Cost-Effective Catalysts for the Electrochemical and Photoelectrochemical Reduction of Carbon Dioxide

by

Sheng Nian Zhang

A thesis submitted in partial fulfillment of the requirements for the degree of

Master of Science

in

Chemical Engineering

Department of Chemical and Materials Engineering
University of Alberta

Abstract

The growing consumption of fossil resources has rapidly depleted fuel availability and increased CO_2 emission, which presents two of the most prominent crises in the modern era. CO_2 reduction reaction (CO_2RR) at ambient conditions using electrochemical (EC) and photoelectrochemical (PEC) methods are promising ways to reducing CO_2 emission while producing storable fuels and chemicals that can be later consumed on demand. To date, highly selective electrochemical conversion of CO_2 to CO, an essential precursor in Fischer-Tropsch processes, require heavily on the use of precious metals while operating at a significant high overpotential. Photocathode-driven PEC conversion of CO_2 can achieve one step conversion of solar energy to chemical energy, but issues such as toxicity, poor selectivity and stability, large external bias potential remain unresolved. On the other hand, photoanodes are well studied in water splitting researches, which can be integrated with CO_2RR electrocatalysts in a photoanode-driven CO_2 reduction system.

In this thesis, a novel, simple, and low-cost Cu_2O-SnO_2 core-shell nanocrystal electrocatalyst was first designed. The electrocatalyst achieved over 90% Faradaic efficiency for CO_2-to-CO conversion at overpotentials of 890 mV and 390 mV in 0.1 M $KHCO_3$ and 0.5 M $KHCO_3$, respectively, which are comparable to those achieved on the precious metals. To further reduce the cell overpotential, a photoanode-driven PEC system is demonstrated through combining Cu_2O-SnO_2 electrocatalyst as a dark cathode and an n-Si/Ni photoanode, achieving a 400-mV reduction in overpotential at 5 mA cm^{-2} when compared to an electrochemical system. The designed PEC cell obtained a photo-assisted efficiency (η_{PAE}) of 3.5% while operated over 12 hours with minor degradation.

Preface

The main results in Chapter 3.1 of this thesis have been published in *ChemCatChem* (DOI:10.1002/cctc.201900395) as Sheng-Nian Zhang, Dr. Meng Li, Dr. Bin Hua, Dr. Nanqi Duan, Shaochen Ding, Prof. Steven Bergens, Prof. Karthik Shankar, Prof. Jing-Li Luo. "A Rational Design of Cu_2O-SnO_2 Core-Shell Catalyst for Highly Selective CO_2-to-CO Conversion". I was responsible for the data collection and analysis, as well as the manuscript composition. Dr. Meng Li contributed to data analysis and manuscript edits. Dr. Bin Hua and Dr. Nanqi Duan contributed to concept formation and electron microscopy data collection. Shaochen Ding contributed to electron microscopy data collection. Prof. Steven Bergens, Prof. Karthik Shankar, and Prof. Jing-Li Luo were the supervisory authors.

Acknowledgments

I would like to express my utmost appreciation to my supervisors Prof. Jing-Li Luo and Prof. Karthik Shankar for their support, guidance, and encouragement to continue tackling the abrupt obstacles throughout this study. I want to express my appreciation to the committee member Prof. Natalia Semagina, for reviewing this thesis and providing her valuable comments.

The work in this thesis was financially supported by the Canada First Research Excellence Fund (CFREF), through the Future Energy Systems (FES) research institute at the University of Alberta. Prof. Steven Bergens and Prof. Karthik Shankar have been instrumental in sharing their valuable expertise and suggestions at our FES progress meetings. For this, I am very grateful.

This research, particularly the portion involving the photoelectrochemical conversion of CO_2, has been a newly explored topic in our group. Progress was slow at the beginning, and there have been many detours during this exploration. Fortunately, many of my colleagues, who became my friends today, have helped me along the way. I would like to particularly thank Dr. Bin Hua, Dr. Meng Li, and Dr. Nanqi Duan for their patience and continuous guidance to overcoming the challenging research problems. It is also a pleasure to work with Aditi Ganji, Stephanie Bozic, Dr. Zhimin Yan, and Dr. Nathan Gerein and staff members of Chemical and Materials Engineering (CME) Department, and National Institute for Nanotechnology, National Research Council of Canada (NINT-NRC).

I want to acknowledge my friends for their support. Also, there are also my beloved pets, Mia and Maya, for bringing joy and companionship. I want to thank my parents for their selfless love and encouragement. Lastly, I wish to thank my girlfriend, Xiaoyi Lan, for her unconditional love and care, and inspiring me to grow and improve.

Table of Contents

Abstract ii

Preface iii

Acknowledgments iv

Chapter 1 Introduction 1

1.1. Current Challenges with CO_2 Emission and Energy Storage 1

1.2. Strategies for CO_2 Reduction 2

1.3. Closing the Anthropogenic Carbon Cycle 3

1.4. Overview of Electrochemical and Photoelectrochemical Reduction of CO_2 5

1.5. Principles of Electrochemical Reduction of CO_2 7

1.5.1. Thermodynamics of CO_2 Reduction Reaction 7

1.5.2. Mechanism of CO_2 Reduction on Metal Electrocatalyst 9

1.5.3. Figure of Merits in Electrochemical CO_2 Reduction 11

1.5.4. Current Status of Metal CO_2RR Electrocatalysts in Aqueous Electrolyte 13

1.6. Principles of Photoelectrochemical Reduction of CO_2 16

1.6.1. Band Structure of Semiconductors 16

1.6.2. Electron-Hole Pair Recombination and the Surface States 20

1.6.3. Co-catalysts and Ohmic Contact 21

1.6.4. Figure of Merits in PEC CO_2 Reduction 22

1.6.5. Current Status of Photoelectrochemical Reduction of CO_2 24

1.7. Remaining Challenges and Statement of Objectives 27

Chapter 2 Experimental Framework and Methods 28

2.1. Material Selection and Experimental Design Framework 28

2.1.1. Cu-Sn Based Material as Promising CO_2-to-CO Conversion Electrocatalyst 28

2.1.2. n-Si/Ni as an Efficient Photoanode 28

2.1.3. Experimental Design Framework 30
2.2. Material Synthesis and Electrode Fabrication 31
2.2.1. Materials 31
2.2.1. Synthesis of Cu_2O-SnO_2 Core-Shell Nanocrystals 31
2.2.2. Preparation of Cu_2O-SnO_2 Dark Cathode 32
2.2.3. Deposition of Ni Thin Film via DC Magnetron Sputtering 32
2.2.4. Preparation of n-Si/Ni Photoanode 34
2.2.5. Preparation of Commercial IrO_2 OER Anode as Benchmark 34
2.3. Material Characterization 35
2.3.1. X-Ray Diffraction Analysis 35
2.3.2. X-Ray Photoelectron Spectroscopy 35
2.3.3. Inductively Coupled Plasma Mass Spectrometry 35
2.3.4. Scanning Electron Microscope 35
2.3.5. Transmission Electron Microscope 36
2.4. Photoelectrochemical and Electrochemical Measurements 36
2.4.1. Cathode Half-Cell Measurements 36
2.4.2. Photoanode Half-Cell Measurements 37
2.4.3. Full Cell Measurements 38
2.5. CO_2RR Product Quantification 39
2.5.1. Gas Product Quantification 39
2.5.2. Liquid Product Quantification 40
Chapter 3 Results and Discussions 42
3.1. Cu_2O-SnO_2 Core-Shell Nanocrystal as CO_2-to-CO Electrocatalyst 42
3.1.1. The Effectiveness of the Synthesis Strategy 42
3.1.2. Crystal Phase and Chemical State of Cu_2O-SnO_2 44

3.1.3. Morphology Evolution of Cu_2O-SnO_2 Nanocrystals 47
3.1.4. Electrochemical CO_2RR Performance in 0.1 M $KHCO_3$ 50
3.1.5. Effect of Electrolyte Concentration 54
3.1.6. Root Cause of Catalyst Degradation 58
3.1.7. Performance Comparison with State-of-the-art Cu-Sn Based Electrocatalyst 59
3.2. n-Si/Ni Photoanode 61
3.2.1. Activation of n-Si/Ni 61
3.2.2. Chemical State of Ni Catalyst Layer 62
3.2.2. Performance of n-Si/Ni Photoanode 64
3.2.2. Current Issues of the n-Si/Ni Photoanode and Potential Resolutions 65
3.3. Photoanode-driven PEC CO_2 Reduction 66
3.3.1. PEC vs. EC System for CO_2 Reduction 67
3.3.1. Stability and System Efficiency 69
Chapter 4 Conclusions and Future Work 71
4.1. Conclusions 71
4.2. Recommendations for Future Work 73
4.2.1. Improving Activity of Cu_2O-SnO_2 Electrocatalyst 73
4.2.2. Benchmarking using Au catalyst 73
4.2.3. Overcoming Mass Transport Limitations of CO_2RR Electrolyser 73
4.2.3. Enhancing the Performance of the n-Si/Ni Photoanode 74
4.2.4. Achieving Unassisted Photoelectrochemical Reduction of CO_2 74
Bibliography 76
Appendix A 1
Appendix B 1

List of Figures

Figure 1-1. Surface average atmospheric CO_2 concentration from 1958 to 2018. 2
Figure 1-2. Closed Carbon Cycle. 4
Figure 1-3. Schematic illustration of a typical setup for A) electrochemical (EC) CO_2RR, and B) photoanode-driven PEC CO_2RR equipped with a quartz window for optimal light transmittance. 7
Figure 1-4. Reaction mechanism of electrochemical CO_2 reduction on metal electrodes in aqueous solutions. 10
Figure 1-5. Band Structure of Metals, Semiconductors, and Insulators. 17
Figure 1-6. Band diagrams of p-type (a-b) and n-type (c-d) immersed in an electrolyte with redox potential ER before equilibrium (a,c) and at equilibrium (b,d). 19
Figure 1-7. Conduction band (white squares) and valence band (gray squares) potentials of some commonly used semiconductors, with the potentials of several CO_2 and water redox couples at pH 0, plotted versus vacuum (left) and NHE (right).. 20
Figure 1-8. Schematic illustrations of three possible two-compartment PEC cells separated by proton-exchange membranes for the reduction of CO_2. (A) Semiconductors as photocathodes. (B) Semiconductors as photoanode. (C) Semiconductors as both photocathode and photoanodes. 26
Figure 2-1. Experimental Design Framework. 30
Figure 2-2. Schematic of magnetron sputter system depositing Ni thin film onto a silicon wafer. 33
Figure 2-3. Experimental setup for EC CO_2RR test using three-electrode method. 37
Figure 2-4. Experimental setup for PEC OER test using three-electrode method. 38
Figure 2-5. Experimental setup for PEC full cell test using two electrode method. 39
Figure 3-1. Schematic illustration the of two-step synthesis of Cu_2O-SnO_2 core-shell catalyst. 42
Figure 3-2. XRD patterns of Cu_2O and Cu_2O-SnO_2 core-shell crystal. 44
Figure 3-3. (A) Cu2p XPS spectrum of Cu_2O-SnO_2 core-shell crystal, (B) Sn3d XPS spectrum of Cu_2O-SnO_2 core-shell crystal. 45
Figure 3-4. HR-TEM image at the catalyst shell layer. 46
Figure 3-5. SEM images of (A,B) Cu_2O nanocubes, (C,D) CuSn10, and (E,F) CuSn40. 48

Figure 3-6. TEM, HAADF, STEM-EDX images of CuSn10. 49
Figure 3-7. TEM, HAADF, STEM-EDX images of CuSn40. 49
Figure 3-8. Gas product faradaic efficiency of carbon black support in 0.1 M $KHCO_3$. 50
Figure 3-9. Chronoamperometry-derived LSV of carbon black support in 0.1 M $KHCO_3$. 51
Figure 3-10. (A) Chronoamperometry-derived LSVs for all tested catalysts, and (B) Faradaic efficiency of CO (FE_{CO}) for all tested catalysts. 52
Figure 3-11. FE_{CO} at -1.0 V vs. RHE as a function of Sn mol% (measured via ICP-MS) in the Cu_2O-SnO_2 catalyst. 53
Figure 3-12. Gas product faradaic efficiencies of CuSn40 tested in 0.1 M $KHCO_3$. 54
Figure 3-13. Gas product faradaic efficiencies of CuSn40 tested in 0.5 M $KHCO_3$. 55
Figure 3-14. Gas product Faradaic efficiency of CuSn40 catalyst tested in 0.1 M $KHCO_3$ (dashed-line) and 0.5 M $KHCO_3$ (solid-line). 56
Figure 3-15. Partial current densities of CuSn40 catalyst tested in 0.1 M $KHCO_3$ (dashed-line) and 0.5 M $KHCO_3$ (solid-line). 56
Figure 3-16. Long-term stability test of CuSn40 catalyst at -0.6 V vs. RHE for 18 hours in 0.5 M $KHCO_3$. 57
Figure 3-17. SEM image of CuSn40 catalyst after stability test. 58
Figure 3-18. (A) TEM, and (B) HAADF and STEM-EDX images of CuSn40 catalyst after stability test. 59
Figure 3-19. One-hour activation of Ni catalyst layer by applying a potential of 2.0 V vs. RHE in 1 M KOH. 61
Figure 3-20. Linear sweep voltammograms of fresh n-Si/Ni sample (black) and activated n-Si-Ni sample (red). 62
Figure 3-21. Ni2p XPS spectrum of the activated n-Si/Ni photoanode. 63
Figure 3-22. Structure schematic of n-Si/Ni photoanode with $Ni(OH)_2$ & γ-NiOOH active layer. 64
Figure 3-23. Linear sweep voltammograms of Ni-coated n-Si photoanode under illumination (red line) and dark (black line), and degenerately doped n++Si in the dark. 65

Figure 3-24. Schematic illustration of the two-compartment PEC cell driven by a photoanode. 67
Figure 3-25. LSV of full cell driven by a n-Si/Ni photoanode (blue) and by a commercial IrO2 OER catalyst (yellow). 68
Figure 3-26. Chopped light (30 s/10 s on/off) CA measurement with at cell voltage of 1.8 V. 68
Figure 3-27. Long-term stability of the PEC system at a cell voltage of 1.8 V for 12 hours. 69

List of Tables

Table 1-1. Simplified Comparison of Electrochemical (EC) and Photoelectrochemical (PEC) Systems for CO_2RR. 6
Table 1-2. Formal Electrochemical Redox Potential (pH 7) for the Reduction of CO_2 and Related Compounds in Aqueous Media. 8
Table 2-1. Magnetron sputter system parameters for the deposition of Ni 33
Table 3-1. Measured Cu and Sn bulk concentrations in Cu_2O-SnO_2 catalysts and their respective molar ratios from ICP-MS results. 43
Table 3-2. Comparison of Cu_2O-SnO_2 catalyst to literature. 60

Chapter 1 Introduction

1.1. Current Challenges with CO_2 Emission and Energy Storage

In the last two centuries, the growing consumption of fossil resources has rapidly depleted fuel availability and increased greenhouse gas (GHG) emission, notability carbon dioxide (CO_2) emission.[1, 2] Despite ongoing efforts in shifting fossil fuel reliance to renewable energy,[3] fossil will still serve as the primary energy source for the upcoming decades to meet the society's growing demand for better living standards, and to supply the needs of the expanding world population. As such, global warming due to GHG emissions and energy shortage present two of the prominent crises right now and going forward.

According to the *Global Carbon Budget 2018* report by C. Le Quéré et al.,[2] the global average atmospheric CO_2 concentration reached an all-time high of 405.0 ppm in 2017 (Figure 1-1). Just over the last decade (2008-2017), the CO_2 emission rate grew by 1.5% yr^{-1}, where 87% of total CO_2 emission was caused by burning fossil fuels.[2] These alarming numbers are indicative of how CO_2 emission reduction remains a significant challenge in recent years. Renewable sources, such as solar and wind electricity, are attractive alternatives to fossil fuels since they are carbon neutral and do not contribute to GHG emissions. However, these types of energy supply are not available on demand due to their transient nature, and there is no established technology to store the energy at scale and a reasonable cost.[4] Therefore, in addition to CO_2 reduction, developing a suitable energy storage technology is also of great importance.

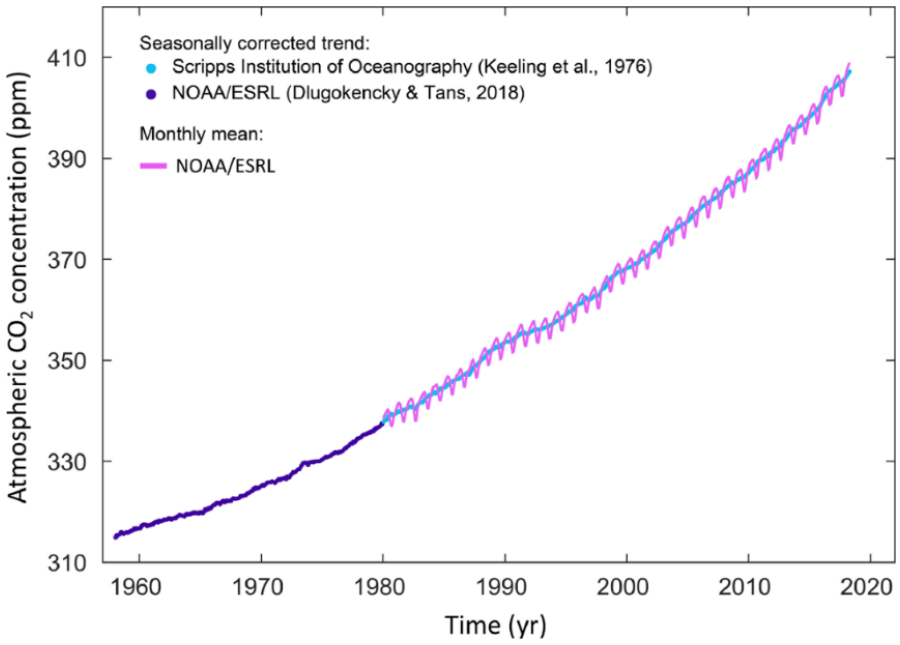

Figure 1-1. Surface average atmospheric CO_2 concentration from 1958 to 2018. Reproduced with permission.[2] Copyright 2018, Earth System Science Data.

1.2. Strategies for CO_2 Reduction

There are three main approaches to reduce atmospheric CO_2 concentration: CO_2 emission prevention, carbon capture and storage (CCS), and CO_2 utilization and conversion.

The first approach can be achieved through implementing more energy efficient and low emission technologies, shifting fuel dependence from coal to gas, installing better insulation of buildings (less cooling and heating required), developing a more conscious attitude toward energy use, and so-on.[5] However, these strategies do not sufficiently reduce CO_2 emission, while global energy consumption continues to increase rapidly.

Since early year 2000s, carbon capture and storage (CCS) technology is perceived as a compelling route for decarbonizing future energy.[6] It enables the capturing of large-scale CO_2 emission directly from large emitters such as power, petrochemical, cement and steel plants, and subsequent storing of CO_2 via geological formation in natural fields such

as depleted oil and gas fields, aquifers, and coal beds [2]. Nevertheless, implementation of CCS at a global scale still face significant barriers due to its high capital and operating costs, and intensive energy requirements from separation, compression, sorbent regeneration, and transportation of CO_2. Therefore, a more sustainable route is desired.

The utilization and conversion of CO_2 as chemical feedstock is another attractive solution to resolve emission issues. It can be divided into two main categories, direct (physical) utilization of CO_2, and conversion of CO_2 into fuels and chemicals.[7] Direct (physical) CO_2 utilization can vary from small scale applications such carbonated drinks, dry ice, fire extinguisher, and solvent, up to large-scale industrial applications such as enhanced oil recovery (EOR), enhanced gas recovery (EGR) and enhanced geothermal systems (EGS).[1] In these cases, CO_2 remains pure in the dissolved form and do not contribute to its overall abatement.[7] Study shows that the current global CO_2 utilization is approximately 200 $MtCO_2$, which almost negligible compared to the anthropogenic CO_2 emissions of over 32,000 $MtCO_2$.[1] For CO_2 conversion to fuel and chemicals, CO_2 breaks down to the basics (carbon or carbon monoxide) or react with other compounds to form longer chained molecules, such as calcium carbonate, urea, salicylic acid, formic acid, methanol, dimethyl ether (DME), etc.[1] However, not all products derived from CO_2 are economically viable due to the high cost and insufficient market demand.

1.3. Closing the Anthropogenic Carbon Cycle

In more recent years, research efforts have been targeted more towards efficient and recyclable CO_2 approaches, implying the conversion of post-captured CO_2 into storable chemical fuels which can be subsequently consumed on demand. In an ideal case, this strategy will simultaneously alleviate both CO_2 emission issues and energy storage

problem. The most common approaches, including thermocatalysis, photocatalysis, electrocatalysis, and photoelectrocatalysis. [8, 9] These approaches can convert CO_2 into light hydrocarbon fuels such as methane, ethylene, formic acid, and methanol, to name a few, or to syngas (CO and H_2), an essential feedstock for Fischer-Tropsch process and methanol synthesis.[5, 10] In an ideal scenario, when carbon capture, utilization, and conversion processes are combined, a closed anthropogenic carbon cycle with zero net CO_2 emission can be achieved, as shown in Figure 1-2.

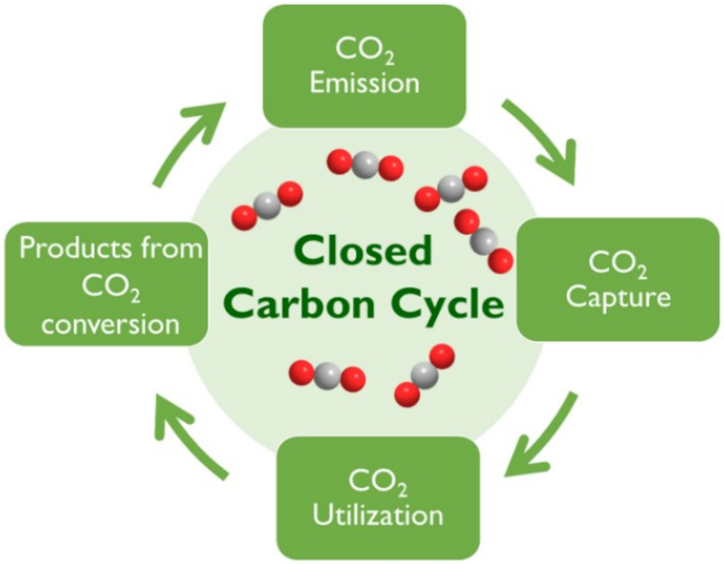

Figure 1-2. Closed Carbon Cycle.

Thermocatalytic conversion of CO_2 using reforming processes has been well studied at both scientific and industrial scale.[1] It combines the use of high temperature and heterogeneous catalyst, typically metallic nanoparticles supported on ceramic material.[4] These processes often require efficient heat supply or removal, adequate reactor design, as well as catalysts that are resistant to deactivation.[4] Photocatalytic (PC) CO_2 reduction, namely artificial photosynthesis, operates solely based on solar energy but is bottlenecked by the lack of efficient photocatalyst, which leads to low product yield and

selectivity. Electrochemical (EC) reduction method, on the other hand, attracted more interests due to its capability to convert CO_2 at ambient conditions and has the flexibility to use electrical energy produced from different sources, such as coal, hydro, geothermal, nuclear, wind and solar power. This method also allows more precise control over product selectivity by tuning applied cell potential, but at the same time consumes a large amount of electricity to overcome the high energy barrier of CO_2 reduction reaction (CO_2RR). Lastly, the photoelectrochemical (PEC) route is an integration of both EC and PC systems and poses advantages of both worlds, such as tunable product selectivity and direct light harvesting capability. In theory, a properly designed PEC system should operate at lower cell voltage compared to EC, have more controlled product selectivity and higher product yield compared to PC.

This thesis is emphasized on the design of novel and efficient catalysts for electrochemical and photoelectrochemical CO_2 reduction. The remainder of this chapter will introduce an overview of EC and PEC systems, discuss their fundamental principles and current research status, and outline the remaining challenges and research objectives.

1.4. Overview of Electrochemical and Photoelectrochemical Reduction of CO_2

Photoelectrochemical and electrochemical reduction of CO_2 is a multi-step and multi-electron cathodic reaction process that takes place at an electrode-electrolyte interface.[11] Both systems share many similarities in terms of the reactor (electrochemical cell) design, electrolyte, catalyst (or co-catalyst) material for CO_2RR, reduced products, and electrochemical analysis methods. The main difference arises from the type of

electrode utilized in each system. A brief comparison of the two systems is outlined in Table 1-1.

Table 1-1. Simplified Comparison of Electrochemical (EC) and Photoelectrochemical (PEC) Systems for CO_2RR.

	EC	PEC
Cell	Two-compartment H-type cell separated by a proton-exchange membrane (PEM)	
Electrode	Conductors	Semiconductors
Electrode Configuration	Cathode + Anode	Three Configurations 1. Photocathode + Dark Anode 2. Dark Cathode + Photoanode 3. Photocathode + Photoanode
Electrolyte	Aqueous, and non-aqueous	
Catalyst (co-catalyst) for CO_2RR	• Homogeneous catalysts: organic and metal-organic complex • Heterogeneous catalysts: metal, transition metal oxide, transition metal chalcogenides, carbon-based material	
Reduced Products	CO, HCOOH, CH_4, C_2H_4, CH_3OH, etc.	
Source of electron	External power	Photo-excited electron (e^-) and holes (h^+) upon illumination ($E_{light} > E_g$)

Since EC and PEC share common fundamental knowledge such as thermodynamics principles and reaction mechanisms, exploring EC system as a starting point should provide a more profound understanding of the subject matter and allow a smoother transition for designing a functional PEC CO_2 reduction system. Moreover, catalysts developed from EC can be implemented directly into PEC either as co-catalysts on semiconductor photocathode or used as a dark cathode in a photoanode-driven system.[12] Figure 1-3 shows the schematic illustrations of EC and photoanode-driven PEC systems.

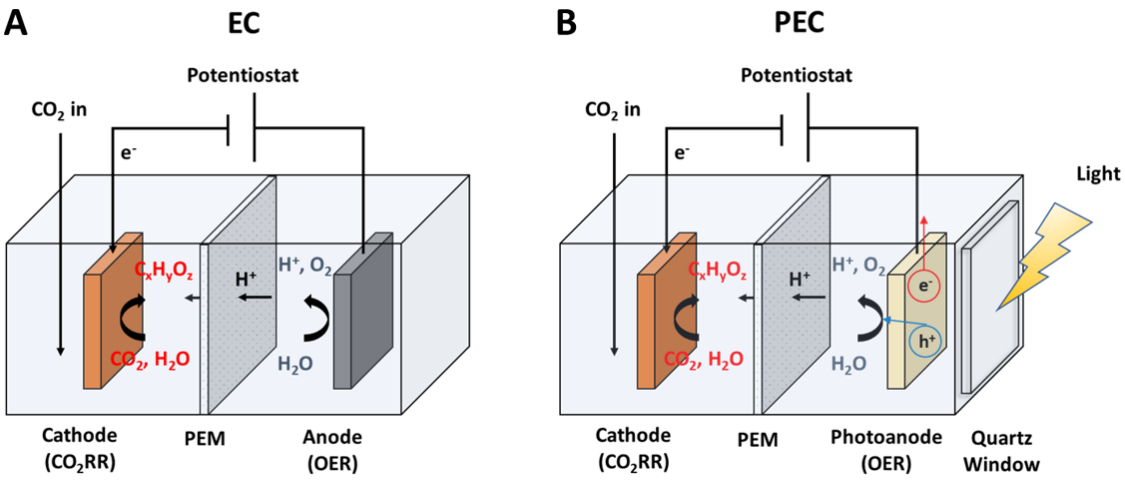

Figure 1-3. Schematic illustration of a typical setup for A) electrochemical (EC) CO_2RR, and B) photoanode-driven PEC CO_2RR equipped with a quartz window for optimal light transmittance. Both systems utilize a two-compartment cell separated by a proton-exchange membrane (PEM).

It should also be noted that catalyst performance can vary significantly when evaluated under different types of electrolytes (aqueous or non-aqueous). Aqueous electrolytes with pH close to neutral, such as bicarbonate (HCO_3^-) solutions, are particularly attractive due to their low cost and non-toxic nature, which is also the electrolyte used in this thesis work.

Sections 1.5 and 1.6 introduce the fundamentals of electrochemical and photoelectrochemical reduction of CO_2, respectively. Then, section 1.7 will outline the remaining challenges and objectives of this thesis.

1.5. Principles of Electrochemical Reduction of CO_2

1.5.1. Thermodynamics of CO_2 Reduction Reaction

Considering CO_2 is a fully oxidized and extremely stable molecule, significant energy must be introduced into the reaction mixture to drive its conversion into reduced products.[13] In the case of CO_2 reduction half-reactions, the required energy is measured

by the formal electrochemical redox potential (E^{0}'). The E^{0}' in reference to the standard hydrogen electrode (SHE, pH = 7) for various CO_2 reduction reactions are provided in Table 1-2. The E^{0}'of hydrogen evolution reaction (HER) is also included here because it competes with CO_2 reduction reaction (CO_2RR) at a similar potential range, which also agrees with the fact that H_2 is the major by-product for CO_2 reduction in aqueous electrolyte. Additionally, the products of CO_2RR are generally a mixture of several species (apart from the undesired H_2), which will create complications for downstream product separation. Therefore, an adequate catalyst should minimize the contribution from HER as well as promote product selectivity of CO_2RR experiments.

Table 1-2. Formal Electrochemical Redox Potential (pH 7) for the Reduction of CO_2 and Related Compounds in Aqueous Media. Adapted with permission.[9] Copyright 2015, American Chemical Society.

Eq.	Reaction	E^0 (V) vs. SHE
1-1	$CO_2 + e^- \rightarrow CO_2^{\bullet -}$	−1.850
1-2	$CO_2 + H_2O_{(l)} + 2e^- \rightarrow HCOO^-_{(aq)} + OH^-_{(aq)}$	−0.665
1-3	$CO_2 + H_2O_{(l)} + 2e^- \rightarrow CO_{(g)} + 2OH^-_{(aq)}$	−0.521
1-4	$CO_2 + 3H_2O_{(l)} + 4e^- \rightarrow HCOH_{(l)} + 4OH^-_{(aq)}$	−0.485
1-5	$CO_2 + 5H_2O_{(l)} + 6e^- \rightarrow CH_3OH_{(l)} + 6OH^-_{(aq)}$	−0.399
1-6	$CO_2 + 6H_2O_{(l)} + 8e^- \rightarrow CH_{4(g)} + 8OH^-_{(aq)}$	−0.246
1-7	$2H_2O_{(l)} + 2e^- \rightarrow H_{2(g)} + 2OH^-_{(aq)}$	−0.414

Although thermodynamic data above shows that only moderately negative potentials are required to reduce CO_2, significant overpotential (the difference between

applied potential and equilibrium potential) is needed during operation due to CO_2RR's sluggish kinetics.[11] Such high overpotential is believed to caused by the rate-determining step involving the one-electron reduction of CO_2 to $CO_2^{\bullet-}$ radical anion (E^0 = -1.850 V vs. SHE).[14]

1.5.2. Mechanism of CO_2 Reduction on Metal Electrocatalyst

Electrochemical reduction of CO_2 can be classified into two categories: homogeneous and heterogeneous.[15] Homogeneous reactions utilize organic or metal-organic molecules as electrocatalysts with unique active centers interacting with CO_2 molecules.[16, 17] However, homogenous electrocatalysts have the disadvantages of high cost, toxicity, and complex post-separation process, which are limiting its application at industrial scale.[11] On the other hand, inorganic heterogeneous catalysts, mainly metal and metal oxide catalyst, have attracted increasing attention due to their facile synthesis, environmental friendliness, high efficiency, and better readiness for industrial applications.[11, 18]

There are basically three steps in a heterogeneous catalysis process in an aqueous electrolyte: i) adsorption of CO_2 (dissolved or gaseous) onto the catalyst sites and subsequent formation of $CO_2^{\bullet-}$ radical, ii) electron and/or proton transfer to break C-O bonds and/or form C-H bonds, and iii) product desorption and diffusion into electrolyte.[19] Although the reaction mechanism can vary from catalyst to catalyst, a general representation of CO_2RR mechanism on metal electrodes in aqueous solution is proposed, shown in Figure 1-4.[11] For group 1 metals, including Sn, Hg, Pb, and In, the $CO_2^{\bullet-}$ intermediate can hardly bind onto the catalyst, which facilitates in the formation of formic acid or formate through an outer-sphere mechanism.[20] This mechanism is still under

debate as others have suggested that the stabilization of *OCHO intermediates is instead the critical step in the formation of formic acid or formate.[21] Au, Ag, Zn, and Pd from group 2 metals can bind well with *COOH intermediate for further reduction (proton and electron transfer denoted by H^++e^-), but the subsequent *CO intermediate is loosely bound to their surfaces, which leads to the formation of carbon monoxide (CO). Cu is the only metal in group 3 and is capable of binding and converting *CO intermediate to higher value-added hydrocarbon and alcohols through *COH or *CHO intermediates. It should be noted that the binding strength of *CO intermediate should only be moderate since stronger binding strength will likely to eliminate CO_2RR, and HER will dominate. Metals such as Pt, Ti, Fe, and Ni are prone to be HER dominant for such reason.[11] Therefore, understanding the binding energies of key intermediates on the catalyst is critical for the rational design of a highly selective and efficient catalyst for CO_2RR.

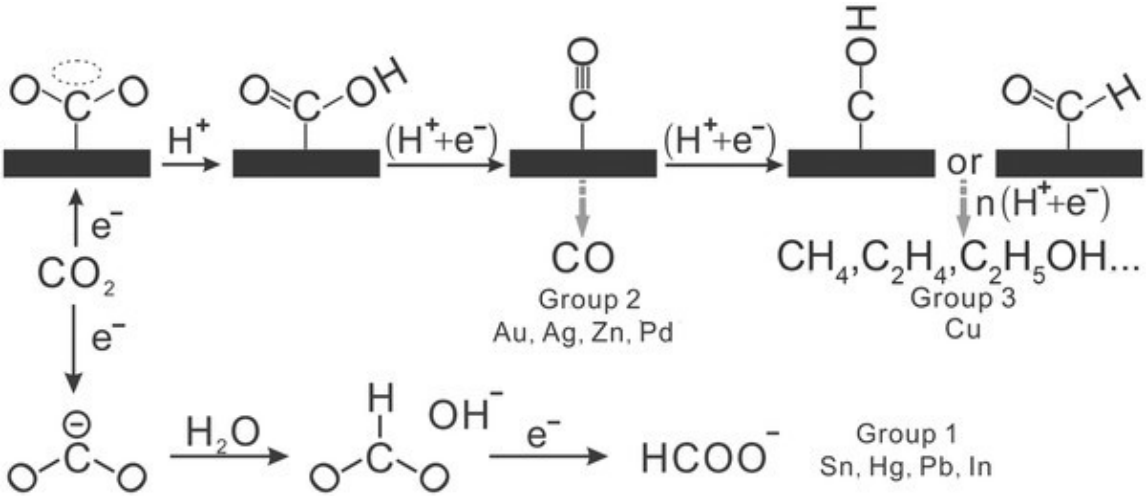

Figure 1-4. Reaction mechanism of electrochemical CO_2 reduction on metal electrodes in aqueous solutions. Reproduced with permission.[11] Copyright 2016, Wiley-VCH.

1.5.3. Figure of Merits in Electrochemical CO_2 Reduction

Overpotential (η)

As discussed earlier, the applied potential (E) applied for CO_2RR is usually much more negative (cathodic) than the thermodynamic one, $E^{0'}$.[17] The difference between them is defined as the overpotential (η), and is expressed as follows:

$$\eta = E - E^{0'} \tag{1-8}$$

Faradaic Efficiency (FE)

The Faradaic efficiency (FE) is a popular term used to define as the percentage of electrons consumed for the formation of a specific product (j); in other words, target product selectivity. The expression for calculating FE is:

$$FE_j = \frac{\alpha n F}{Q} \times 100\% \tag{1-9}$$

where α is the number of moles of electrons transferred (i.e., 2 moles of electrons for CO and HCOOH, 8 electrons for CH_4, etc.), n is the number of moles of a specific product, F is the Faraday's constant (96,485 C mol^{-1}), and Q is the total number of charges passed measured in Coulomb (C).

Current Density

The current density is a measure of reaction rate in EC CO_2RR experiments. It is calculated by dividing the measured current over the geometric surface area of the working electrode. This parameter is essential for determining the size of the electrolyzer and cost for the process. Also, due to several different possible products from CO_2RR as well as the

competing HER, a partial current density of a specific product is usually considered, which is calculated by multiplying the corresponding FE by the overall current density.

Energy Efficiency (EE)

The energy efficiency is the overall energy utilization toward the desired product, which is expressed by:

$$EE = \frac{E_{eq}}{E_{eq}+\eta} \times FE_j \quad (1\text{-}10)$$

where E_{eq} is the equilibrium potential and is the summation of anodic thermodynamic potential (H_2O/O_2: 1.23 V vs. Reversible Hydrogen Electrode (RHE)) and cathodic thermodynamic potential (i.e., CO_2/CO: -0.11 V vs. RHE). In typical three-electrode test results described in most previous work on CO_2RR, only cathodic half-cell overpotential (η) is considered and the anodic half-cell is assumed to have zero overpotential.

Hence, it is not difficult to realize that a high EE in CO_2RR should encompass a low overpotential and a high FE at the same time; it is an ongoing effort for the CO_2 reduction community to continue developing catalysts with the smallest overpotential and highest faradaic efficiency possible.

Stability and Cost

Stability is another vital merit for evaluating a catalyst, as it determines how often a catalyst needs to be replaced. Additionally, many of the high performing catalysts utilize precious metals, which adds another cost factor when designing a catalyst. It is therefore desirable to utilize a low-cost, earth-abundant catalyst for carrying out CO_2RR.

1.5.4. Current Status of Metal CO_2RR Electrocatalysts in Aqueous Electrolyte

As mentioned in the previous section, metal and metal oxide catalysts have shown steady improvement and great promises in the last decades.[11, 18, 22] More specifically, nano-engineered metal catalysts with specific sizes, structures, and surface chemical states have demonstrated superior performance compared to their bulk counterparts.[23-43]

Copper-Based Electrocatalyst

Copper (Cu) has been intensely studied owing to its unique ability to electrochemically reduce CO_2 into C_1 and C_2 products at a significantly higher selectively comparing to other metal electrodes.[36-42] Li et al. reported ultrathin twinned copper nanowires (Cu NWs) wrapped with graphene oxide (rGO).[36] The catalyst exhibited up to 55% FE towards CH_4 at -1.25 V vs. RHE with well-preserved structure after electrolysis. The morphology feature of the twinned nanowire, as well as its robust structural integrity, were attributed to the high CH_4 selectivity. Recent works also suggested that oxide-derived Copper (OD-Cu) is catalytically more favorable towards reducing CO_2 into hydrocarbons compared to metallic Cu.[37, 39, 41, 42] The OD-Cu is usually prepared by in-situ electrochemical reduction of copper oxide, with most of its surface reduced to the metallic state while the subsurface oxides are retained. Through experimental findings and density functional theory (DFT) simulations, Eilert et al. suggested that the residual subsurface oxide could have altered the electronic structure of the catalyst and created active sites with higher CO binding energy.[42] Similar conclusions were drawn from oxide-derived Ag and Au catalysts, where they also demonstrated higher performance compared to their metallic counterparts.[31, 43]

Bismuth and Tin-Based Electrocatalysts

2D-structure Bi nanosheets and nanoflakes,[28, 34, 35] as well as Sn/SnO_2,[44-46] have demonstrated superior activity and selectivity towards producing formate or formic acid. Han et al. reported an ultrathin Bismuth nanosheet (BiNS) derived via in-situ topotactic transformation of bismuth oxyiodide nanosheets (BiOI).[28] The BiNS, which possess single crystallinity and enlarged surface area, displayed a broader range of high FE (>90%), substantially higher partial current density, and excellent durability for formate production when compared to a commercial Bi. The excellent performance was investigated through DFT calculations, which revealed that the predominantly exposed Bi (001) plane on the BiNS facilitated the stabilization of OCHO* intermediate and subsequent formate formation. Li et al. reported hierarchical mesoporous SnO_2 nanosheets on carbon cloth which exhibited a high partial current density of 45 mA cm^{-2} at moderate overpotential and high FE (87%) towards formate production. Additionally, the minimal current drop was observed for 24 hours of durability test. The author attributed this superior performance to the large surface area and porous structure from the SnO_2 nanosheets, which improved the charge and mass transfer during electrochemical tests. The structural robustness of this material also attributed to the performance durability of the catalyst.

Silver, Gold, and Palladium-Based Electrocatalysts

For reducing CO_2 to CO, precious metals such as Ag,[24-26, 32, 33, 43] Au,[29-31] and Pd[23, 29] with specific nanostructures have exhibited outstanding CO selectivity (>90% FE) and excellent stability at low to moderate overpotentials. Lu et al. reported a nanoporous silver (np-Ag) electrocatalyst that can convert CO_2 to CO with FE of 92% at

moderate overpotential (<0.50 V vs. RHE), which is 3,000 times higher than the polycrystalline counterpart.[25] The increased activity was attributed to the increased electrochemical surface area and a highly curved surface, which enabled improved stabilization of $CO_2^{\bullet-}$ intermediate. Zhu et al. compared the electrocatalytic activity of monodispersed Au nanoparticles (NPs) with sizes of 4, 6, 8, and 10 nm.[27] A FE of 90% at -0.67 V vs. RHE was achieved on the 8 nm Au NPs, while the other sizes were significantly lower (<80%). DFT calculations further suggested that the high CO selectivity on 8 nm NPs was due to the presence of optimum ratio of the edge sites (active for CO_2RR) over corner sites (active for HER). Gao et al. studied the size-dependent catalytic activity of Pd NPs.[23] The Faradaic efficiency for CO production increased from 5.8% at -0.89 V vs. RHE over 10.3 nm NPs to 91.2% over 3.7 nm NPs, as well as a substantial increase in current density. The theoretical study confirmed that the CO_2 adsorption, COOH* intermediate formation, and CO* removal energies are related on the size of Pd NPs, or more specifically, the ratio of the corner, edge, and terrace sites.

To summarize, single element metal and metal oxide catalysts have been well studied experimentally. Although several products have been successfully synthesized from CO_2RR electro-reduction, only formic acid/formate and CO could be obtained at a satisfying selectivity and moderate overpotential. Formic acid/formate production using Bi-based or Sn-based catalysts showed promising results so far, but CO production mostly relies on precious metals.

1.6. Principles of Photoelectrochemical Reduction of CO_2

As discussed in Chapter 1.4, a PEC system can harvest light energy to supplement or even replace electrical energy inputs using semiconductor photoelectrode.[9] Unlike metal electrode in electrochemical systems, the effect of applied potential does not directly govern the electrochemistry on a semiconductor electrode. This difference mainly arises from the unique electronic band structure of semiconductors.

1.6.1. Band Structure of Semiconductors

In terms of solid-state physics, solids have two energy bands that are formed by delocalized orbitals that overlap. The low-energy band of mainly filled orbitals is called valance band (VB), whereas the higher energy band of mainly empty orbitals is called conduction band (CB).[9] For metals, these two bands overlap, forming continuous energy states for the electrons, whereas, in semiconductors and insulators, CB and VB are separated by a quantum mechanically forbidden energy zone, called band gap (E_g). Figure 1-5 shows the band structure of metals, semiconductors, and insulators. Metals usually conduct electricity well because electrons can move freely within the overlapped CB and VB. Semiconductor does not normally conduct electricity due to the existence of bandgap. However, if E_g is less or equal than the energy of incident photon/light (i.e., $h\nu \geq E_g$), then the electrons from VB of the semiconductor can be excited to CB as they gain sufficient energy from light.[47] Then, the electrons excited to the conduction band and the holes in the valence band are used to perform photocatalytic reactions (details discussed in the followed section). Lastly, insulators have too large of a bandgap to be excited by photon.

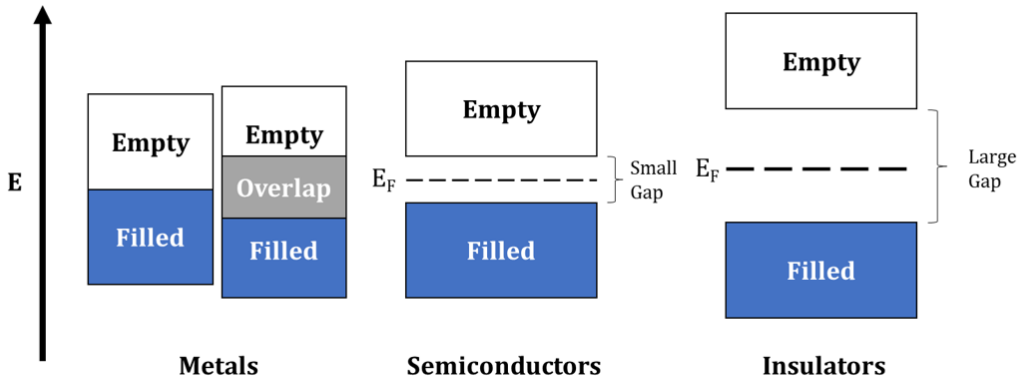

Figure 1-5. Band Structure of Metals, Semiconductors, and Insulators. (CB: Blue, VB: White)

Semiconductors are usually categorized as intrinsic semiconductor and extrinsic semiconductor, which differs in the charge densities of electrons and holes. The transition from intrinsic to extrinsic is achieved through doping. For intrinsic semiconductors, the charge densities are equal, and their Fermi level (E_F, the energy level at which the probability of finding an electron in the energy band is ½ at 0 K[47]) lies approximately at the midpoint between the lower edge of CB and the upper edge of VB (Figure 1-5). By introducing vacancies or impurities, either of the charge densities can be altered. Semiconductors with acceptor impurities such as boron (B) or aluminum (Al) will generate extra holes by attracting the neighboring electrons in the original lattice, resulting in a p-type semiconductor with E_F slightly above VB (Figure 1-6a).[47] On the contrary, semiconductors with donor impurities such as phosphorus (P) or arsenic (As) will provide extra electrons to the lattice, resulting in an n-type semiconductor with E_F slightly below CB (Figure 1-6c) [47]. The type of semiconductor (n-type or p-type) usually determines how the semiconductor behaves upon contact with an electrolyte.

When a semiconductor is immersed in an electrolyte, the Fermi level of semiconductor will equilibrate with the redox potential of electrolyte to minimize their

difference in Gibbs free energy, thereby causing electron transfer at the interface and forming a band-bending gradient (Figure 1-6b, d).[9] The electron flow across the interface creates a space-charge layer due to depleted majority charge carriers near the junction inside the semiconductor.[48, 49] The electric field induced by the band-bending gradient will, therefore, facilitate the photo-excited charges to migrate in opposite directions. The minority charge carrier moving towards the interface will be utilized to perform electrochemical reactions, and the majority charge carrier will migrate through the bulk semiconductor and external circuit to complete the redox cycle at the other half electrode. The p-type semiconductor bulk will have an upward band-bending gradient which allows the photo-generated electrons to migrate to the interface more easily (Figure 1-6b). The opposite occurs at n-type semiconductor bulk, where the photo-generated holes are driven towards the semiconductor interface (Figure 1-6d). Therefore, photo-reduction reactions mostly utilize p-type semiconductors, and photo-oxidation mostly utilize n-type semiconductors.

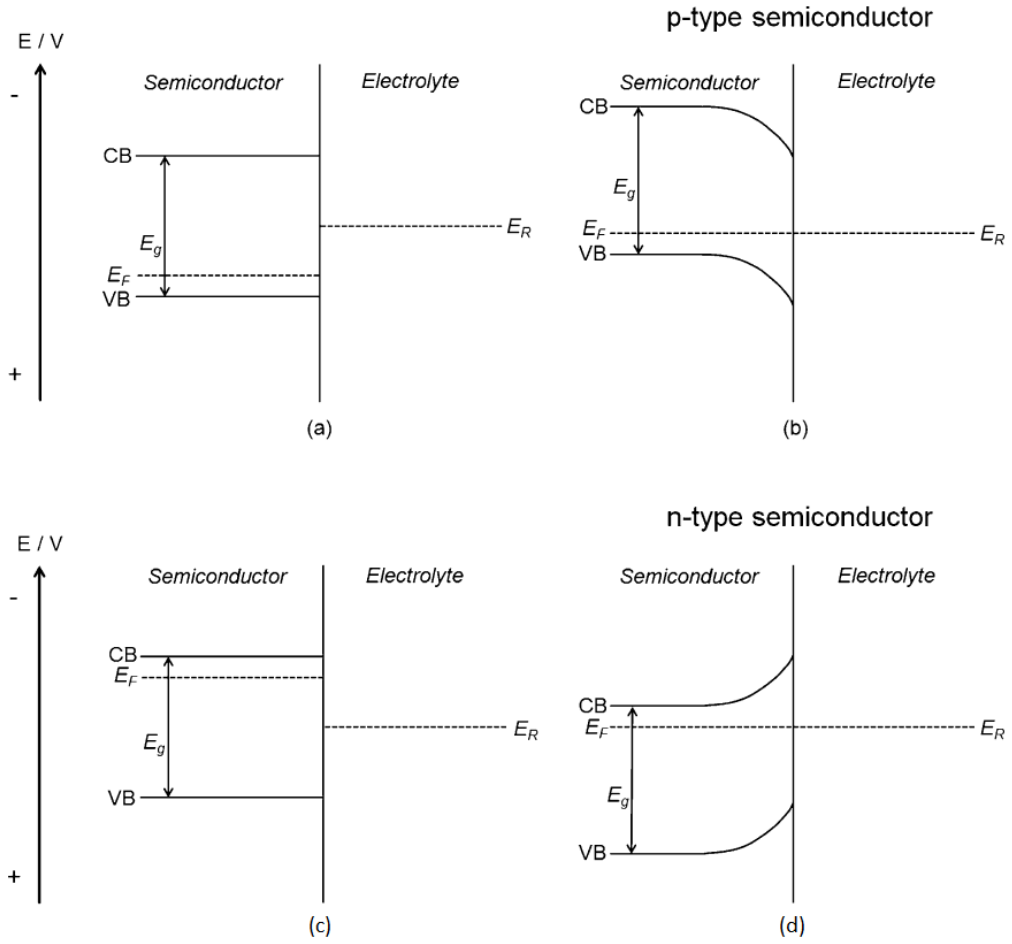

Figure 1-6. Band diagrams of p-type (a-b) and n-type (c-d) immersed in an electrolyte with redox potential ER before equilibrium (a,c) and at equilibrium (b,d). Reproduced in part with permission.[9] Copyright 2015, American Chemical Society.

Besides, for CO_2 photo-reduction, the conduction band minimum (CBM) of the semiconductor should lie at a potential more negative than the reduction potentials of CO_2 (i.e., in Figure 1-7, Si, SiC, and GaP are examples of appropriate semiconductors only based on CBM). The larger the difference between the band edge and the redox potential, the more photovoltage a photoelectrode could supply to the overall PEC system. Theoretically, a properly designed PEC system can operate with certain "underpotential",

meaning below the equilibrium potential. Figure 1-7 shows some of the commonly used semiconductor materials for photo-driven CO_2 reduction and water splitting applications.[9]

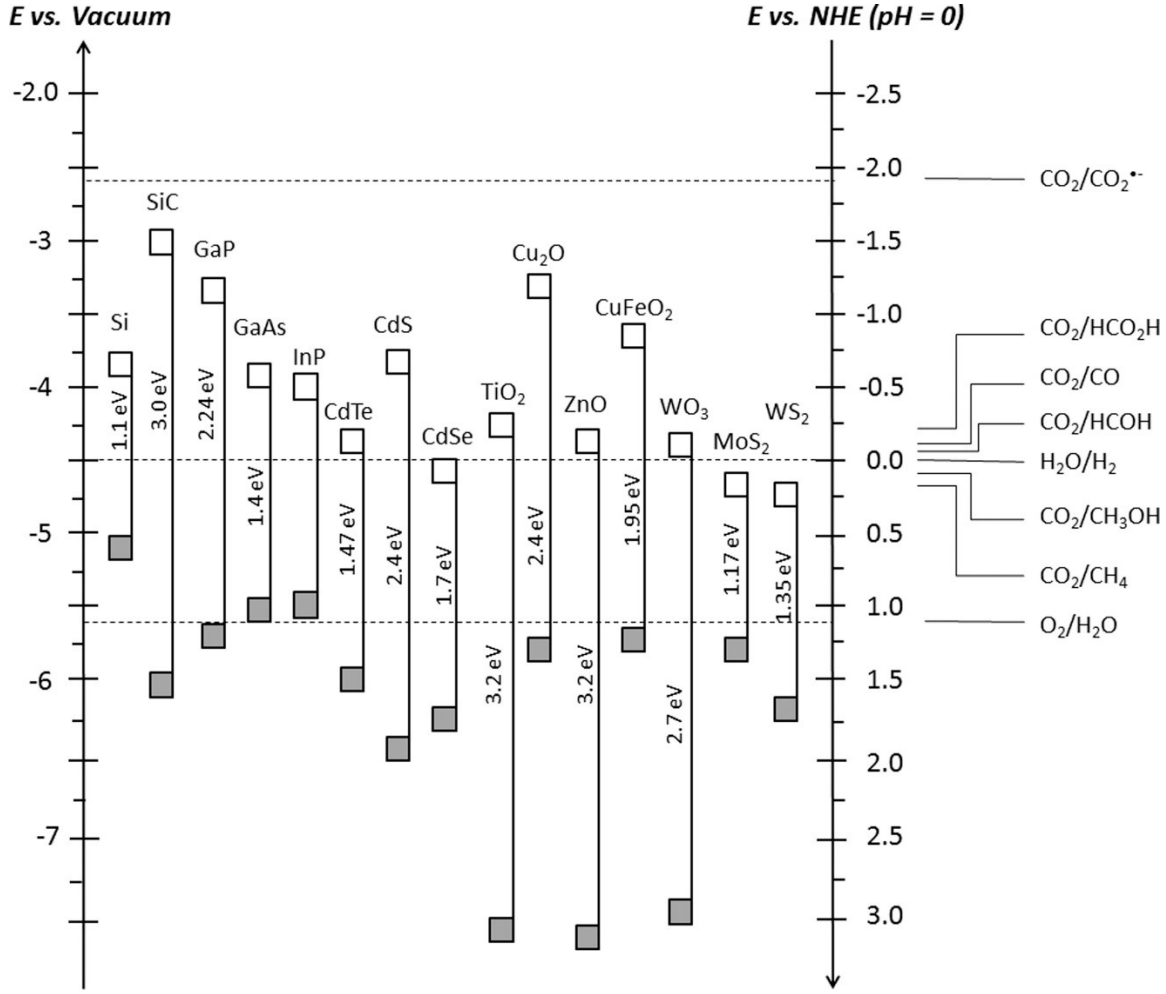

Figure 1-7. Conduction band (white squares) and valence band (gray squares) potentials of some commonly used semiconductors, with the potentials of several CO_2 and water redox couples at pH 0, plotted versus vacuum (left) and NHE (right). Reproduced with permission.[9] Copyright 2015, American Chemical Society.

1.6.2. Electron-Hole Pair Recombination and the Surface States

Another essential concept is the charge recombination, which is the annihilation of photo-generated charges to achieve charge neutrality. Since photocatalytic redox reactions usually involve multiples steps, the electron-hole pair must be separated in a way that its recombination occurs slower than the redox reactions.[9] However, the time between

separation and recombination of the electron-hole pair, known as carrier lifetime, occurs on a nanosecond timescale. Thus the photo-generated charges do not have enough time to travel to the semiconductor surface and subsequently get involved in redox reactions. The fast charge recombination is considered a major bottleneck in the field of photocatalysis research.[9] On the other hand, because an external bias can be applied in a PEC system, the band-bending at the semiconductor-electrolyte interface can further deviate from the equilibrium state, which directs the charges in opposite directions more efficiently and reduces the chance for recombination.

Surface states is also a problem for photoelectrodes, which can negatively affect the electron transfer at the semiconductor-electrolyte interface.[9] It is caused by the termination of the crystal lattice at the electrode surface, where the dangling bonds can interact with energy levels between band edges.[50] In such a case, surface states would behave as local recombination centers for electron and holes, and compete with the redox reactions.[51, 52]

1.6.3. Co-catalysts and Ohmic Contact

Some of the electrocatalysts developed for EC systems can be directly incorporated onto semiconductor photoelectrode as co-catalysts to lower the significant kinetic barriers.[53] Besides, metal co-catalysts with appropriate work function can serve as trapping sites for electrons and holes by forming a Schottky barrier with the semiconductor, thereby promoting the charge separation.[54] When loading co-catalyst onto photoelectrodes, size, loading amount, and dispersity should be carefully controlled as light could be blocked due to oversized particles and excessive loading amount.[53]

Similar to EC systems, PEC systems require the electrodes to be connected via an external circuit. Here, the connection between the metal wire and photoelectrode must have an ohmic contact to optimize charge carrier transfer. Otherwise, a junction resistance will exist which may rectify the photo-separated charges back to the semiconductor bulk.[55] Metal with work function (Φ_M) larger than semiconductor work function (Φ_S) can be used for p-type photocathode, and the opposite applies to n-type photoanode. Also, metal alloys can also be used to form an ohmic contact, such as Ga-In eutectic, which is used in this work.

1.6.4. Figure of Merits in PEC CO_2 Reduction

In addition to previously mentioned criteria for EC CO_2 reduction, an adequate PEC system should evaluate the following figure of merits. At the current stage, PEC CO_2 reduction research work across different groups are challenging to compare because little benchmark has been established (such as experimental conditions and cell setup).

Photocurrent Density

In PEC systems, photocurrent density (J_{ph}) measured in mA cm^{-2} is the difference between the current density under illumination (J_{light}) and under dark (J_{dark}) at a given voltage, and is defined by:

$$J_{ph} = J_{light} - J_{dark} \tag{1-11}$$

This photocurrent is an entirely trivial value because it is determined by the source light intensity and spectrum and should not be used to compare across different research work. System efficiency, such as solar-to-fuel efficiency, is more appropriate when evaluating the performance of a system.

Quantum Efficiency

The quantum efficiency, usually reported as the incident photon-to-current efficiency (IPCE), measures the conversion efficiency of the incident light to the photocurrent. The equation for calculating IPCE is defined by:

$$IPCE(\lambda) = \frac{J_{ph} \times 1239.8\ V \cdot nm}{P_{mono} \times \lambda} \quad (1\text{-}12)$$

where 1239.8 V·nm is the product of Planck's constant (h) and the speed of light (c), P_{mono} is the power density of monochromatic light with a specific wavelength (λ). In this thesis, the IPCE was not considered due to lack of an IPCE measuring equipment.

Solar-to-Fuels Efficiency

When solar energy is the only input to produce fuel, the system efficiency is calculated by solar-to fuels efficiency (η_{STF}), and is defined as:

$$\eta_{STF} = \frac{J_{op}(\sum_j E_{eq} \cdot FE_j)}{P_{solar}} \quad (1\text{-}13)$$

where J_{op} is the operating current density in mA cm^{-2}, E_{eq} is the equilibrium potential in V (i.e. for overall water splitting, E_{eq} = 0 V (HER) + 1.23 V (OER) = 1.23 V), FE_j is the faradaic efficiency of a given product (j) in %, and P_{solar} is the solar power density in mW cm^{-2}. However, this equation does not apply when external bias (electrical power) is applied to the system.

Photo-Assisted System Efficiency

When solar energy alone is not sufficient enough to drive the electrolyzer, and additional electrical power is required, the solar-to-fuel efficiency can no longer apply. Solar energy would only help to reduce the bias required to drive the reaction comparing

to an electrochemical system. In such a case, photo-assisted system efficiency (η_{PAE}) should be used, and is expressed as[56]:

$$\eta_{PAE} = \frac{P_{f,o}}{P_{solar}+P_{e,i}} \tag{1-14}$$

where $P_{f,o}$ is the output power contained in the chemical fuel, and $P_{e,i}$ is the input electrical power. The above equation can be further expanded as:

$$\eta_{PAE} = \frac{J_{op}(\sum_j E_{eq} \cdot FE_j)}{P_{solar}+J_{op}E_{op}} \tag{1-15}$$

where E_{op} is the operating cell voltage (V).

Stability

In addition to stability issues associated with co-catalyst, most semiconductors in direct contact with an electrolyte are also prone to decomposition induced by its reduction or oxidation by photogenerated electrons or holes.[57] This phenomenon is commonly known as photo-corrosion or photo-degradation.[9] An adequate protection layer on the semiconductor is, therefore, necessary to reduce the chance of degradation.

1.6.5. Current Status of Photoelectrochemical Reduction of CO_2

Three possible configurations are available for PEC reduction of CO_2, as shown in Figure 1-8. In photocathode-driven system (Figure 1-8A), many of the p-type semiconductors have been studied in aqueous solutions, including Cu_2O[58-60], GaP[61-64], InP[65-67], CdTe[68, 69], and Si[70-76], to name a few. However, there are still significant challenges with existing photocathodes: (1) poor stability due to photo-corrosion, (2) inferior product selectivity due to sluggish kinetics on semiconductor surface and compatibility issues between semiconductor and co-catalyst, (3) large bias potential

required to drive the reaction, and (4) toxic semiconductor materials such phosphide and arsenide.[12] On the other hand, the photoanode-driven system (Figure 1-8B) can incorporate both well-developed electrocatalysts from EC CO_2 reduction[11, 15, 18] and photoanodes from PEC water oxidation researches,[55, 77] which eliminates the direct use of photocathodes. Some of the notable n-type semiconductor photoanode include Si[78-82], $BiVO_4$[83-87], WO_3[85, 86, 88, 89], and TiO_2[90-92], which are much more stable and less toxic compared to p-type semiconductors. The third configuration is ultimately a tandem photoelectrochemical cell (Figure 1-8C), which incorporates both p-type photocathode and n-type photoanode to achieve unassisted CO_2 photo-reduction and water photo-oxidation, respectively. With enough photovoltage generated, it is possible to remove the dependence of external bias entirely. However, this configuration is less studied at present date since significant research work is still focused on stand-alone photoanode or photocathode.[9, 12, 93]

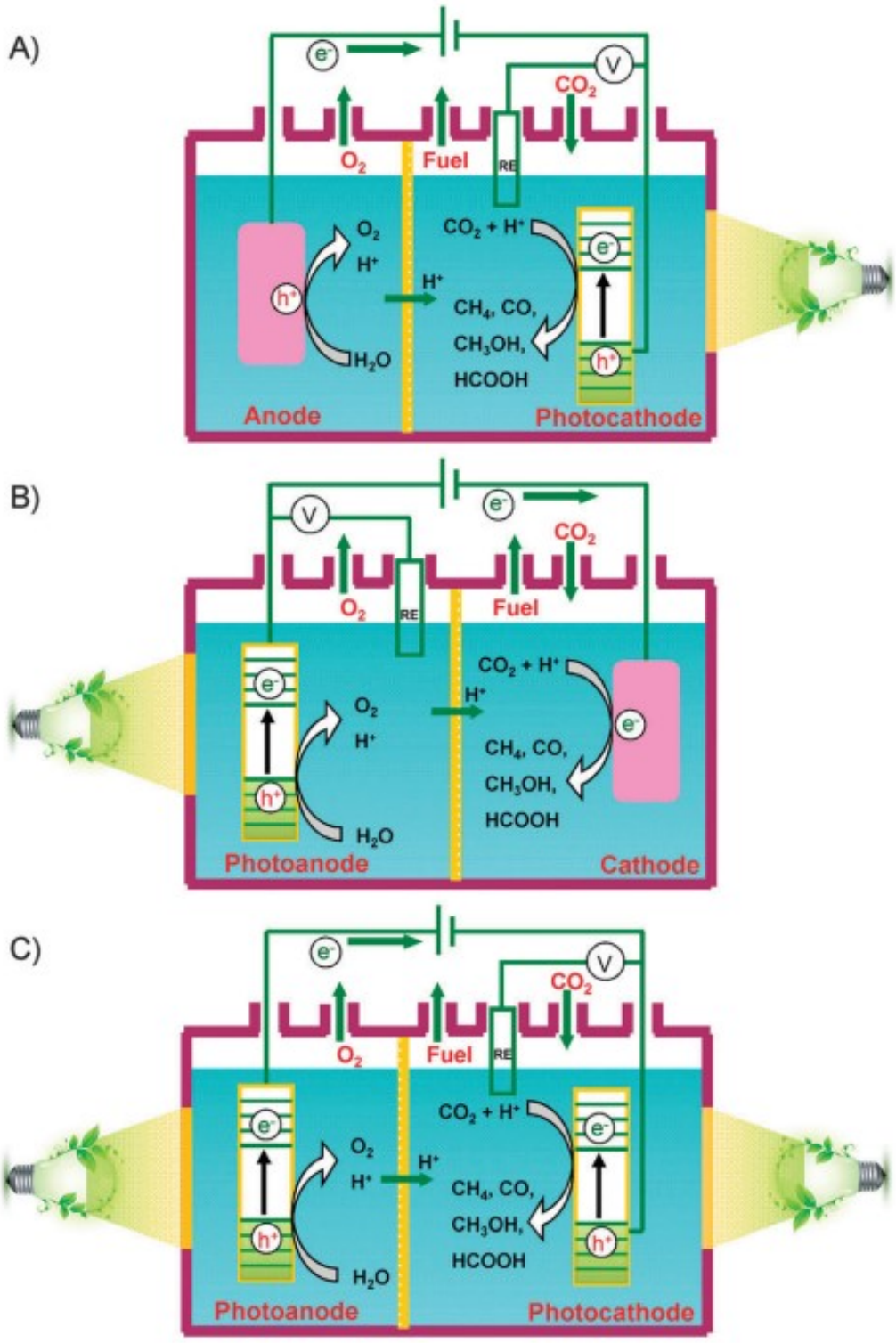

Figure 1-8. Schematic illustrations of three possible two-compartment PEC cells separated by proton-exchange membranes for the reduction of CO_2. (A) Semiconductors as photocathodes. (B) Semiconductors as photoanode. (C) Semiconductors as both photocathode and photoanodes. Reproduced with permission.[93] Copyright 2016, Royal Society of Chemistry.

1.7. Remaining Challenges and Statement of Objectives

Challenges

1) High-performance CO_2-to-CO metal electrocatalysts rely on the use of precious metals such as Ag, Au, and Pd, which are less economically feasible for industrial application.
2) Significant high overpotential is required to drive CO_2 reduction reactions, leading to increased electricity consumption and low energy efficiency.
3) Photocathode-driven CO_2 PEC systems suffer from poor stability, poor selectivity, large bias potential, and/or use of toxic materials.

Statement of Objectives

To address the above challenges, the following objectives are proposed in this thesis:

1) Develop a simple and economical method to fabricate a non-precious metal-based electrocatalyst which could achieve high CO_2-to-CO conversion efficiency, high current density, and stable operation (rate of degradation for both current density and CO faradaic efficiency should be no more than 2.5%/hour).
2) Develop a PEC system which integrates an established photoanode with the CO_2RR electrocatalyst to realize a photoanode-driven PEC system in a full cell setup. The performance of the PEC system should exhibit superior performance compared to an EC system.

Chapter 2 Experimental Framework and Methods

2.1. Material Selection and Experimental Design Framework

2.1.1. Cu-Sn Based Material as Promising CO_2-to-CO Conversion Electrocatalyst

Recently, few groups have reported that oxide derived-copper (OD-Cu) with coated a controlled amount of tin (Sn), or tin (IV) oxide (SnO_2) can significantly enhance the faradaic efficiency of copper-based electrocatalyst towards CO.[94-97] Theoretical studies suggested that the synergetic interactions between Cu and Sn atoms at the active sites have led to this enhancement.[94, 96] These Cu-Sn based catalysts demonstrated outstanding performances that are comparable to that of precious metals such as Ag, Au, and Pd. However, the underlying challenge with such modification is the lack of uniform coverage and an inexpensive fabrication method, ultimately reducing the reproducibility and scalability of the so-called "earth-abundant" catalyst. Methods such as electrodeposition,[94] electroless plating,[95] seed-mediation,[96] and atomic layer deposition[97] have been implemented to deposit Sn or SnO_2 onto OD-Cu. These fabrication methods are either energy intensive, require strict synthesis protocols, or expensive to operate. Therefore, finding an alternative deposition method to allow a simple and cheap fabrication of highly efficient Cu-Sn catalyst is showing great importance.

2.1.2. n-Si/Ni as an Efficient Photoanode

As discussed in Chapter 1.6.5, the most commonly investigated n-type semiconductor photoanode include TiO_2, $BiVO_4$, WO_3, and Si. Despite the popularity of TiO_2, its wide bandgap of around 3.2 eV can only absorb light in the UV spectrum.[91] $BiVO_4$ and WO_3 have moderate bandgaps of 2.4 eV and 2.8 eV, respectively.[85] On the

other hand, not only Silicon (Si) can absorb the largest portion of the solar spectrum with its short bandgap of 1.1 eV, it is also the only material used and produced at mass (in the photovoltaic industry), demonstrating its best technological readiness for commercial PEC application.[98] However, direct use of Si as photoanode remain challenging in three aspects: (1) sluggish reaction kinetics at silicon-liquid interface, (2) self-oxidation of Si (-0.99 V vs. Normal Hydrogen Electrode NHE) to form surface SiO_x passivation layer which leads to its deactivation under long-term operation, and (3) instability of Si due to spontaneous chemical etching in alkaline conditions.[82] As such, almost all Si-based photoanodes encompass one or multiple conformal protective layers to avoid direct contact with electrolyte.[81]

Most notable protection strategies used for stabilizing Si photoanode include atomic layer deposition (ALD) of TiO_2 [99, 100] and vapor deposition of Ni/NiO_x [78-81] thin films. Despite TiO_2 protective layer can significantly improve stability, the extremely high material, capital, and operating costs associated with ALD cannot be economically justified in large scale PEC applications. Besides, another co-catalyst layer is usually required over of TiO_2 layer to facilitate oxygen evolution reaction, further increases material cost. In contrast, nickel's excellent corrosion resistance and catalytic activity enable it to act as both a protective layer and an adequate OER co-catalyst,[80] ultimately simplifying the overall fabrication process.

For uniform and dense coverage of Ni thin film, pulse laser deposition (PLD) and sputtering deposition techniques have been used.[78, 80, 81] Previous work demonstrated that coating a thin layer (~2 to 20 nm) of Ni which has shown stable PEC operation in 1 M KOH for over 24 hours.[80] In this thesis, DC Magnetron Sputtering (Bob Sputtering,

NanoFAB, University of Alberta) was used to deposit ~15 nm of Ni on the silicon substrate. Magnetron sputtering technique has the advantage of better film adhesion due to the high kinetic energy of impacting target atoms, which is critical for the stability of Si photoanode.

2.1.3. Experimental Design Framework

Figure 2-1 outlines the experimental design framework in this thesis.

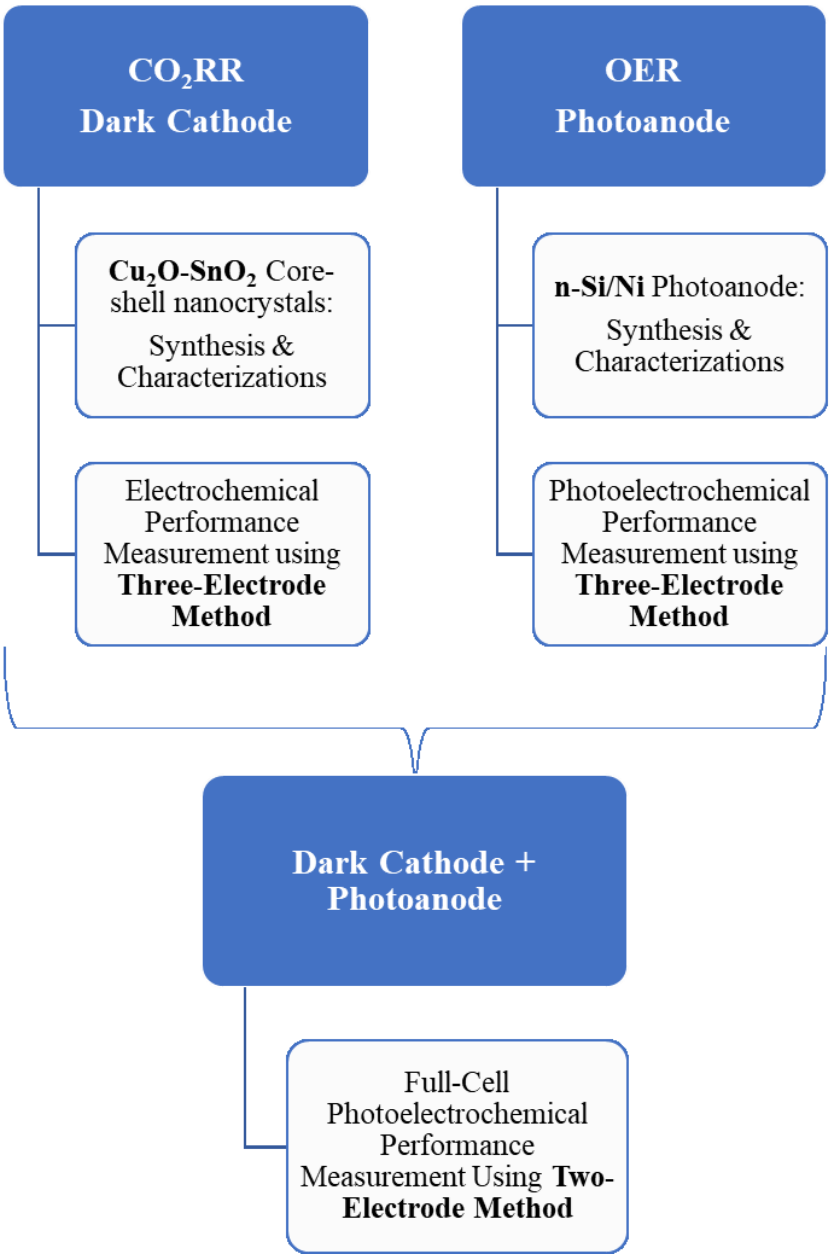

Figure 2-1. Experimental Design Framework.

2.2. Material Synthesis and Electrode Fabrication

2.2.1. Materials

$CuCl_2 \cdot 2H_2O$ (>99.0% purity), $SnCl_4 \cdot 5H_2O$ (>98.0% purity), NaOH (>97.0% purity), L-Ascorbic Acid (>99.0% purity), $KHCO_3$ (99.7 to 100.5% purity), KOH (>85% purity) were purchased from Fisher Scientific Inc. Carbon Paper (Toray 060) and Carbon Black (Vulcan XC 72) were purchased from Fuel Cell Store. IrO_2 (99% purity), Nafion membrane (Nafion N-117), and Nafion solution (5 wt%, Nafion D-520 dispersion) were purchased from Alfa Aesar. Double-sided polished n-type Si wafers (525 µm thick, (100)-oriented, 1-10 Ω cm^2) and single-sided polished degenerate n-type Si wafers (525 µm thick, (100)-oriented, 0.001-0.005 Ω cm^2) were acquired from UniversityWafer Inc. The Ga/In eutectic (>99.99% trace metals basis) was purchased from Sigma Aldrich. High-purity CO_2 (99.99%) was acquired from Praxair Canada Inc, Canada.

2.2.1. Synthesis of Cu_2O-SnO_2 Core-Shell Nanocrystals

The preparation of the Cu_2O-SnO_2 core-shell catalyst is achieved in two steps: (i) synthesis of Cu_2O cubic nanocrystals through a wet precipitation method,[101] and (ii) fabrication of SnO_2 shell layer via coordinating etching method with some modifications.[102] All the procedures below were carried out at room temperature and under vigorous stirring.

To obtain Cu_2O octahedral nanocrystals, 10.0 mL of 2.0 M NaOH solution was added dropwise into an aqueous solution of $CuCl_2 \cdot 2H_2O$ (0.01 M, 100 mL). After stirring for 30 minutes, 10.0 mL of 0.6 M Ascorbic acid solution was added dropwise and then aged for 3 hours. The precipitates were collected by vacuum filtration, followed by washing

with distilled water three times and absolute ethanol twice to remove impurities, and finally dried in vacuum at 60 °C for 12 hours.

To fabricate the SnO_2 shell layer, 50 mg of Cu_2O collected from the previous step was first dispersed in a solution of 50 mL ethanol and 1.5 mL of 0.2 M NaCl solution. Then, a varied amount of $SnCl_4$ dissolved in 50 mL of ethanol was added dropwise to the solution. The solution was stirred for 10 minutes before being collected by vacuum filtration, followed by washing and decantation. In this work, five samples were prepared by varying the precursor molar ratios (Cu_2O to $SnCl_4$) to 10:1, 20:1, 30:1, 40:1, and 50:1. The corresponding samples are referred to as CuSn10, CuSn20, CuSn30, CuSn40, and CuSn50.

2.2.2. Preparation of Cu_2O-SnO_2 Dark Cathode

Catalyst mixture comprising 5 mg of catalyst and 1.5 mg of carbon black support (Vulcan XC 72), was dispersed in a 650 μL solution that contains 65 μL Nafion solution (5 wt%, Nafion D-520 dispersion), 455 μL IPA, and 130 μL DI water to form a homogenous ink after at least 1 hours of ultrasonication. Then, 100 μL of the ink was drop-casted onto a 1 cm x 1 cm piece of carbon paper (Toray 060, FuelCellStore) to achieve a catalyst loading (catalyst + carbon black support) of 1 mg cm^{-2}. The loading amount of 1 mg cm^{-2} is referenced to previous work.[96]

2.2.3. Deposition of Ni Thin Film via DC Magnetron Sputtering

Double-sided polished n-type Si wafers (525 μm thick, (100)-oriented, 1-10 Ω cm^2, UniversityWafer Inc.), were first cleaned in piranha, BOE solutions to remove the organic contaminants and native oxide, respectively, followed by blow drying with N_2. The wafer was immediately transferred into a planar DC magnetron sputtering system (Bob

Sputtering, NanoFab, University of Alberta). Ni target and the parameters used for deposition are listed in Table 2-1. Approximately 15 nm of Ni was deposited onto the wafer. Figure 2-2 shows a schematic of the deposition process inside the sputter system.

Table 2-1. Magnetron sputter system parameters for the deposition of Ni

Parameters	
Target gun number	#3
Chamber base pressure	$1.0 * 10^{-6}$ torr
Ar gas pressure	$7.0 * 10^{-3}$ torr
Substrate rotation speed	3
Average deposition rate	9.2 nm/min (Ni)
Deposition time	98s
Film thickness	~15 nm

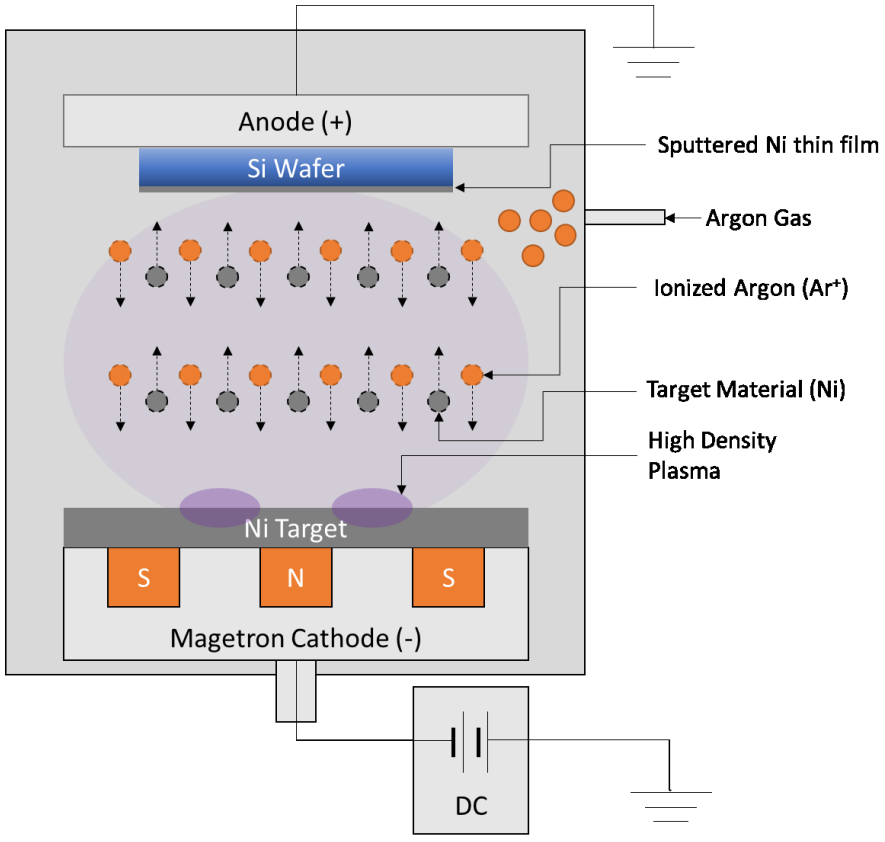

Figure 2-2. Schematic of magnetron sputter system depositing Ni thin film onto a silicon wafer.

2.2.4. Preparation of n-Si/Ni Photoanode

After the deposition of the Ni layer, the silicon wafer was then cleaved into small pieces of ~1.1 cm x 1.1 cm for electrode preparation. The backside of the n-Si/Ni was scratched using a scriber with a diamond tip to remove the oxide layer, then Ga/In eutectic alloy was immediately applied onto the scratched area form an ohmic contact with Si. Silver paste and Cu wire were placed on the Ga/In eutectic to conduct current. Epoxy was used to cover the back and edges of the photoanode to prevent direct contact of backside and electrolyte. The final geometric surface area of the photoanode is approximately 1.0 cm^2.

A heavily-doped (degenerate) n-type Si (denoted as n++-Si, 525 μm thick, (100)-oriented, 0.001-0.005 Ω cm^2, UniversityWafer Inc.) deposited with same Ni layer was also prepared using the above procedures and was used as a conducting dark anode for comparing with n-Si photoanode.

2.2.5. Preparation of Commercial IrO_2 OER Anode as Benchmark

A commercial IrO_2 OER catalyst (99% purity, Alfa Aesar) was also prepared through ultrasonication of 10 mg catalyst powder with 10 mg of carbon black support in 1 mL solution that contains 100 μL Nafion solution (5 wt%, Nafion D-520 dispersion) and 900 μL IPA for one hour, followed by drop-casting 100 μL of this solution onto a 1 cm x 1 cm piece of carbon paper (Toray 060, FuelCellStore). The carbon supported IrO_2 serves as a dark anode and is used for the benchmark comparison.

2.3. Material Characterization

2.3.1. X-Ray Diffraction Analysis

The Cu_2O and Cu_2O-SnO_2 catalyst materials were subjected to X-ray diffraction analysis (XRD, Rigaku Ultima IV) using Co Kβ radiation generated at 38 kV and 38 mA. The scan rate was 2° $min^{-1,}$ and the scan range was set between 20° to 100°.

2.3.2. X-Ray Photoelectron Spectroscopy

X-ray photoelectron spectroscopy (XPS) was performed using a Kratos AXIS system to evaluate the chemical states of Cu_2O-SnO_2 and n-Si/Ni. A monochromatic Al Kα source (hν = 1486.6 eV) was used with a power of 210W and a based pressure of 3×10^{-8} Pa in the analytical chamber. All the spectroscopies were referenced to the C1s binding energy of 284.6 eV and fitted using Gaussian-Lorentzian peak shapes and Shirley baselines.

2.3.3. Inductively Coupled Plasma Mass Spectrometry

Inductively coupled plasma mass spectrometry (ICP-MS) was performed to quantify the composition of Cu_2O-SnO_2 catalyst powders using a Quadrupole ICP-MS. Each sample was prepared by dissolving 1 mg of catalyst powder in 2 mL of 30% HNO_3 before being submitted for analysis.

2.3.4. Scanning Electron Microscope

SEM images were taken with a high-resolution Zeiss Sigma 300 VP-Field Emission Scanning Electron Microscopy (FESEM) equipped with an EDS detector.

2.3.5. Transmission Electron Microscope

TEM, HR-TEM, HAADF, and STEM-EDX were taken using a JOEL JEM-ARM200CF Field Emission Transmission Electron Microscopy (FETEM) with a 200-kV accelerating voltage and a Hitachi H-9500 environmental transmission electron microscope (ETEM) with a 300-kV accelerating voltage.

2.4. Photoelectrochemical and Electrochemical Measurements

2.4.1. Cathode Half-Cell Measurements

The EC measurements of the dark cathode were performed in a three-electrode system controlled by an AUTOLAB workstation. The $Ag/AgCl_{sat\ KCl}$ electrode and a platinum wire were used as the reference (RE) and counter electrode (CE), respectively. A home-made two-compartment gas-tight cell with a Nafion membrane (Nafion 117) in between was used to separate the cathode and anode. A 0.1 M $KHCO_3$ (pH=6.8) or 0.5 M $KHCO_3$ (pH = 7.2) aqueous electrolyte is saturated with high purity CO_2 at 20 mL min^{-1} controlled by a mass flow controller (SLA5850, Brooks Instrument) for at least 30 minutes before each measurement and maintained after that. The outlet gas from the cathode compartment was connected to GC (Agilent 6890N) for gas quantification. The current density reported in this work was normalized to the geometric surface area. The conversion of the potential of Ag/AgCl electrode to the reversible hydrogen electrode (RHE) used the following equation:

$$E(RHE) = E(Ag/AgCl_{KCl\ sat}) + 0.059 \times pH + 0.197\ V \qquad (2\text{-}1)$$

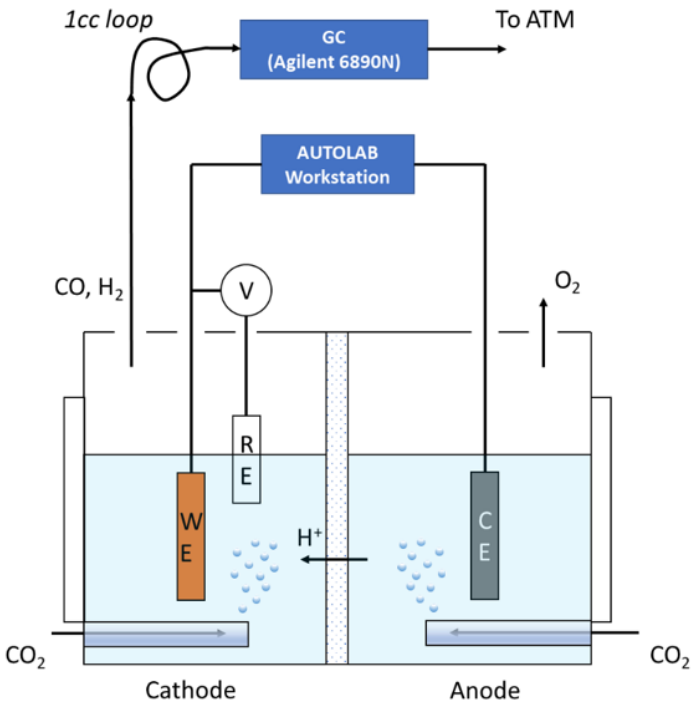

Figure 2-3. Experimental setup for EC CO_2RR test using three-electrode method.

2.4.2. Photoanode Half-Cell Measurements

The PEC measurements of the photoanode were performed in a three-electrode system controlled by an AUTOLAB workstation. The $Ag/AgCl_{sat\ KCl}$ electrode and a platinum wire were used as the reference (RE) and counter (CE) electrodes, respectively. A home-made two-compartment gas-tight cell with a Nafion membrane (Nafion 117) in between was used to separate the cathode and anode. A quartz window was equipped on each side of the compartment for optimal light transmission. A solar simulator (model SF-300-A, Sciencetech Inc.) equipped with Air Mass filter AM1.5 with an intensity of 100 mW cm^{-2} at 10 cm working distance is used as the light source. A 1 M KOH (pH = 14) aqueous electrolyte is bubbled with Ar at 20 mL min^{-1} controlled by a mass flow controller (SLA5850, Brooks Instrument) for at least 10 minutes to remove the residual O_2 and maintained after that.

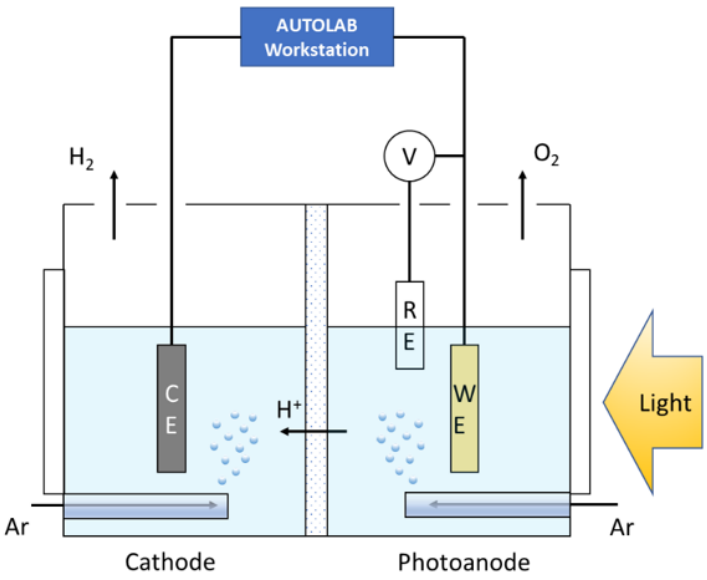

Figure 2-4. Experimental setup for PEC OER test using three-electrode method.

2.4.3. Full Cell Measurements

The PEC measurements were performed in a two-compartment cell with a quartz window on each side for optimal light transmission. The two-electrode system was controlled by an AUTOLAB workstation and was consist of the n-Si/Ni photoanode (WE) and the best Cu_2O-SnO_2 dark cathode (CE) determined from electrochemical measurements. The outlet gas from the cathode compartment was connected to GC (Agilent 6890N) for gas quantification. The catholyte is CO_2-saturated 0.5 M $KHCO_3$ (pH = 7.2), and the anolyte is 1 M KOH (pH = 13.6). A solar simulator (model SF-300-A, Sciencetech Inc.) equipped with Air Mass filter AM1.5 with an intensity of 100 mW cm^{-2} at 10 cm working distance is used as the light source. For comparison, the IrO_2 commercial OER anode was also tested in conjunction with Cu_2O-SnO_2 dark cathode to evaluate the electrochemical performance of the full cell.

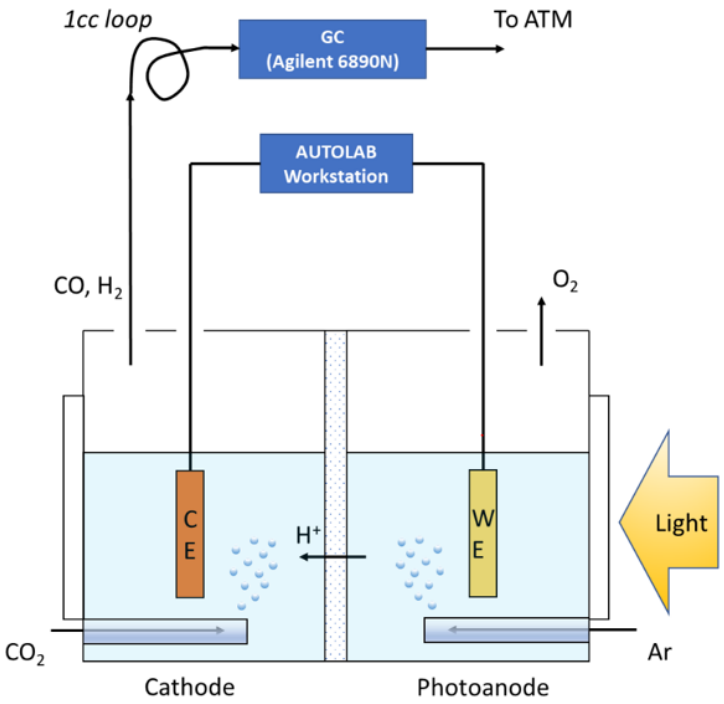

Figure 2-5. Experimental setup for PEC full cell test using two electrode method.

2.5. CO_2RR Product Quantification

2.5.1. Gas Product Quantification

The gaseous products from CO_2 reduction were measured by gas chromatography (GC, Agilent Technology 6890N) for gaseous products and. The GC has been calibrated with standard gas that contains 0.5% CO, 0.5% H_2, 0.5% CH_4, 0.5% C_2H_4, 0.5% C_2H_6 and balance CO_2 (97.5%), with more detail shown in Appendix B. The gas outlet from the catholyte was connected to the GC which operates an automatic valve injection (1 cc sample) and a thermal conductivity detector (TCD) and flame ionization detector (FID). Argon (99.999%, Praxair) was used as the carrier gas. During each chronoamperometric measurement, the product gas from the cell was injected after 5 minutes and again three times at 8.4 minutes interval to ensure the accuracy of the measurement. A step-by-step

procedure is included in Appendix A. The faradaic efficiency of gas products was calculated using the following equation:

$$FEj = \frac{\alpha F V v p_o}{R T_o I_{total}} \times 100\% \quad (2\text{-}2)$$

where

α = number of moles of electrons consumed per one mole of the product (e.g., α=2 for CO and H_2)

v (vol%) = volume concentration of CO or H_2 in the exhaust gas from the cell (measured from GC results)

V (mL/min) = gas flow rate, assumed 20 mL min^{-1}

I_{total} (A) = steady-state cell current

2.5.2. Liquid Product Quantification

The liquid products were measured by nuclear magnetic resonance (NMR, VNMRS 600 MHz) spectroscopy. For ^1H NMR spectroscopy analysis of the liquid phase, samples were prepared by mixing 500 μL of the electrolyte with 200 μL of D_2O solution that contains 2.816 μM of DMSO internal standard. A calibration curve was obtained for the NMR signals of formate and DMSO using six standard solutions, as shown in Appendix B.

The slope of the calibration curve was determined to be 0.02826 mM^{-1}. Using the calibration curve, we can obtain the concentration of formate in the catholyte using:

$$Formate\ Concentration\ (mM) = \frac{RA}{0.02826\ mM^{-1}} \quad (2\text{-}3)$$

The total volume of catholyte in the cathode compartment is 0.030 L. Therefore, the number of moles of formate in the cathode compartment is calculated as:

$$n_{HCOO^-} = 0.030\ L \times Formate\ concentration\ (mM) \div 1000 \quad (2\text{-}4)$$

The faradaic efficiency of formate is then calculated by:

$$FE_{HCOO^-} = \frac{2 * n_{HCOO^-} * 96485}{Q_{total}} \times 100\% \quad (2\text{-}5)$$

where Q_{total} is the total number of charges in Coulomb (C) during the photo/electro-reduction of CO_2.

Chapter 3 Results and Discussions

3.1. Cu_2O-SnO_2 Core-Shell Nanocrystal as CO_2-to-CO Electrocatalyst

The main results in Chapter 3.1 of this thesis have been published in *ChemCatChem* (DOI:10.1002/cctc.201900395), titled "A Rational Design of Cu_2O-SnO_2 Core-Shell Catalyst for Highly Selective CO_2-to-CO Conversion". This published work has been reproduced with permission from Wiley-VCH, Copyright 2019.

3.1.1. The Effectiveness of the Synthesis Strategy

The Cu_2O-SnO_2 core-shell cubic nanocrystals were synthesized via a two-step process that is facile and scalable as illustrated in Figure 3-1. Cu_2O nanocubes were first obtained through wet precipitation synthesis at room temperature.[101] The thin layer of SnO_2 grew onto Cu_2O surfaces during the coordinating-etching process, with the overall chemical reaction described as follows:

$$SnCl_{4(aq)} + xH_2O_{(l)} + 2Cu_2O_{(s)} \rightarrow SnO_2 \bullet xH2O_{(s)} + 4CuCl_{(s)} \quad (3\text{-}1)$$

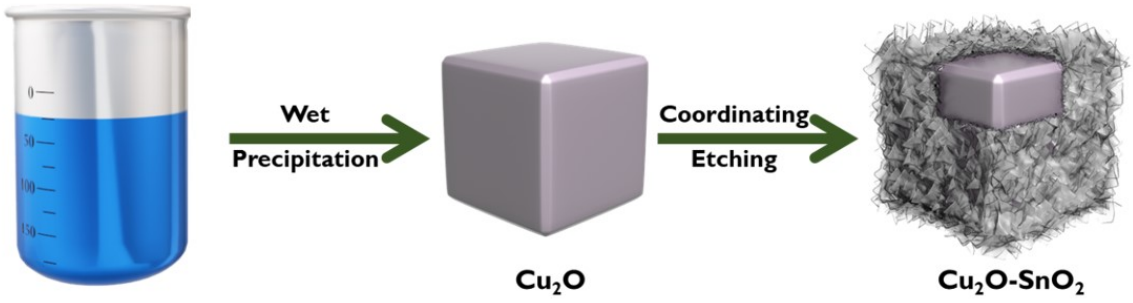

Figure 3-1. Schematic illustration the of two-step synthesis of Cu_2O-SnO_2 core-shell catalyst.

As previous reports found that the SnO_2 shell layer plays a vital role to the product selectivity of Cu-Sn based catalysts,[95-97] it is necessary to develop a low cost and

effective strategy for controlling the SnO_2 shell thickness. In this work, the control strategy was achieved by adjusting the Cu_2O to $SnCl_4$ precursor molar ratios during the second synthesis step, where ratios of 10:1, 20:1, 30:1, 40:1, and 50:1 were used. The resulting catalysts were labeled as CuSn10, CuSn20, CuSn30, CuSn40, and CuSn50, respectively. The measured bulk Cu to Sn molar ratios from the as-synthesized catalysts were quantified using inductively-coupled plasma mass spectrometry (ICP-MS) and are shown in Table 3-1. As shown in Table 3-1, although the measured ratios are slightly lower than the prediction, the amount of formed SnO_2 can be easily controlled by adjusting its precursor content.

Table 3-1. Measured Cu and Sn bulk concentrations in Cu_2O-SnO_2 catalysts and their respective molar ratios from ICP-MS results.

Catalyst Label	Measured Cu (mol%)	Measured Sn (mol%)	Predicted bulk Cu:Sn Ratio	Measured bulk Cu:Sn Ratio
CuSn10	88.23%	11.77%	10	7.5
CuSn20	94.66%	5.34%	20	17.7
CuSn30	96.23%	3.77%	30	25.5
CuSn40	97.19%	2.81%	40	34.6
CuSn50	97.86%	2.14%	50	45.8

To confirm the validity of the coordinating etching reaction process, the composition of remaining solvent (supernatant) from the synthesis of Cu_2O-SnO_2 powders was also analyzed using ICP-MS. Because ICP-MS cannot directly analyze content inside an organic solvent (ethanol, in this case), the clear supernatant of the solvent was first

evaporated and subsequently redissolved in dilute HNO_3. ICP-MS results showed that Cu and Sn ions mol% present in the solvent are 99.65% and 0.35%, respectively. Because Cu_2O and SnO_2 are not soluble in ethanol, the high Cu content is suspected to be the dissolved CuCl. The trace Sn content may be the remaining unreacted $SnCl_4$.

3.1.2. Crystal Phase and Chemical State of Cu_2O-SnO_2

To reveal the crystal phase and chemical state of synthesized Cu_2O-SnO_2 core-shell catalysts, characterizations were conducted on CuSn10. The X-ray diffraction (XRD) patterns of Cu_2O and Cu_2O-SnO_2 core-shell catalysts are shown in Figure 3-2. Both materials show identical characteristic peaks, which can be identified as Cu_2O (JCPDS 01-078-2076). The consistency in XRD patterns indicates that Cu_2O maintained its crystal structure after the growth of SnO_2 shell layer.

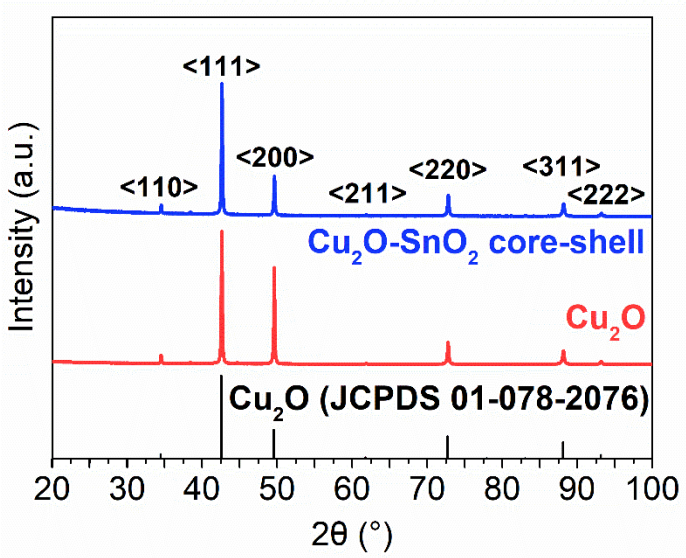

Figure 3-2. XRD patterns of Cu_2O and Cu_2O-SnO_2 core-shell crystal (2θ = 20° - 100°).

The chemical state of Cu was investigated by X-ray photoelectron spectroscopy (XPS). The Cu2p XPS spectrum for Cu_2O-SnO_2 (Figure 3-3A) indicates the presence of

two oxidation states, Cu^{2+} and Cu^{1+}, positioned at 934.5 and 932.5 eV in the $Cu2p_{3/2}$ spectra, respectively.[103] Despite the presence of satellite peaks (which is indicative of strong Cu^{2+} oxidation state)[97] due to partial surface oxidation, the bulk material is still considered Cu_2O based on XRD results. The oxidation of Cu_2O surface layer into CuO may be caused by exposing the catalysts to ambient air during and after synthesis.[103] Additionally, no diffraction peak of SnO_2 could be found in the XRD pattern, which may be attributed to the low SnO_2 content as well as its amorphous nature. The presence of SnO_2 was confirmed by XPS, as shown in Figure 3-3B. The Sn3d spectrum of Cu_2O-SnO_2 core-shell crystal shows a single Sn3d doublet at 486.6 and 495.0 eV. The Sn 3d peaks can be assigned to Sn^{4+}, in agreement with previous works. [95, 96]

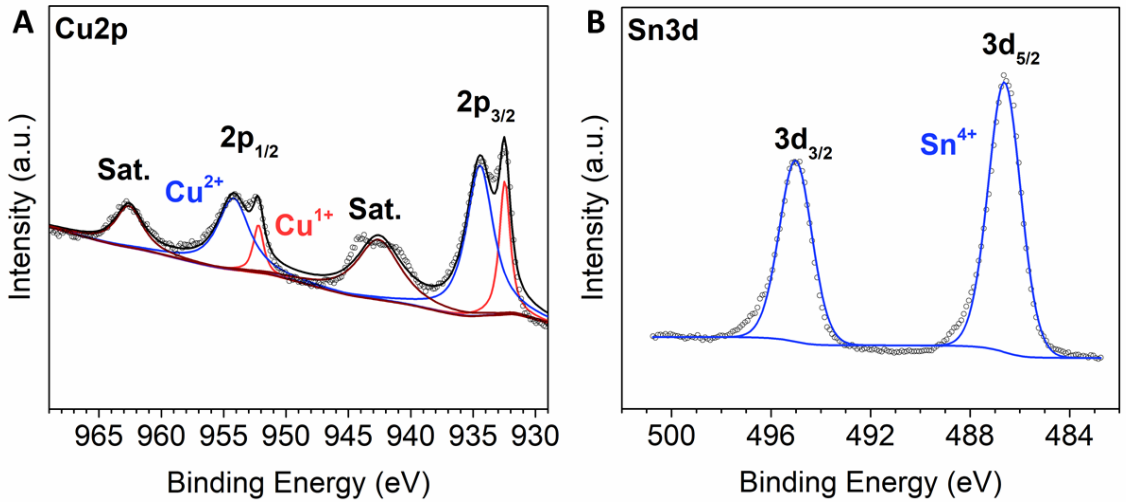

Figure 3-3. (A) Cu2p XPS spectrum of Cu_2O-SnO_2 core-shell crystal, (B) Sn3d XPS spectrum of Cu_2O-SnO_2 core-shell crystal.

High-resolution transmission electron microscopy (HR-TEM) image (Figure 3-4) revealed that the SnO_2 at the shell layer shows no evidence of long-range crystal order, which confirms its amorphous nature.

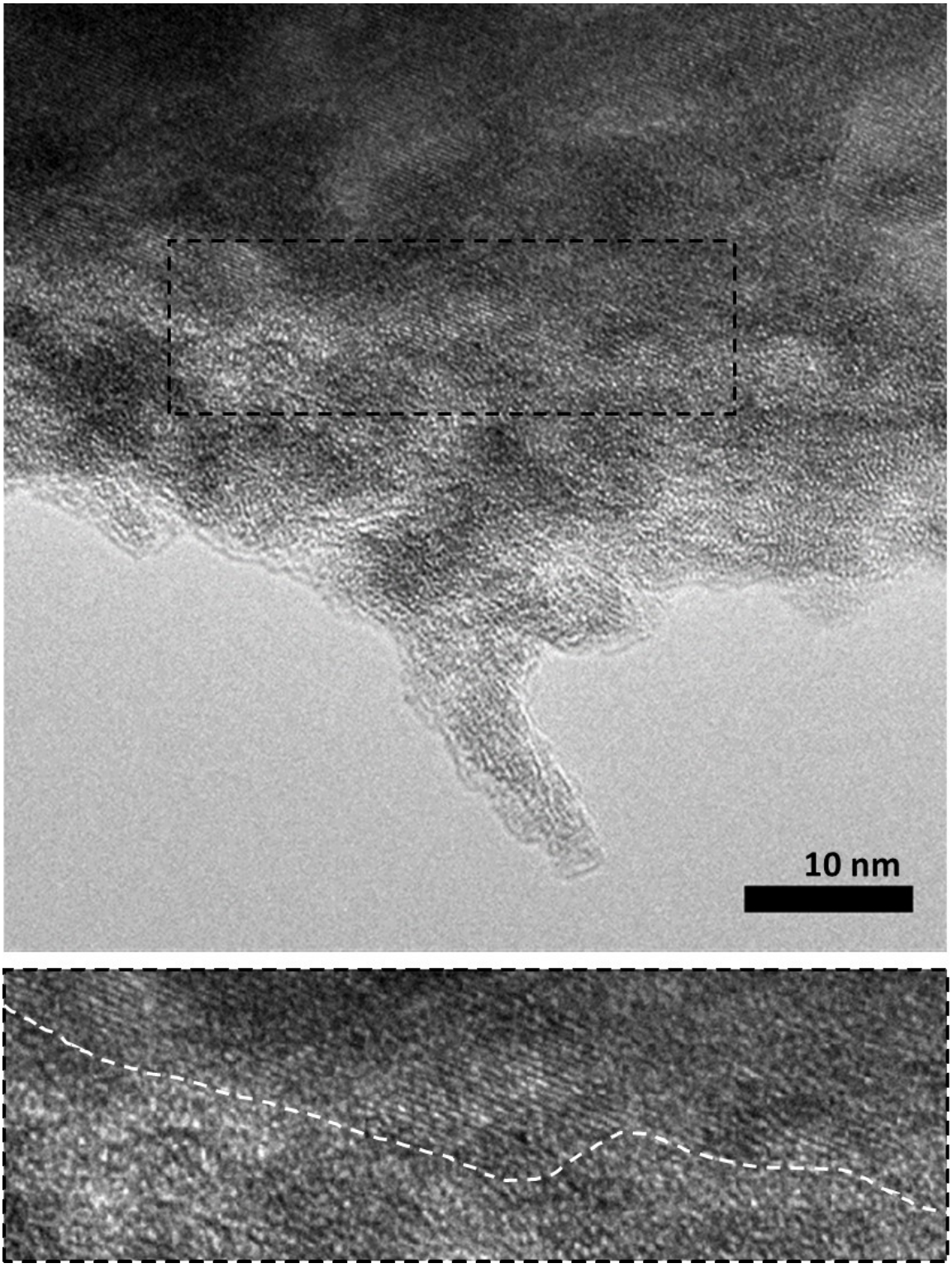

Figure 3-4. HR-TEM image at the catalyst shell layer. Inset shows a clear boundary between crystalline core and amorphous shell.

3.1.3. Morphology Evolution of Cu_2O-SnO_2 Nanocrystals

The morphology evolution of Cu_2O to Cu_2O-SnO_2 nanocrystals, as well as various SnO_2 shell thickness, were characterized by scanning electron microscopy (SEM), transmission electron microscopy (TEM), scanning transmission electron microscopy-energy dispersive X-ray spectroscopy (STEM-EDX).

As shown in Figure 3-5, the surfaces of Cu_2O nanocrystals (Figure 3-5A,B) transformed from relatively smooth to having considerable roughness after the growth of SnO_2 shell layer, while the Cu_2O cubic structure was well maintained (Figure 3-5C,D,E,F). It should be noted that when higher Sn precursor amount was used, the SnO_2 does not only form on the shell side of Cu_2O but also tend to self-aggregate and form clusters on its own.[102] For this work, since a limited amount of Sn precursor was used, only slight SnO_2 self-aggregation was observed (Figure 3-5C,D).

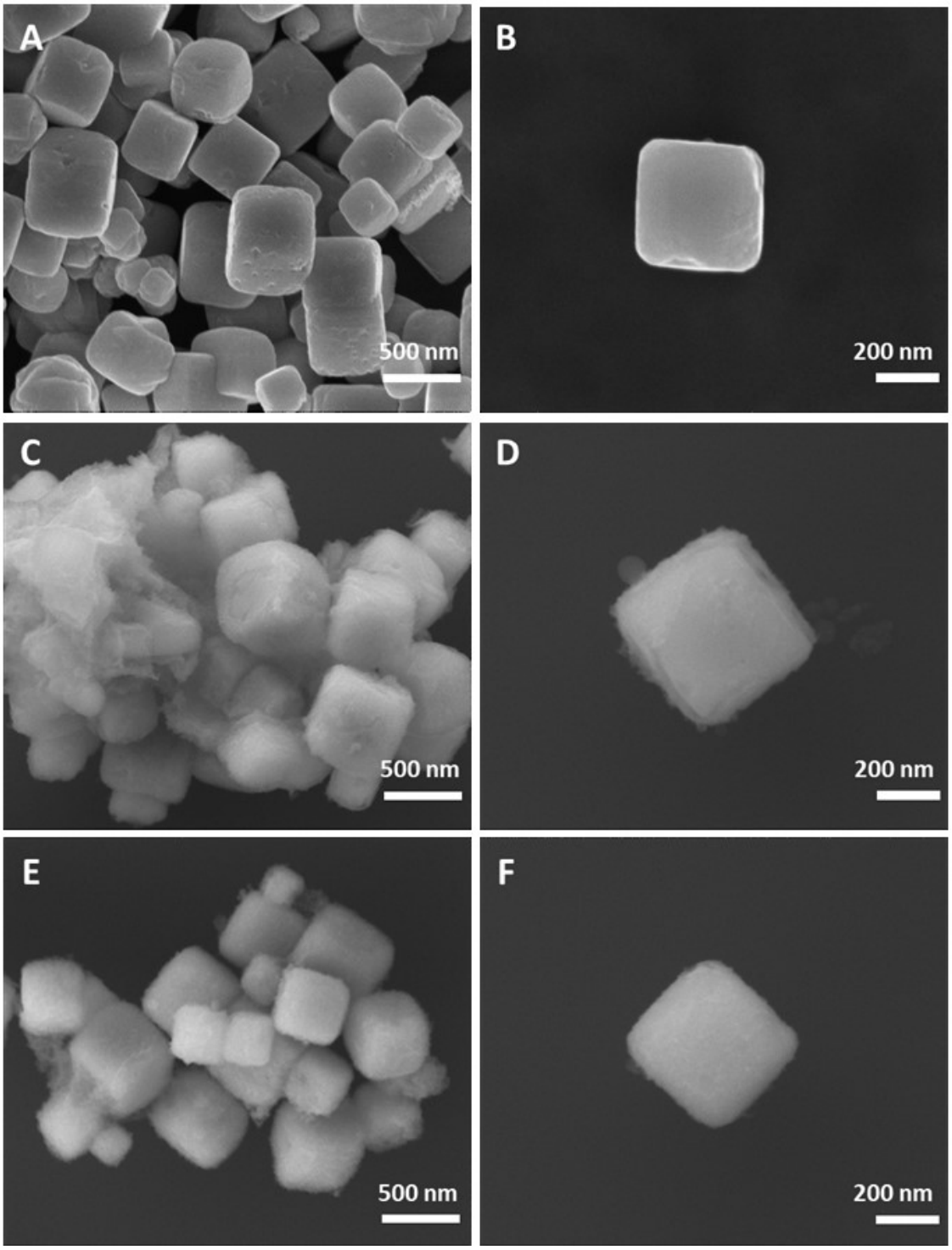

Figure 3-5. SEM images of (A,B) Cu_2O nanocubes, (C,D) CuSn10, and (E,F) CuSn40.

Figure 3-6 and Figure 3-7 show the TEM, high-angle annular dark-field (HAADF) image and STEM-EDX mapping of the CuSn10 and CuSn40, respectively. From the

STEM-EDX images, the SnO_2 is uniformly distributed on the shell layer, demonstrating the effectiveness of our synthesis strategy. By comparing both STEM-EDX images of CuSn10 (Figure 3-6) and CuSn40 (Figure 3-7), it is obvious that the shell thickness indeed has shown dependence on the amount of Sn precursor used. For instance, the CuSn10 has a thicker shell of 20 nm than to that of CuSn40 with a thickness of 5 nm. Therefore, it is feasible to optimize the thickness of the SnO_2 shell by changing the content of Sn precursor. HR-TEM result also revealed that the SnO_2 at the shell layer shows no evident long-range crystal order, which confirms its amorphous nature.

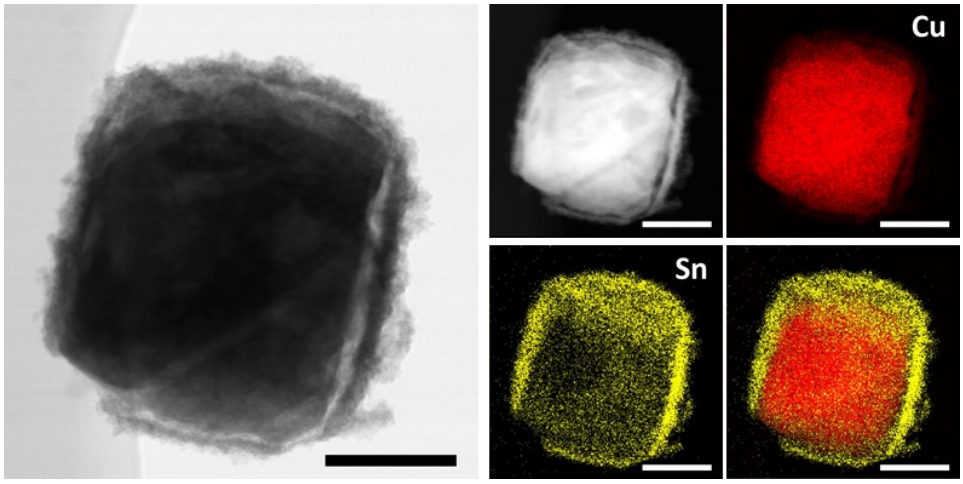

Figure 3-6. TEM, HAADF, STEM-EDX images of CuSn10. Scale bar is 100 nm.

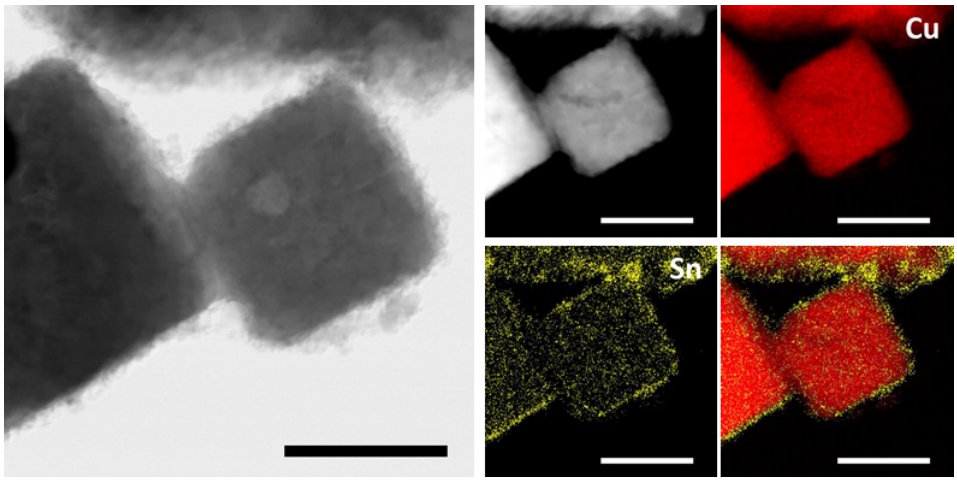

Figure 3-7. TEM, HAADF, STEM-EDX images of CuSn40. Scale bar is 100 nm.

3.1.4. Electrochemical CO_2RR Performance in 0.1 M $KHCO_3$

The performance of Cu_2O-SnO_2 catalysts with different Cu and Sn ratios were investigated using the three-electrode method with Pt as a counter electrode in 0.1 M $KHCO_3$ electrolyte. All the applied potentials described below are referenced against the reversible hydrogen electrode (RHE) unless otherwise indicated. Detailed CO_2RR gas product analysis for each catalyst is shown in Appendix A.

As Vulcan XC 72 carbon black (CB) was used as catalyst support in all samples, its CO_2RR activity should be first studied. As shown in Figure 3-8, only minor activity towards CO_2RR, yielding trace CO, CH_4, C_2H_4 at high cathodic potentials (< -0.8 V). Once CB is mixed with a catalyst, its activity becomes overshadowed by the latter and serve only as conducting material.[96] This can be explained by the disappearance of CH_4 and C_2H_4 in the product distributions from all of the Cu_2O-SnO_2 catalysts (Appendix A).

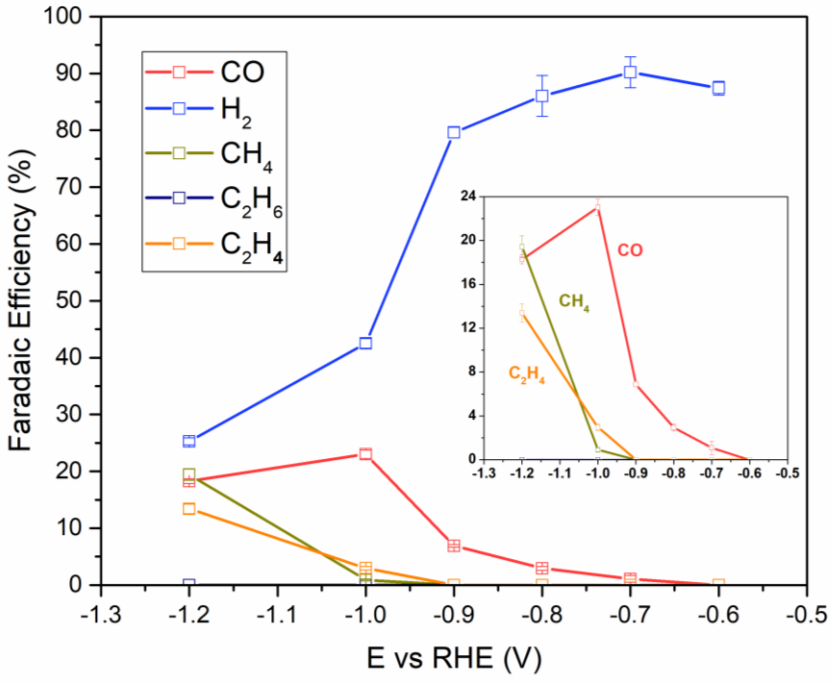

Figure 3-8. Gas product faradaic efficiency of carbon black support in 0.1 M $KHCO_3$.

Figure 3-9 shows the chronoamperometry-derived linear sweep voltammetry (LSV) measurements of carbon black support tested in CO_2-saturated 0.1 M $KHCO_3$.

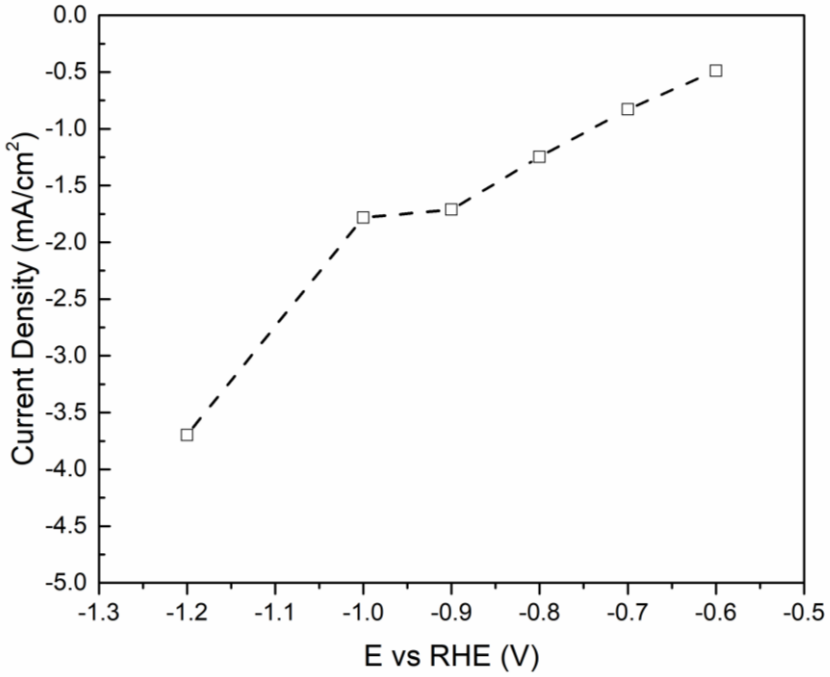

Figure 3-9. Chronoamperometry-derived LSV of carbon black support in 0.1 M $KHCO_3$.

Figure 3-10 shows chronoamperometry-derived LSV and CO Faradaic efficiency (FE_{CO}) of all tested catalysts in this work. As shown in Figure 3-10A, Cu_2O exhibit highest total current densities across the tested potential range. However, most of its current densities contribute to the competing hydrogen evolution reaction (HER) with FE_{H2} over 50% across all tested potentials, while its maximum FE_{CO} does not exceed 22% (Appendix A). On the other hand, with SnO_2 incorporated on Cu_2O, the total current density showed an apparent decrease, signifying a suppressed catalytic activity. This activity suppression can be attributed to the reduced HER, evidenced by a lower FE_{H2} measured for all Cu_2O-SnO_2 catalysts (Appendix A). As shown in Figure 3-10B, most of the Cu_2O-SnO_2 catalysts have FE_{CO} peak at -1.0 V, with CuSn40 having the highest FE_{CO} among all.

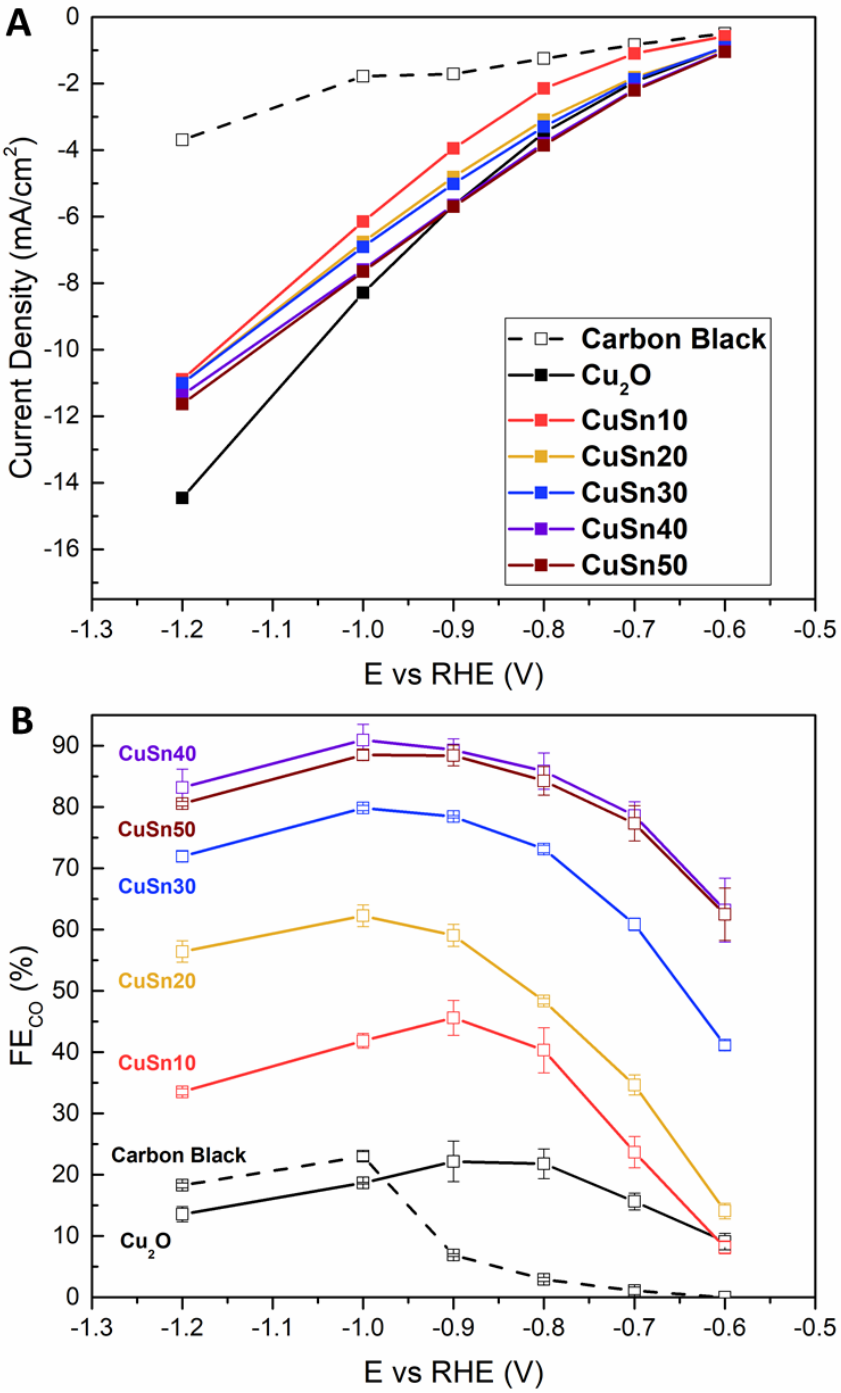

Figure 3-10. (A) Chronoamperometry-derived LSVs for all tested catalysts, and (B) Faradaic efficiency of CO (FE_{CO}) for all tested catalysts. The error bars in (B) represent one standard deviation based on three sample points.

The results above demonstrated that changing Cu to Sn content ratio in the catalyst indeed has strong effect towards the CO Faradaic efficiency. By incorporating ICP-MS measurements, the direct relationship between FE_{CO} and Sn% present in the Cu_2O-SnO_2 catalysts can be determined, shown in Figure 3-11. A sharp peak in FE_{CO} was observed at an optimal Sn mol% of ~3%, corresponding to that of CuSn40. Lower or higher mol% of Sn in the catalyst have resulted in significantly lower FE_{CO}, agreeing with trends observed from previous works.[95, 97]

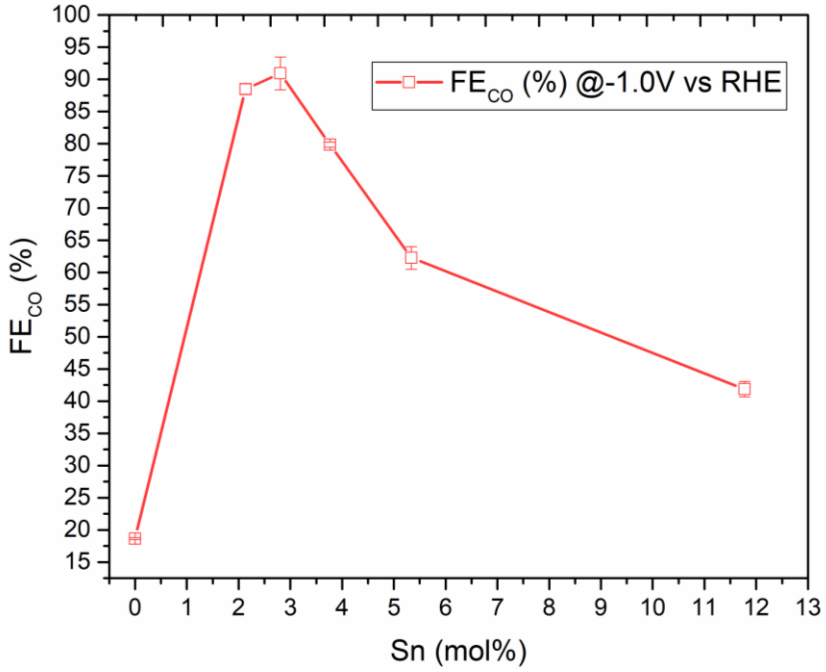

Figure 3-11. FE_{CO} at -1.0 V vs. RHE as a function of Sn mol% (measured via ICP-MS) in the Cu_2O-SnO_2 catalyst.

Figure 3-12 shows the gas product faradaic efficiencies of the best performing Cu_2O-SnO_2 catalyst (CuSn40) tested in 0.1 M $KHCO_3$. A CO faradaic efficiency (FE_{CO}) of higher than 80% (85.9%) was achieved at -0.8 V, peaked to 90.9% at -1.0 V, and deteriorated at more cathodic potentials. This trend is consistent with the potential-dependent product selectivity observed in previous CO_2RR experiments.[23, 26, 30, 31, 33,

94-97, 104] The enhanced CO_2 to CO conversion on Cu_2O-SnO_2 core-shell catalyst is believed to be a result of the synergetic interactions between Cu and Sn surface atoms, and this effect was demonstrated in two reported DFT calculations for Cu-Sn based catalyst.[94, 96]

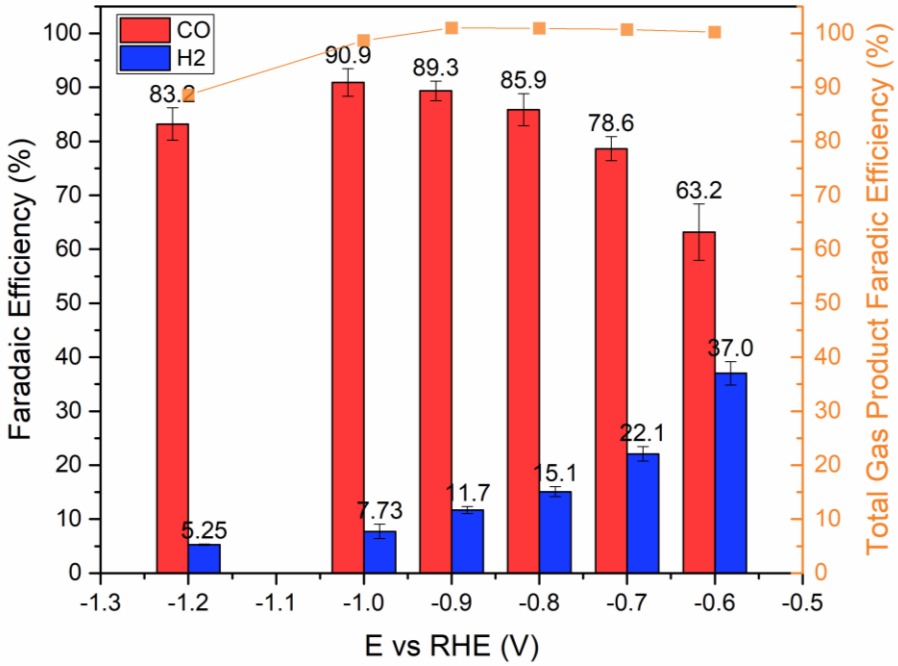

Figure 3-12. Gas product faradaic efficiencies of CuSn40 tested in 0.1 M $KHCO_3$.

3.1.5. Effect of Electrolyte Concentration

We then investigated the CO_2RR performance of CuSn40 in 0.5 M $KHCO_3$ electrolyte. Improved faradaic efficiencies and current densities were observed across all tested potentials. As shown in Figure 3-13, the FE_{CO} achieved over 90% at a potential as low as -0.5 V, which is much lower than the results obtained in 0.1 M $KHCO_3$ (Figure 3-12). Moreover, the potential window at which FE_{CO} is higher than 80% is broader in 0.5 M $KHCO_3$, expanding from -0.5 V to -1.0 V, with a peak of 94.8% at -0.8 V.

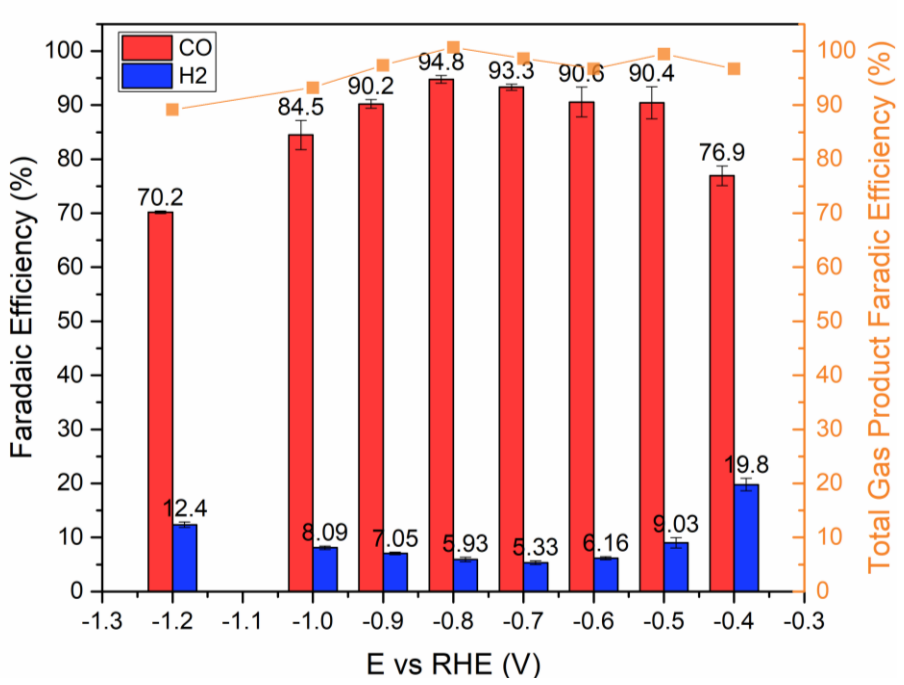

Figure 3-13. Gas product faradaic efficiencies of CuSn40 tested in 0.5 M $KHCO_3$.

For better clarity, Figure 3-14 and Figure 3-15 show the effect of electrolyte concentration (0.1 M vs. 0.5 M) on faradaic efficiencies and partial current densities, respectively. As shown in Figure 3-14, when a potential more cathodic than -1.0 V was applied, HER is more significant in 0.5 M $KHCO_3$ but suppressed in 0.1 M $KHCO_3$. This observation is also reflected in the partial current density comparisons in Figure 3-15. The partial current densities of H_2 (j_{H2}) remained less than 1 mA cm^{-2} in 0.1 M $KHCO_3$, whereas the j_{H2} in 0.5 M $KHCO_3$ begun increasing at -0.9 V and reached ~4 mA cm^{-2} at -1.2 V. On the other hand, due to higher total current densities measured in 0.5 M $KHCO_3$, the corresponding j_{CO} was also much higher. Therefore, we concluded that the overall performance of CuSn40 is better in 0.5 M $KHCO_3$ because of higher j_{CO} and a broader potential range of high FE_{CO}.

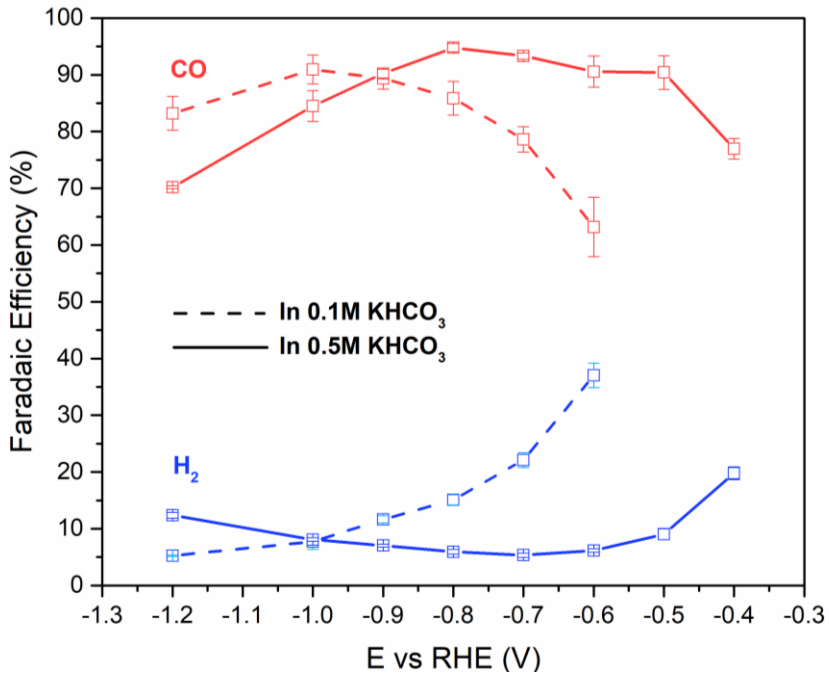

Figure 3-14. Gas product Faradaic efficiency of CuSn40 catalyst tested in 0.1 M $KHCO_3$ (dashed-line) and 0.5 M $KHCO_3$ (solid-line).

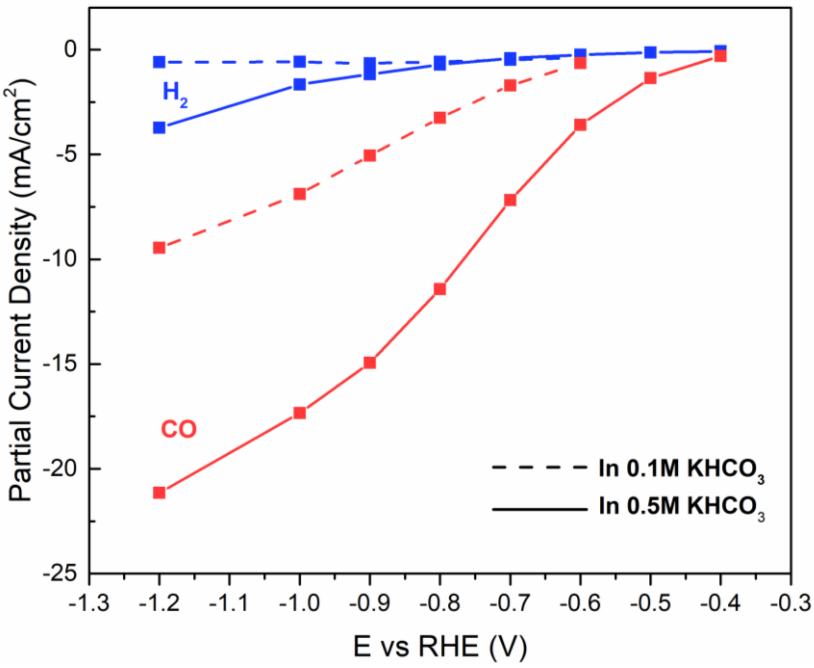

Figure 3-15. Partial current densities of CuSn40 catalyst tested in 0.1 M $KHCO_3$ (dashed-line) and 0.5 M $KHCO_3$ (solid-line).

The subsequent long-term stability test was carried out at -0.6 V for 18 hours in 0.5 M $KHCO_3$. As shown in Figure 3-16, the total current density degraded slightly in the first 8 hours, reached a plateau and remained relatively constant thereafter. The faradaic efficiencies of CO and H_2 remained stable with an average FE_{CO} of 91.0% ± 2.2% and FE_{H2} of 7.6% ± 0.6% in the first two hours. Then, the FE_{CO} and FE_{H2} were measured to be 86.1% ± 1.9% and 11.5% ± 0.9% in the final hour, respectively. The liquid product from the stability test was measured to be ~2% of formate using nuclear magnetic resonance (NMR) spectroscopy (see Appendix B for NMR chromatograph of the analyzed electrolyte). The degradation of current density and FE_{CO} during the stability test are comparable to earlier reports on Cu-Sn based electrocatalyst.[94, 95, 97]

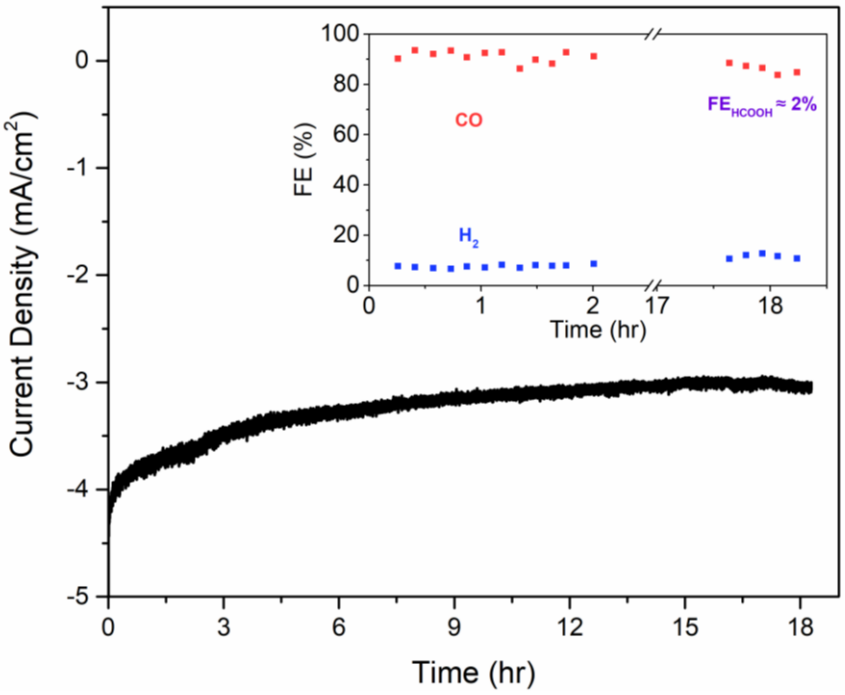

Figure 3-16. Long-term stability test of CuSn40 catalyst at -0.6 V vs. RHE for 18 hours in 0.5 M $KHCO_3$.

3.1.6. Root Cause of Catalyst Degradation

After the stability test, the CuSn40 catalyst was characterized by SEM, TEM, and STEM-EDX (Figure 3-17 and Figure 3-18). Results showed that the original cubic structure of the catalyst no longer remains and has broken down into assemblies of smaller nanoparticles with distinctive grain boundaries in between. This structure change may have exposed the subsurface Cu and greatly reduced the percentage of catalyst surface area possessing a robust Cu-Sn interface (which was believed to be main active sites for CO_2-to-CO reduction). This observation agrees with the fact that the current density and FE_{CO} was gradually decreasing during the stability test.

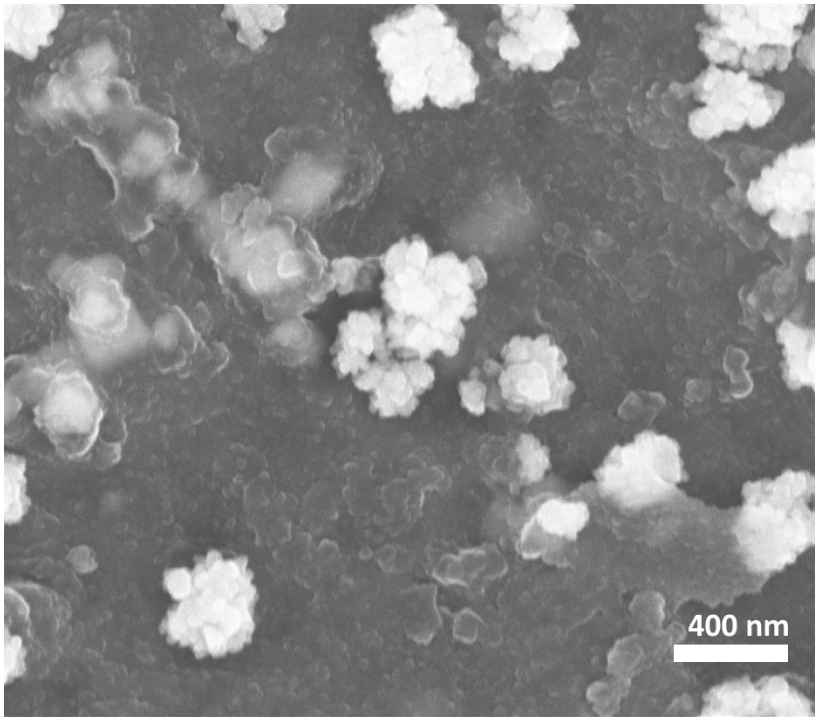

Figure 3-17. SEM image of CuSn40 catalyst after stability test. (Note some of the particles are covered by organic matters which are probably the Nafion binder used in the catalyst ink)

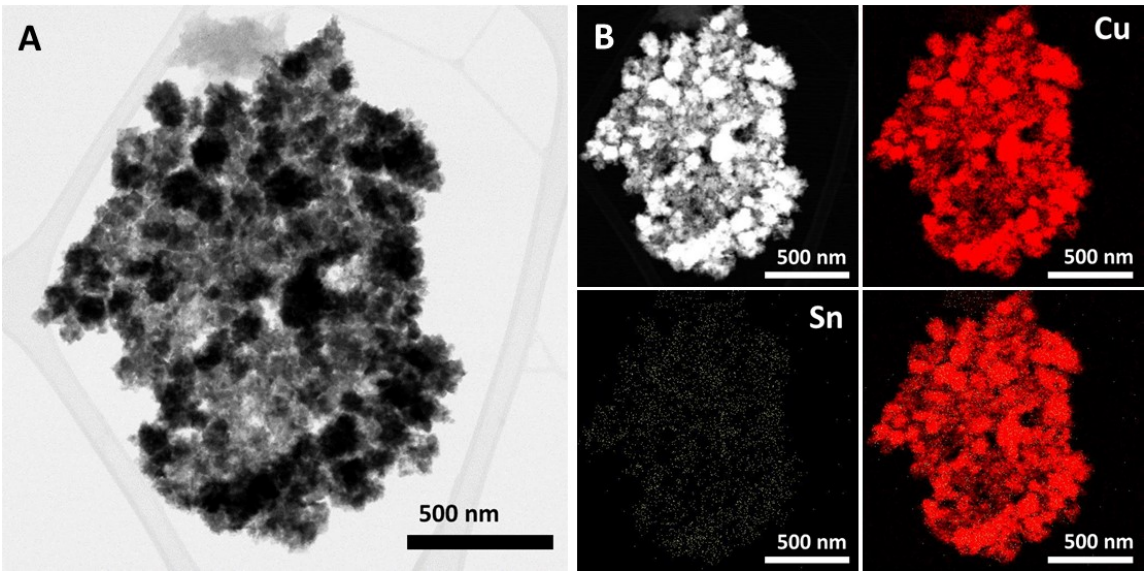

Figure 3-18. (A) TEM, and (B) HAADF and STEM-EDX images of CuSn40 catalyst after stability test.

3.1.7. Performance Comparison with State-of-the-art Cu-Sn Based Electrocatalyst

The electrochemical CO_2RR of CuSn40 catalyst in both 0.1 M $KHCO_3$ and 0.5 M $KHCO_3$ electrolytes demonstrated comparable, if not better, performances to previous Cu-Sn based catalysts,[94-97] and are summarized in Table 3-2. In 0.1 M $KHCO_3$ electrolyte, CuSn40 has a similar potential window at which FE_{CO} is higher than 80% compared to others, and it has the highest j_{CO} at -0.8 V vs. RHE. In 0.5 M $KHCO_3$, our catalyst has the broadest potential window of high FE_{CO} (> 80%) and has only slightly lower j_{CO} at -0.8V vs. RHE. Moreover, the Cu_2O-SnO_2 core-shell nanocrystals can be synthesized inside a laboratory beaker at ambient conditions without the use of surfactant or capping agent, which can be readily scaled up. All other Cu-Sn based catalysts for the same application either require more sophisticated and energy-intensive methods such as annealing[94, 95], seed-mediated synthesis in an Argon environment at elevated temperature[96], or require some form of in-situ and ex-situ deposition method such as electrodeposition[94] or atomic layer deposition (ALD)[97]. Considering both performance and cost, we concluded that

our Cu_2O-SnO_2 core-shell catalyst stands shoulder to shoulder with the state-of-the-art Cu-Sn based electrocatalysts for CO_2-to-CO conversion.

Table 3-2. Comparison of Cu_2O-SnO_2 catalyst to literature. (j_{CO}* was calculated through multiplying j_{total} by FE_{CO}, where j_{total} and FE_{CO} were interpreted directly from data plots)

Catalyst	Electrolyte	Range of E (vs. RHE) @ FE_{CO} > 80%	j_{CO} (mA cm^{-2}) @-0.8 V vs. RHE	Stability (hr)	Ref.
Cu-Sn Bimetallic	0.1 M $KHCO_3$	-0.4V to -0.8V	-3.0*	14	[94]
Cu_xO-Sn NWs	0.1 M $KHCO_3$	-0.7V to -0.8V	-2.7	12	[95]
Cu_xO-Au-Sn NWs	0.1 M $KHCO_3$	-0.8V to -0.9V	-3.2	N/A	[95]
CuO/SnO_2 NWs	0.1 M $NaHCO_3$	-0.6V to -0.8V	-1.4	6	[97]
Cu/SnO_2 NPs	0.5 M $KHCO_3$	-0.6V to -1.0V	-13.6*	N/A	[96]
Cu_2O-SnO_2 nanocrystals	0.1 M $KHCO_3$	-0.8V to -1.2V	-3.3	N/A	This work
Cu_2O-SnO_2 nanocrystals	0.5 M $KHCO_3$	-0.5V to -1.0V	-11.4	18	This work

3.2. n-Si/Ni Photoanode

3.2.1. Activation of n-Si/Ni

In alkaline photoelectrochemical conditions, the Ni film is known to experience an activation stage before it stabilizes.[82] This activation process can be triggered either by applying an anodic potential for some time or run multiple cyclic voltammetry cycles at operating potential range. Here, as an anodic potential of 2.0 V vs. RHE was applied (Figure 3-19), a gradual increase of photocurrent density was shown, with an initial value of ~23 mA cm^{-2} to a final value 23.5 mA cm^{-2} after 1 hour.

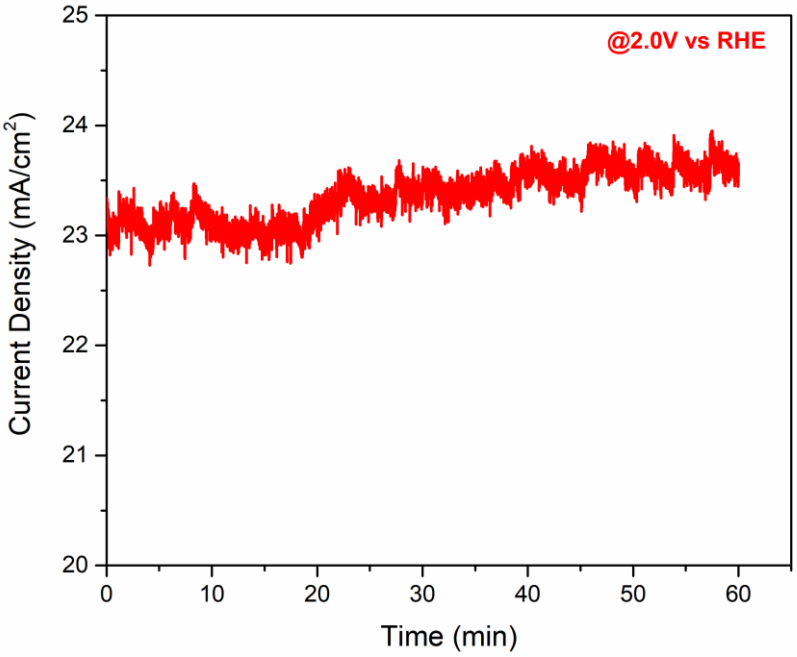

Figure 3-19. One-hour activation of Ni catalyst layer by applying a potential of 2.0 V vs. RHE in 1 M KOH. Simulated sunlight (AM 1.5, 100 mW/cm^2) was used.

It is more noticeable by comparing LSV curves of the freshly prepared sample against the activated sample. This observation agrees well with previous studies. [80-82]

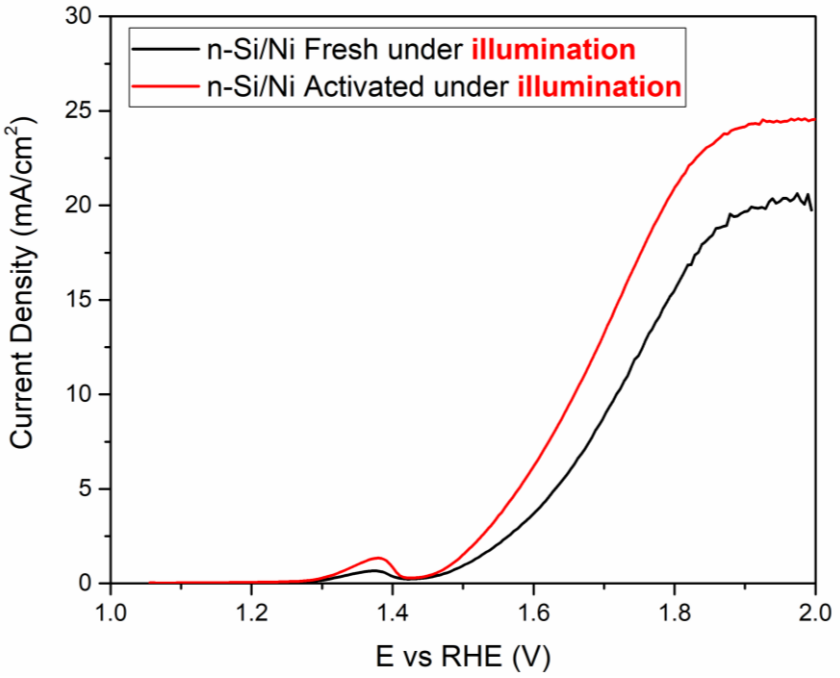

Figure 3-20. Linear sweep voltammograms of fresh n-Si/Ni sample (black) and activated n-Si-Ni sample (red). Simulated sunlight (AM 1.5, 100 mW/cm^2) was used.

3.2.2. Chemical State of Ni Catalyst Layer

This activation process is considered a result of the change in chemical state of nickel.[82] Previous studies showed that Ni film under alkaline (in our case, 1 M KOH, pH 14) and PEC operating conditions is known to transform into hydroxides (a combination of $Ni(OH)_2$ and γ-NiOOH, which are usually considered as the catalytically-active species of Ni-based compounds[105, 106]), where the sub-surface layer remains in metallic state.[80, 82] According to Oh et al., the $Ni(OH)_2$ is first formed by photo-oxidation of Ni metal before being photo-oxidized again to form the γ-NiOOH phase, which described as follows [82]:

$$Ni^{0}{}_{(s)} + 2OH^{-}{}_{(l)} + 2h^{+} \rightarrow Ni^{II}(OH)_{2(s)} \quad (3\text{-}2)$$

$$Ni^{II}(OH)_{2(s)} + OH^{-}{}_{(l)} + h^{+} \rightarrow Ni^{III}OOH_{(s)} + H_2O_{(l)} \quad (3\text{-}3)$$

To confirm this assumption, the n-Si/Ni photoanode after the activation step was taken out immediately and washed with DI water, and was analyzed by XPS for Ni2p spectrum. As shown in Figure 3-21, the maximum binding energy of Ni2p 3/2 is experimentally found to be 855.5 eV which agrees with that of $Ni(OH)_2$ (855.80 eV) and γ-NiOOH (855.75 eV), while Ni metal (852.54 eV) and NiO (853.78 eV) states do not appear on XPS results.[107] Unfortunately, the two hydroxide phases are indistinguishable in the XPS spectrum and usually co-exist under operating conditions.[82]

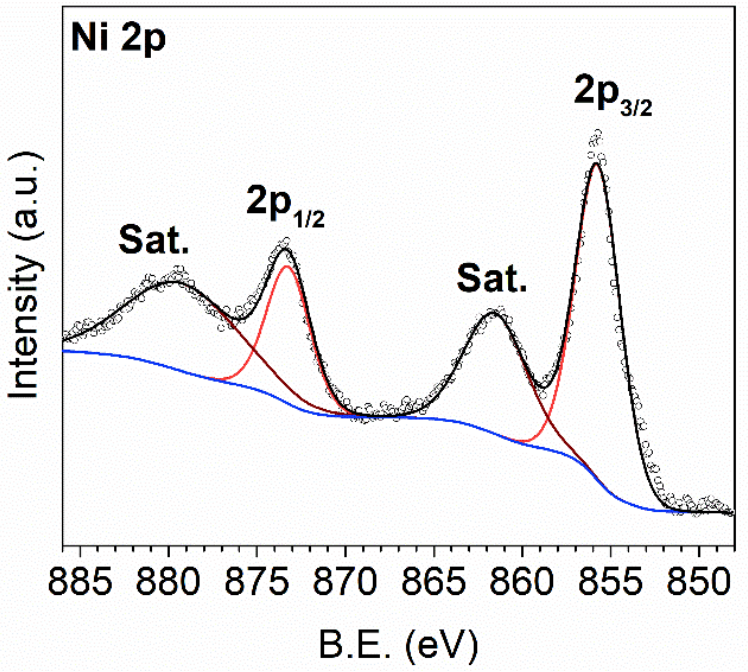

Figure 3-21. Ni2p XPS spectrum of the activated n-Si/Ni photoanode.

Figure 3-22 shows the schematic of the n-Si/Ni's final structure, where Ga/In eutectic alloy here serve as ohmic back contact.

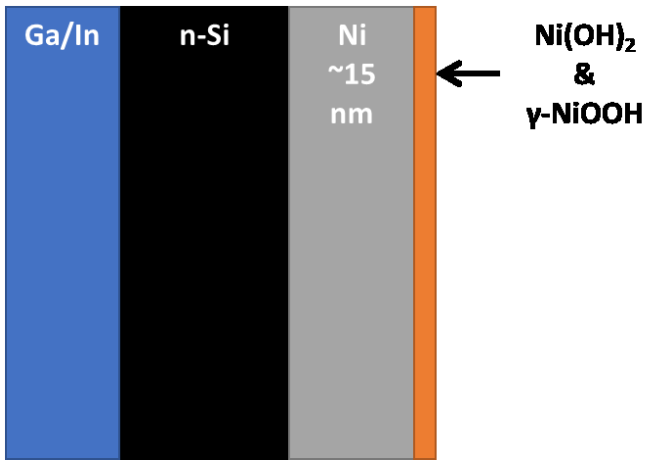

Figure 3-22. Structure schematic of n-Si/Ni photoanode with $Ni(OH)_2$ & γ-NiOOH active layer.

3.2.2. Performance of n-Si/Ni Photoanode

For benchmarking, a heavily-doped (degenerate) n-type silicon coated with same Ni catalyst layer (denoted as n++Si/Ni) was used. Here, the n++Si/Ni serves as a "dark" conductive electrode and is compared to the photo-active n-Si/Ni photoanode. As shown in Figure 3-23, the onset potential (at 1.0 mA cm^{-2}) of n-Si/Ni is 1.46 V compared to 1.57 V obtained using n++Si/Ni dark electrode, signifying 110 mV of photovoltage generated from n-Si/Ni. Regardless of this improvement, the n-Si/Ni cannot achieve photo-oxidation of water operated below its equilibrium potential (1.23 V vs. RHE) as shown in earlier works.[78, 80-82]

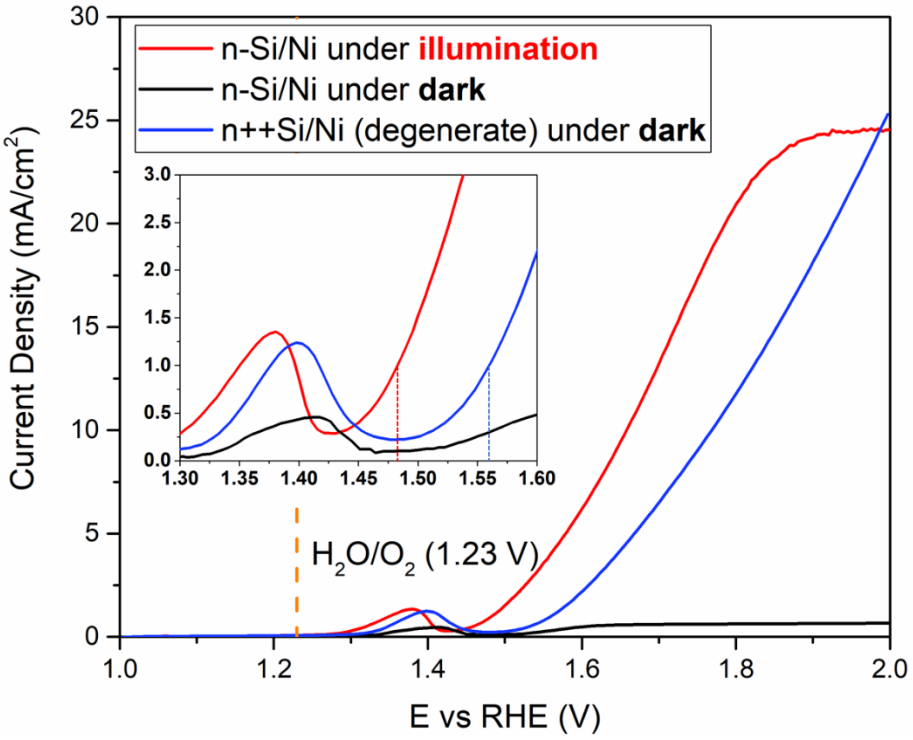

Figure 3-23. Linear sweep voltammograms of Ni-coated n-Si photoanode under illumination (red line) and dark (black line), and degenerately doped n++Si in the dark. The electrolyte is 1 M KOH.

3.2.2. Current Issues of the n-Si/Ni Photoanode and Potential Resolutions

By comparing with previous studies, it is suspected that the low photovoltage associated with the as-fabricated n-Si/Ni may have been caused primarily by the presence of excessive defect states acting as fast recombination centers.[79] In this work, there are couple of possibilities that may have created these defect states: (1) fast formation of SiO_x layer (source of defects) on Si between HF/BOE treatment and magnetron sputtering steps, (2) high-density interfacial defects on Si created by high kinetic energy bombardment of Ni atoms in the initial stage of sputtering deposition.[108, 109]

The formation of SiO_x can be alleviated in a fully automated production line where minimal oxygen and contaminations are present, as well as minimal wait time between

HF/BOE cleaning and deposition steps. Given the available facilities at disposal, this strategy cannot be achieved at this moment. The problems with excessive interfacial defect between Si and Ni was resolved in a recent work by Li et al.[79] The author utilized a rapid thermal process (RTP) oven to quickly anneal the as-prepared n-Si/Ni at 450 °C in a pure N_2 ambiance for 30 s. This step is to allow some diffusion of Ni atoms into the Si lattice, creating a much more robust interface with fewer defects. Li's results indicated a 150-mV reduction in onset potential following the RTP treatment. Unfortunately, an RTP oven is also not available at disposal, and hence full cell test was conducted as-is.

3.3. Photoanode-driven PEC CO_2 Reduction

To address the challenge of high overpotential associated with electrochemical CO_2RR, we further demonstrated a PEC system driven by the as-fabricated n-Si/Ni photoanode and the CuSn40 catalyst as a dark cathode. This PEC system is compared against an electrochemical system where a commercial OER catalyst, IrO_2, is used as a dark anode. Figure 3-24 shows the schematic illustration of the two-compartment PEC cell separated by a Nafion membrane, where simulated sunlight (1 sun, AM1.5, with an intensity of 100 mW cm^{-2}) was used to illuminate the photoanode.

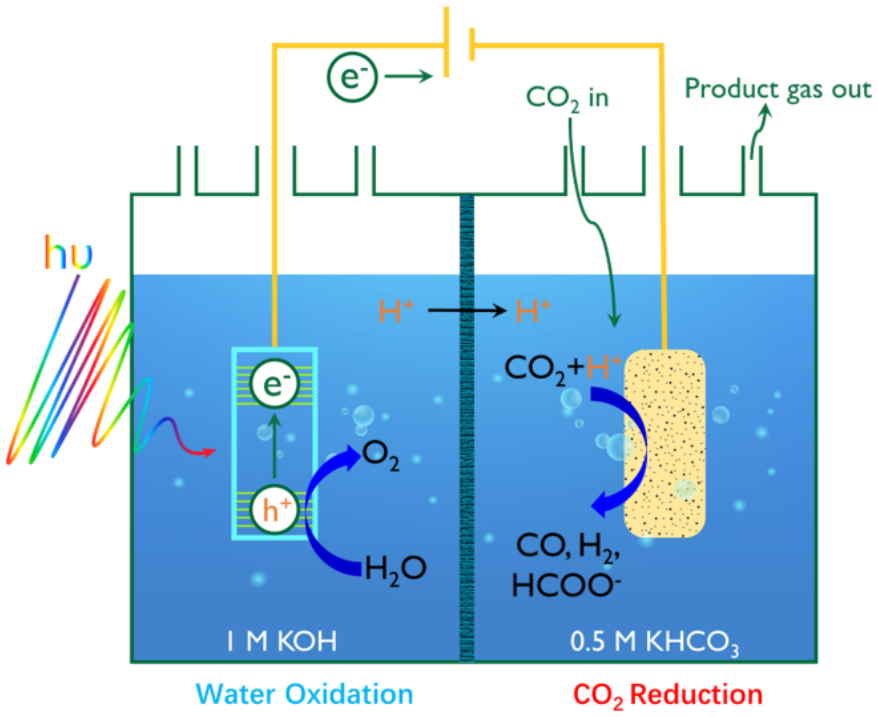

Figure 3-24. Schematic illustration of the two-compartment PEC cell driven by a photoanode.

3.3.1. PEC vs. EC System for CO_2 Reduction

Figure 3-25 shows the LSV curves of the photoanode-driven PEC systems (blue and black) as well as the electrochemical system (yellow). Under the experimental conditions, the PEC system performs much better than the EC systems. For example, at an applied cell voltage of 1.8 V, PEC delivers a current density of 3.3 mA cm^{-2}, whereas the EC system delivers only around 0.8 mA cm^{-2}, demonstrating a 4-fold improvement. Similarly, when evaluating the cell voltage to achieving a current density of 5 mA cm^{-2}, the PEC system can attain this value at 1.9 V whereas the EC system can attain it at 2.3 V, signifying 400 mV reduction in overpotential.

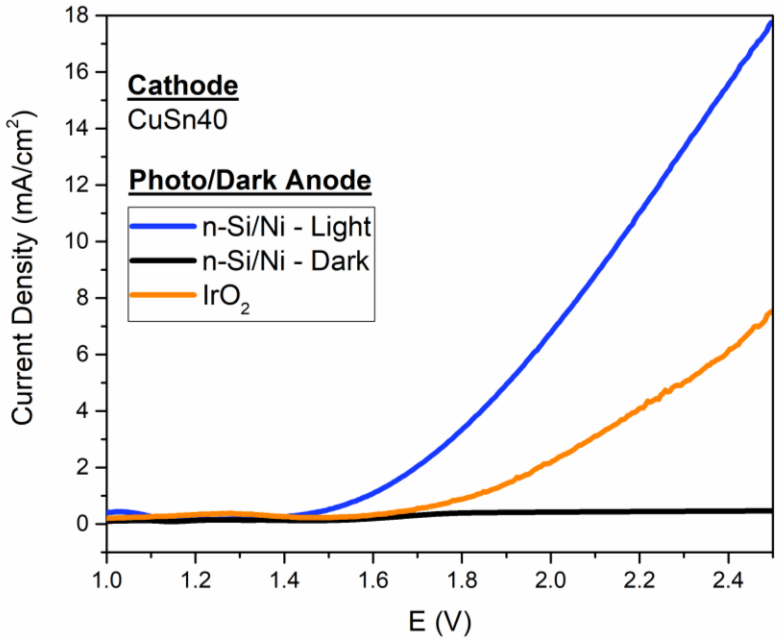

Figure 3-25. LSV of full cell driven by a n-Si/Ni photoanode (blue) and by a commercial IrO2 OER catalyst (yellow).

Figure 3-26 shows the chronoamperometry (CA) measurement of the PEC system at an applied cell voltage of 1.8 V. An evident photocurrent of ~2 mA cm^{-2} was observed upon illumination and disappeared once the light is cut-off.

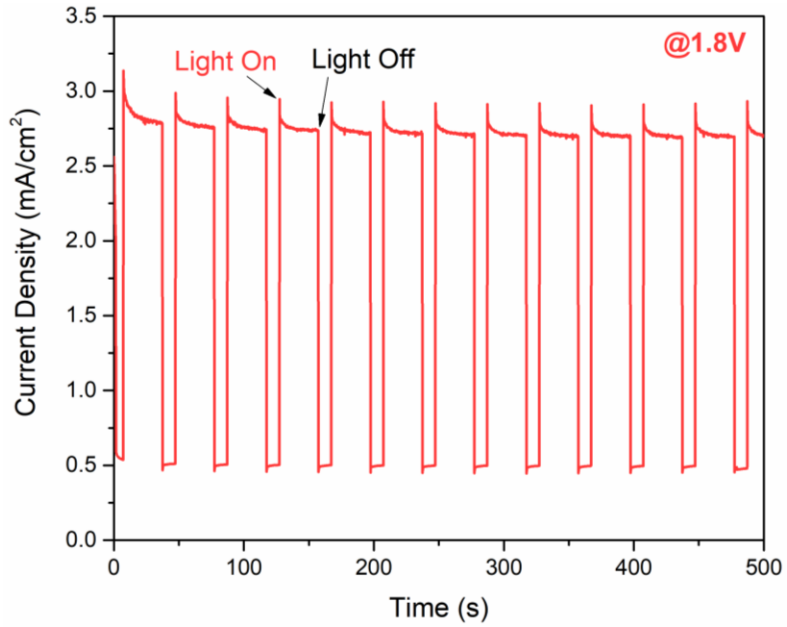

Figure 3-26. Chopped light (30 s/10 s on/off) CA measurement with at cell voltage of 1.8 V.

3.3.1. Stability and System Efficiency

The stability of the PEC cell at 1.8 V was then evaluated for 12 hours as shown in Figure 3-27. A slight degradation in current density and FE_{CO} was observed, which can be attributed to the degradation of the dark cathode (CuSn40, see Figure 3-16). The FE_{CO} and FE_{H2} remained stable with an average of 89.6% ± 2.0% and of 8.7% ± 1.2%, respectively, during the first three hours. Then, FE_{CO} and FE_{H2} were measured to be 82.1% ± 2.2% and 12.7% ± 2.1% in the final hours, respectively. The liquid product was quantified to be 4% formate using NMR spectroscopy. The reduced CO_2RR and increased HER during stability test is consistent with the electrochemical CO_2RR measurements on CuSn40 (Figure 3-16).

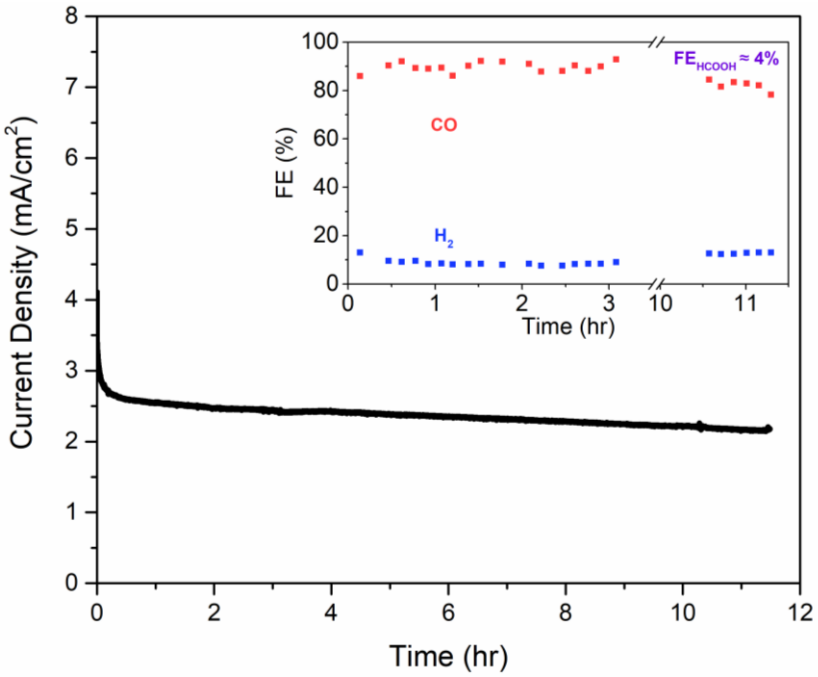

Figure 3-27. Long-term stability of the PEC system at a cell voltage of 1.8 V for 12 hours. Simulated sunlight (one sun, AM1.5, 100 mW cm^{-2}) is used to perform all PEC tests.

Because the cell still requires external bias to operate, the total energy input to the system is a combination of solar and electrical energy. Therefore, photo-assisted efficiency (η_{PAE}) is calculated to evaluate the performance of the designed system. Considering the

equilibrium potential of 1.34 V (1.23 V + 0.11 V) for CO_2-to-CO conversion and operating cell voltage of 1.8 V at ~85% FE_{CO}, the as-designed photoanode-driven system can achieve an η_{PAE} of 3.5%. Although this provides an idea of the system efficiency, η_{PAE} cannot be directly compared to solar-to-fuel efficiency, where zero net bias is applied.

Chapter 4 Conclusions and Future Work

4.1. Conclusions

In this thesis, the two proposed objectives were successfully achieved, including: (1) developing an economical and straightforward method to fabricate a non-precious metal-based electrocatalyst achieving high CO_2-to-CO conversion, and (2) developing a photoanode-driven PEC system in a full cell setup to achieve superior performance comparing to an EC system.

To achieve the first objective, a novel low-cost method using earth-abundant materials for synthesizing Cu_2O-SnO_2 core-shell nanocrystal catalyst have been reported. The synthesis method can be achieved at room-temperature while being surfactant/capping agent free, which can enable a scalable process for fabricating an efficient CO_2-to-CO electrocatalyst. This work provides a widely applicable strategy for developing a low-cost electrocatalyst for CO_2 conversion, and has been published at *ChemCatChem* (DOI: 10.1002/cctc.201900395), titled "A Rational Design of Cu_2O-SnO_2 Core-Shell Catalyst for Highly Selective CO_2-to-CO Conversion".

- The reported Cu_2O-SnO_2 catalyst demonstrated comparable, if not better, selectivity, activity, and stability compared to previously reported Cu-Sn based catalyst.
- The improved performance can be elucidated by the synergetic interaction between Cu and Sn atoms at the active sites, where the Cu to Sn ratio can be tuned by changing their respective precursor amount.
- A FE_{CO} of 90% and higher were achieved at overpotentials of 890 mV and 390 mV in 0.1 M $KHCO_3$ and 0.5 M $KHCO_3$, respectively.

- A stability test of 18 hours showed a slight degradation (less than 2.5%/hour decrease) in current density and CO_2RR Faradaic efficiency.

To achieve the second objective, n-Si/Ni photoanode was first fabricated by depositing ~15 nm of Ni protective and catalyst layer using DC magnetron sputtering technique and subsequently activated in PEC operating conditions. Followed by this, a photoanode-driven PEC system is demonstrated by combining Cu_2O-SnO_2 electrocatalyst as a dark cathode and the activated n-Si/Ni as photoanode.

- A 400-mV reduction in overpotential is achieved at 5 mA cm^{-2} when compared to an electrochemical system (with a commercial IrO_2/C as a dark anode).
- The PEC system showed a moderately stable operation for 12 hours at 1.8 V cell potential. The slight degradation is believed to have resulted from the cathode side.
- A photo-assisted efficiency (η_{PAE}) of 3.5% is achieved.

4.2. Recommendations for Future Work

4.2.1. Improving Activity of Cu_2O-SnO_2 Electrocatalyst

Despite the superior performance of Cu_2O-SnO_2 core-shell electrocatalyst, the current density (catalytic activity) at operating conditions is still very low (<10 mA cm^{-2}). To improve this, it is suggested to synthesize Cu_2O-SnO_2 catalyst with hierarchical structures for increased surface area, thereby improving its catalytic activity.

4.2.2. Benchmarking using Au catalyst

As mentioned in Chapter 1, precious metals, particularly gold (Au), is the most active material for CO_2 conversion to CO. Therefore, future work should utilize Au for benchmark comparison.

4.2.3. Overcoming Mass Transport Limitations of CO_2RR Electrolyser

The maximum current densities achieved in a conventional H-type CO_2RR electrolyzer (used in this work) is far inferior comparing to those reported for water electrolysis research (>300 mA cm^{-2}).[8] This is because the free CO_2 reactants reaching the catalyst surface exist primarily as a dissolved form in aqueous electrolyte, and requires rigorous stirring of electrolyte to facilitate the mass transport. Martin et al. suggested that the concentration of CO_2 at equilibrium is as low as 30 mM at 1 bar and 25 °C (about 33 mM in 0.1 M $KHCO_3$), which limits the attainable current density to approximately 60 mA cm^{-2}.[8] In fact, mass transport and CO_2 solubility can be improved simply by increasing pressure and using non-aqueous electrolyte with high CO_2 solubility, respectively. However, this would take away the advantages of ambient operating conditions and the

easily recyclable aqueous electrolyte. Alternatively, the following strategy can be implemented:

- Utilize a flow cell configuration where electrocatalysts are supported on a porous gas diffusion electrode (GDE). Gaseous CO_2 is fed from the backside of the porous electrode onto the catalyst surface directly, without being first dissolved in the electrolyte. This creates a triple phase boundary where CO_2, electrons, and water would meet.[8] As such, the system is no longer limited by the low solubility of CO_2, but rather the diffusion rate of CO_2 to the catalyst surface.

4.2.3. Enhancing the Performance of the n-Si/Ni Photoanode

The following work can be conducted to enhance the performance of n-Si/Ni photoanode:

- Optimize the thickness of Ni film to allow higher light transmittance while preserving adequate protection of Si photoanode.
- Reduce the formation of SiO_x by processing the Silicon wafer in an automated fabrication line where minimal oxygen and contamination is present.
- Use rapid thermal processing (RTP) method to reduce Ni/Si interface defects.
- Enhance photovoltage by introducing p+ emitter layer to create buried p-n junction.
- Decorate Ni catalyst with additional OER co-catalyst such as Fe and Co to improve catalytic performance

4.2.4. Achieving Unassisted Photoelectrochemical Reduction of CO_2

The photoanode-driven PEC system presented in this thesis still operates above the equilibrium potential, where energy-to-fuel conversion mostly depends on electrical input.

To achieve the goal of unassisted PEC CO_2-to-CO conversion, the following recommendations are proposed:

- Design a photoanode that can provide enough photovoltage (1.34 V + cathodic overpotential) to drive the full PEC cell. To the best of my knowledge, no work has been reported for unassisted photoanode-driven PEC CO_2 reduction.
- Design a tandem PEC cell which combines both photoanode and photocathode to achieve unassisted operation.

Bibliography

[1] A. Rafiee, K. R. Khalilpour, D. Milani, and M. Panahi, "Trends in CO2 conversion and utilization: A review from process systems perspective," *Journal of environmental chemical engineering,* 2018.

[2] C. Le Quéré *et al.*, "Global Carbon Budget 2018," *Earth System Science Data,* vol. 10, no. 4, pp. 2141-2194, 2018.

[3] S. Chu and A. Majumdar, "Opportunities and challenges for a sustainable energy future," *nature,* vol. 488, no. 7411, p. 294, 2012.

[4] D. S. Simakov, *Renewable Synthetic Fuels and Chemicals from Carbon Dioxide: Fundamentals, Catalysis, Design Considerations and Technological Challenges*. Springer, 2017.

[5] M. Aresta, A. Dibenedetto, and A. Angelini, "Catalysis for the valorization of exhaust carbon: from CO2 to chemicals, materials, and fuels. technological use of CO2," *Chem Rev,* vol. 114, no. 3, pp. 1709-42, Feb 12 2014.

[6] F. Karimi and R. Khalilpour, "Evolution of carbon capture and storage research: Trends of international collaborations and knowledge maps," *International Journal of Greenhouse Gas Control,* vol. 37, pp. 362-376, 2015.

[7] N. Muradov, "Industrial Utilization of CO 2: A Win–Win Solution," in *Liberating Energy from Carbon: Introduction to Decarbonization*: Springer, 2014, pp. 325-383.

[8] A. J. Martín, G. O. Larrazábal, and J. Pérez-Ramírez, "Towards sustainable fuels and chemicals through the electrochemical reduction of CO 2: lessons from water electrolysis," *Green Chemistry,* vol. 17, no. 12, pp. 5114-5130, 2015.

[9] J. L. White *et al.*, "Light-Driven Heterogeneous Reduction of Carbon Dioxide: Photocatalysts and Photoelectrodes," *Chem Rev,* vol. 115, no. 23, pp. 12888-935, Dec 09 2015.

[10] F. Fischer and H. Tropsch, "The preparation of synthetic oil mixtures (synthol) from carbon monoxide and hydrogen," *Brennstoff-Chem,* vol. 4, pp. 276-285, 1923.

[11] D. D. Zhu, J. L. Liu, and S. Z. Qiao, "Recent advances in inorganic heterogeneous electrocatalysts for reduction of carbon dioxide," *Advanced materials,* vol. 28, no. 18, pp. 3423-3452, 2016.

[12] P. Wang, S. Wang, H. Wang, Z. Wu, and L. Wang, "Recent Progress on Photo-Electrocatalytic Reduction of Carbon Dioxide," *Particle & Particle Systems Characterization,* vol. 35, no. 1, p. 1700371, 2018.

[13] W. M. Haynes, *CRC handbook of chemistry and physics*. CRC press, 2014.

[14] P. S. Surdhar, S. P. Mezyk, and D. A. Armstrong, "Reduction potential of the carboxyl radical anion in aqueous solutions," *The Journal of Physical Chemistry,* vol. 93, no. 8, pp. 3360-3363, 1989.

[15] C. Costentin, M. Robert, and J.-M. Savéant, "Catalysis of the electrochemical reduction of carbon dioxide," *Chemical Society Reviews,* vol. 42, no. 6, pp. 2423-2436, 2013.

[16] E. E. Benson, C. P. Kubiak, A. J. Sathrum, and J. M. Smieja, "Electrocatalytic and homogeneous approaches to conversion of CO 2 to liquid fuels," *Chemical Society Reviews,* vol. 38, no. 1, pp. 89-99, 2009.

[17] J. Schneider, H. Jia, J. T. Muckerman, and E. Fujita, "Thermodynamics and kinetics of CO2, CO, and H+ binding to the metal centre of CO2 reduction catalysts," *Chemical Society Reviews,* vol. 41, no. 6, pp. 2036-2051, 2012.
[18] J. P. Jones, G. S. Prakash, and G. A. Olah, "Electrochemical CO2 reduction: recent advances and current trends," *Israel Journal of Chemistry,* vol. 54, no. 10, pp. 1451-1466, 2014.
[19] R. Schlögl, "Heterogeneous catalysis," *Angewandte Chemie International Edition,* vol. 54, no. 11, pp. 3465-3520, 2015.
[20] Y. Hori, H. Wakebe, T. Tsukamoto, and O. Koga, "Electrocatalytic process of CO selectivity in electrochemical reduction of CO2 at metal electrodes in aqueous media," *Electrochimica Acta,* vol. 39, no. 11-12, pp. 1833-1839, 1994.
[21] J. T. Feaster *et al.*, "Understanding selectivity for the electrochemical reduction of carbon dioxide to formic acid and carbon monoxide on metal electrodes," *Acs Catalysis,* vol. 7, no. 7, pp. 4822-4827, 2017.
[22] Y. i. Hori, "Electrochemical CO 2 reduction on metal electrodes," in *Modern aspects of electrochemistry*: Springer, 2008, pp. 89-189.
[23] D. Gao *et al.*, "Size-dependent electrocatalytic reduction of CO2 over Pd nanoparticles," *Journal of the American Chemical Society,* vol. 137, no. 13, pp. 4288-4291, 2015.
[24] S. Liu *et al.*, "Ultrathin 5-fold twinned sub-25 nm silver nanowires enable highly selective electroreduction of CO2 to CO," *Nano Energy,* vol. 45, pp. 456-462, 2018.
[25] Q. Lu *et al.*, "A selective and efficient electrocatalyst for carbon dioxide reduction," *Nature communications,* vol. 5, p. 3242, 2014.
[26] S. Liu *et al.*, "Shape-dependent electrocatalytic reduction of CO2 to CO on triangular silver nanoplates," *Journal of the American Chemical Society,* vol. 139, no. 6, pp. 2160-2163, 2017.
[27] W. Zhu *et al.*, "Monodisperse Au nanoparticles for selective electrocatalytic reduction of CO2 to CO," *Journal of the American Chemical Society,* vol. 135, no. 45, pp. 16833-16836, 2013.
[28] P. Su, W. Xu, Y. Qiu, T. Zhang, X. Li, and H. Zhang, "Ultrathin Bismuth Nanosheets as a Highly Efficient CO2 Reduction Electrocatalyst," *ChemSusChem,* vol. 11, no. 5, pp. 848-853, 2018.
[29] J. J. Humphrey *et al.*, "Electrochemical reduction of carbon dioxide at gold - palladium core–shell nanoparticles: product distribution versus shell thickness," *ChemCatChem,* vol. 8, no. 5, pp. 952-960, 2016.
[30] X. Feng, K. Jiang, S. Fan, and M. W. Kanan, "Grain-boundary-dependent CO2 electroreduction activity," *Journal of the American Chemical Society,* vol. 137, no. 14, pp. 4606-4609, 2015.
[31] Y. Chen, C. W. Li, and M. W. Kanan, "Aqueous CO2 reduction at very low overpotential on oxide-derived Au nanoparticles," *Journal of the American Chemical Society,* vol. 134, no. 49, pp. 19969-19972, 2012.
[32] M. Yang *et al.*, "Facet Sensitivity of Capping Ligand - Free Ag Crystals in CO2 Electrochemical Reduction to CO," *ChemCatChem,* vol. 10, no. 22, pp. 5128-5134, 2018.

[33] J. Rosen *et al.*, "Mechanistic insights into the electrochemical reduction of CO2 to CO on nanostructured Ag surfaces," *Acs Catalysis,* vol. 5, no. 7, pp. 4293-4299, 2015.
[34] C. W. Lee *et al.*, "Selective electrochemical production of formate from carbon dioxide with bismuth-based catalysts in an aqueous electrolyte," *ACS Catalysis,* vol. 8, no. 2, pp. 931-937, 2018.
[35] J. H. Koh *et al.*, "Facile CO2 electro-reduction to formate via oxygen bidentate intermediate stabilized by high-index planes of Bi dendrite catalyst," *ACS Catalysis,* vol. 7, no. 8, pp. 5071-5077, 2017.
[36] Y. Li, F. Cui, M. B. Ross, D. Kim, Y. Sun, and P. Yang, "Structure-sensitive CO2 electroreduction to hydrocarbons on ultrathin 5-fold twinned copper nanowires," *Nano letters,* vol. 17, no. 2, pp. 1312-1317, 2017.
[37] C. W. Li and M. W. Kanan, "CO2 reduction at low overpotential on Cu electrodes resulting from the reduction of thick Cu2O films," *Journal of the American Chemical Society,* vol. 134, no. 17, pp. 7231-7234, 2012.
[38] D. Raciti, K. J. Livi, and C. Wang, "Highly dense Cu nanowires for low-overpotential CO2 reduction," *Nano letters,* vol. 15, no. 10, pp. 6829-6835, 2015.
[39] R. Kas, R. Kortlever, A. Milbrat, M. T. Koper, G. Mul, and J. Baltrusaitis, "Electrochemical CO 2 reduction on Cu 2 O-derived copper nanoparticles: controlling the catalytic selectivity of hydrocarbons," *Physical Chemistry Chemical Physics,* vol. 16, no. 24, pp. 12194-12201, 2014.
[40] S. Sen, D. Liu, and G. T. R. Palmore, "Electrochemical reduction of CO2 at copper nanofoams," *Acs Catalysis,* vol. 4, no. 9, pp. 3091-3095, 2014.
[41] Y. Lum and J. W. Ager, "Evidence for product-specific active sites on oxide-derived Cu catalysts for electrochemical CO 2 reduction," *Nature Catalysis,* vol. 2, no. 1, p. 86, 2019.
[42] A. Eilert *et al.*, "Subsurface oxygen in oxide-derived copper electrocatalysts for carbon dioxide reduction," *The journal of physical chemistry letters,* vol. 8, no. 1, pp. 285-290, 2016.
[43] M. Ma, B. J. Trześniewski, J. Xie, and W. A. Smith, "Selective and Efficient Reduction of Carbon Dioxide to Carbon Monoxide on Oxide - Derived Nanostructured Silver Electrocatalysts," *Angewandte Chemie International Edition,* vol. 55, no. 33, pp. 9748-9752, 2016.
[44] B. Kumar *et al.*, "Reduced SnO2 Porous Nanowires with a High Density of Grain Boundaries as Catalysts for Efficient Electrochemical CO2 - into - HCOOH Conversion," *Angewandte Chemie International Edition,* vol. 56, no. 13, pp. 3645-3649, 2017.
[45] F. Li, L. Chen, G. P. Knowles, D. R. MacFarlane, and J. Zhang, "Hierarchical mesoporous SnO2 nanosheets on carbon cloth: a robust and flexible electrocatalyst for CO2 reduction with high efficiency and selectivity," *Angewandte Chemie International Edition,* vol. 56, no. 2, pp. 505-509, 2017.
[46] D. H. Won, C. H. Choi, J. Chung, M. W. Chung, E. H. Kim, and S. I. Woo, "Rational design of a hierarchical tin dendrite electrode for efficient electrochemical reduction of CO2," *ChemSusChem,* vol. 8, no. 18, pp. 3092-3098, 2015.

[47] S. O. Kasap, *Principles of electronic materials and devices*. McGraw-Hill New York, 2006.
[48] A. J. Bard and L. R. Faulkner, "Fundamentals and applications," *Electrochemical Methods,* vol. 2, p. 482, 2001.
[49] P. Kissinger and W. R. Heineman, *Laboratory Techniques in Electroanalytical Chemistry, revised and expanded*. CRC press, 1996.
[50] A. Fujishima and K. Honda, "Electrochemical photolysis of water at a semiconductor electrode," *nature,* vol. 238, no. 5358, p. 37, 1972.
[51] L. Peter, J. Li, and R. Peat, "Surface recombination at semiconductor electrodes: Part I. Transient and steady-state photocurrents," *Journal of electroanalytical chemistry and interfacial electrochemistry,* vol. 165, no. 1-2, pp. 29-40, 1984.
[52] J. Kelly and R. Memming, "The Influence of Surface Recombination and Trapping on the Cathodic Photocurrent at p - Type III - V Electrodes," *Journal of the Electrochemical Society,* vol. 129, no. 4, pp. 730-738, 1982.
[53] X. Chang, T. Wang, P. Yang, G. Zhang, and J. Gong, "The Development of Cocatalysts for Photoelectrochemical CO2 Reduction," *Advanced Materials,* p. 1804710, 2018.
[54] W. Tu, Y. Zhou, and Z. Zou, "Photocatalytic conversion of CO2 into renewable hydrocarbon fuels: state-of-the-art accomplishment, challenges, and prospects," *Advanced Materials,* vol. 26, no. 27, pp. 4607-4626, 2014.
[55] Z. Chen, H. N. Dinh, and E. Miller, *Photoelectrochemical water splitting*. Springer, 2013.
[56] R. H. Coridan *et al.*, "Methods for comparing the performance of energy-conversion systems for use in solar fuels and solar electricity generation," *Energy & Environmental Science,* vol. 8, no. 10, pp. 2886-2901, 2015.
[57] C. Lokhande and S. Pawar, "Electrochemical photovoltaic cells for solar energy conversion," *Materials chemistry and physics,* vol. 11, no. 3, pp. 201-277, 1984.
[58] M. Schreier, J. Luo, P. Gao, T. Moehl, M. T. Mayer, and M. Gratzel, "Covalent Immobilization of a Molecular Catalyst on Cu2O Photocathodes for CO2 Reduction," *J Am Chem Soc,* vol. 138, no. 6, pp. 1938-46, Feb 17 2016.
[59] X. Chang, T. Wang, P. Zhang, Y. Wei, J. Zhao, and J. Gong, "Stable Aqueous Photoelectrochemical CO2 Reduction by a Cu2 O Dark Cathode with Improved Selectivity for Carbonaceous Products," *Angew Chem Int Ed Engl,* vol. 55, no. 31, pp. 8840-5, Jul 25 2016.
[60] X. Ba, L.-L. Yan, S. Huang, J. Yu, X.-J. Xia, and Y. Yu, "New Way for CO2 Reduction under Visible Light by a Combination of a Cu Electrode and Semiconductor Thin Film: Cu2O Conduction Type and Morphology Effect," *The Journal of Physical Chemistry C,* vol. 118, no. 42, pp. 24467-24478, 2014.
[61] S. Ikeda, M. Yoshida, and K. Ito, "Photoelectrochemical reduction products of carbon dioxide at metal coated p-GaP photocathodes in aqueous electrolytes," *Bulletin of the Chemical Society of Japan,* vol. 58, no. 5, pp. 1353-1357, 1985.
[62] G. Zeng, J. Qiu, Z. Li, P. Pavaskar, and S. B. Cronin, "CO2 reduction to methanol on TiO2-passivated GaP photocatalysts," *ACS Catalysis,* vol. 4, no. 10, pp. 3512-3516, 2014.
[63] J.-P. Petit, P. Chartier, M. Beley, and J.-P. Deville, "Molecular catalysts in photoelectrochemical cells: study of an efficient system for the selective

photoelectroreduction of CO2: p-GaP or p-GaAs/Ni (cyclam) 2+, aqueous medium," *Journal of Electroanalytical Chemistry and Interfacial Electrochemistry,* vol. 269, no. 2, pp. 267-281, 1989.

[64] E. E. Barton, D. M. Rampulla, and A. B. Bocarsly, "Selective solar-driven reduction of CO2 to methanol using a catalyzed p-GaP based photoelectrochemical cell," *Journal of the American Chemical Society,* vol. 130, no. 20, pp. 6342-6344, 2008.

[65] K. Hirota, D. A. Tryk, K. Hashimoto, M. Okawa, and A. Fujishima, "Photoelectrochemical Reduction of CO 2 at High Current Densities at p - InP Electrodes," *Journal of the Electrochemical Society,* vol. 145, no. 5, pp. L82-L84, 1998.

[66] T. Arai, S. Sato, K. Uemura, T. Morikawa, T. Kajino, and T. Motohiro, "Photoelectrochemical reduction of CO 2 in water under visible-light irradiation by a p-type InP photocathode modified with an electropolymerized ruthenium complex," *Chemical Communications,* vol. 46, no. 37, pp. 6944-6946, 2010.

[67] S. Kaneco, Y. Ueno, H. Katsumata, T. Suzuki, and K. Ohta, "Photoelectrochemical reduction of CO2 at p-InP electrode in copper particle-suspended methanol," *Chemical Engineering Journal,* vol. 148, no. 1, pp. 57-62, 2009.

[68] T. P. Senftle, M. Lessio, and E. A. Carter, "Interaction of pyridine and water with the reconstructed surfaces of GaP (111) and CdTe (111) photoelectrodes: implications for CO2 reduction," *Chemistry of Materials,* vol. 28, no. 16, pp. 5799-5810, 2016.

[69] H. Yoneyama, K. Sugimura, and S. Kuwabata, "Effects of electrolytes on the photoelectrochemical reduction of carbon dioxide at illuminated p-type cadmium telluride and p-type indium phosphide electrodes in aqueous solutions," *Journal of electroanalytical chemistry and interfacial electrochemistry,* vol. 249, no. 1-2, pp. 143-153, 1988.

[70] Q. Kong *et al.*, "Directed Assembly of Nanoparticle Catalysts on Nanowire Photoelectrodes for Photoelectrochemical CO2 Reduction," *Nano Lett,* vol. 16, no. 9, pp. 5675-80, Sep 14 2016.

[71] S. Chu *et al.*, "Photoelectrochemical CO2 Reduction into Syngas with the Metal/Oxide Interface," *J Am Chem Soc,* vol. 140, no. 25, pp. 7869-7877, Jun 27 2018.

[72] S. Chu *et al.*, "Tunable Syngas Production from CO2 and H2 O in an Aqueous Photoelectrochemical Cell," *Angew Chem Int Ed Engl,* vol. 55, no. 46, pp. 14262-14266, Nov 7 2016.

[73] R. Hinogami, Y. Nakamura, S. Yae, and Y. Nakato, "An Approach to Ideal Semiconductor Electrodes for Efficient Photoelectrochemical Reduction of Carbon Dioxide by Modification with Small Metal Particles," *The Journal of Physical Chemistry B,* vol. 102, no. 6, pp. 974-980, 1998.

[74] S. K. Choi, U. Kang, S. Lee, D. J. Ham, S. M. Ji, and H. Park, "Sn-Coupled p-Si Nanowire Arrays for Solar Formate Production from CO2," *Advanced Energy Materials,* vol. 4, no. 11, 2014.

[75] J. T. Song *et al.*, "Nanoporous Au Thin Films on Si Photoelectrodes for Selective and Efficient Photoelectrochemical CO2Reduction," *Advanced Energy Materials,* vol. 7, no. 3, 2017.

[76] K. R. Rao *et al.*, "Photoelectrochemical reduction of CO2 to HCOOH on silicon photocathodes with reduced SnO2 porous nanowire catalysts," *Journal of Materials Chemistry A,* vol. 6, no. 4, pp. 1736-1742, 2018.
[77] D. Kang, T. W. Kim, S. R. Kubota, A. C. Cardiel, H. G. Cha, and K.-S. Choi, "Electrochemical synthesis of photoelectrodes and catalysts for use in solar water splitting," *Chemical reviews,* vol. 115, no. 23, pp. 12839-12887, 2015.
[78] L. He, W. Zhou, D. Cai, S. S. Mao, K. Sun, and S. Shen, "Pulsed laser-deposited n-Si/NiO x photoanodes for stable and efficient photoelectrochemical water splitting," *Catalysis Science & Technology,* vol. 7, no. 12, pp. 2632-2638, 2017.
[79] S. Li *et al.*, "Enhancing the Photovoltage of Ni/n-Si Photoanode for Water Oxidation through a Rapid Thermal Process," *ACS applied materials & interfaces,* vol. 10, no. 10, pp. 8594-8598, 2018.
[80] M. J. Kenney *et al.*, "High-performance silicon photoanodes passivated with ultrathin nickel films for water oxidation," *Science,* vol. 342, no. 6160, pp. 836-840, 2013.
[81] K. Sun *et al.*, "Stable solar-driven water oxidation to O2 (g) by Ni-oxide-coated silicon photoanodes," *The journal of physical chemistry letters,* vol. 6, no. 4, pp. 592-598, 2015.
[82] K. Oh *et al.*, "Elucidating the performance and unexpected stability of partially coated water-splitting silicon photoanodes," *Energy & Environmental Science,* vol. 11, no. 9, pp. 2590-2599, 2018.
[83] W. J. Jo *et al.*, "Phosphate doping into monoclinic BiVO4 for enhanced photoelectrochemical water oxidation activity," *Angewandte Chemie International Edition,* vol. 51, no. 13, pp. 3147-3151, 2012.
[84] Y. H. Ng, A. Iwase, A. Kudo, and R. Amal, "Reducing graphene oxide on a visible-light BiVO4 photocatalyst for an enhanced photoelectrochemical water splitting," *The Journal of Physical Chemistry Letters,* vol. 1, no. 17, pp. 2607-2612, 2010.
[85] S. J. Hong, S. Lee, J. S. Jang, and J. S. Lee, "Heterojunction BiVO 4/WO 3 electrodes for enhanced photoactivity of water oxidation," *Energy & Environmental Science,* vol. 4, no. 5, pp. 1781-1787, 2011.
[86] J. Su, L. Guo, N. Bao, and C. A. Grimes, "Nanostructured WO3/BiVO4 heterojunction films for efficient photoelectrochemical water splitting," *Nano letters,* vol. 11, no. 5, pp. 1928-1933, 2011.
[87] T. W. Kim and K.-S. Choi, "Nanoporous BiVO4 photoanodes with dual-layer oxygen evolution catalysts for solar water splitting," *Science,* vol. 343, no. 6174, pp. 990-994, 2014.
[88] V. Cristino, S. Caramori, R. Argazzi, L. Meda, G. L. Marra, and C. A. Bignozzi, "Efficient photoelectrochemical water splitting by anodically grown WO3 electrodes," *Langmuir,* vol. 27, no. 11, pp. 7276-7284, 2011.
[89] K. Sivula, F. L. Formal, and M. Gratzel, "WO3− Fe2O3 photoanodes for water splitting: A host scaffold, guest absorber approach," *Chemistry of Materials,* vol. 21, no. 13, pp. 2862-2867, 2009.
[90] A. Wolcott, W. A. Smith, T. R. Kuykendall, Y. Zhao, and J. Z. Zhang, "Photoelectrochemical water splitting using dense and aligned TiO2 nanorod arrays," *Small,* vol. 5, no. 1, pp. 104-111, 2009.

[91] G. Wang *et al.*, "Hydrogen-treated TiO2 nanowire arrays for photoelectrochemical water splitting," *Nano letters,* vol. 11, no. 7, pp. 3026-3033, 2011.
[92] Y.-C. Pu *et al.*, "Au nanostructure-decorated TiO2 nanowires exhibiting photoactivity across entire UV-visible region for photoelectrochemical water splitting," *Nano letters,* vol. 13, no. 8, pp. 3817-3823, 2013.
[93] S. Xie, Q. Zhang, G. Liu, and Y. Wang, "Photocatalytic and photoelectrocatalytic reduction of CO 2 using heterogeneous catalysts with controlled nanostructures," *Chemical communications,* vol. 52, no. 1, pp. 35-59, 2016.
[94] S. Sarfraz, A. T. Garcia-Esparza, A. Jedidi, L. Cavallo, and K. Takanabe, "Cu–Sn bimetallic catalyst for selective aqueous electroreduction of CO2 to CO," *ACS Catalysis,* vol. 6, no. 5, pp. 2842-2851, 2016.
[95] Y. Zhao, C. Wang, and G. G. Wallace, "Tin nanoparticles decorated copper oxide nanowires for selective electrochemical reduction of aqueous CO2 to CO," *Journal of Materials Chemistry A,* vol. 4, no. 27, pp. 10710-10718, 2016.
[96] Q. Li *et al.*, "Tuning Sn-Catalysis for Electrochemical Reduction of CO2 to CO via the Core/Shell Cu/SnO2 Structure," *J Am Chem Soc,* vol. 139, no. 12, pp. 4290-4293, Mar 29 2017.
[97] M. Schreier *et al.*, "Solar conversion of CO2 to CO using Earth-abundant electrocatalysts prepared by atomic layer modification of CuO," *Nature Energy,* vol. 2, no. 7, 2017.
[98] K. Sun, S. Shen, Y. Liang, P. E. Burrows, S. S. Mao, and D. Wang, "Enabling silicon for solar-fuel production," *Chemical reviews,* vol. 114, no. 17, pp. 8662-8719, 2014.
[99] S. Hu, M. R. Shaner, J. A. Beardslee, M. Lichterman, B. S. Brunschwig, and N. S. Lewis, "Amorphous TiO2 coatings stabilize Si, GaAs, and GaP photoanodes for efficient water oxidation," *Science,* vol. 344, no. 6187, pp. 1005-1009, 2014.
[100] Y. Yu *et al.*, "Enhanced photoelectrochemical efficiency and stability using a conformal TiO 2 film on a black silicon photoanode," *Nature Energy,* vol. 2, no. 6, p. 17045, 2017.
[101] D.-F. Zhang, H. Zhang, L. Guo, K. Zheng, X.-D. Han, and Z. Zhang, "Delicate control of crystallographic facet-oriented Cu2O nanocrystals and the correlated adsorption ability," *Journal of Materials Chemistry,* vol. 19, no. 29, 2009.
[102] Z. Wang, D. Luan, F. Y. Boey, and X. W. Lou, "Fast formation of SnO2 nanoboxes with enhanced lithium storage capability," *J Am Chem Soc,* vol. 133, no. 13, pp. 4738-41, Apr 06 2011.
[103] Y. Wang, Y. Lü, W. Zhan, Z. Xie, Q. Kuang, and L. Zheng, "Synthesis of porous Cu 2 O/CuO cages using Cu-based metal–organic frameworks as templates and their gas-sensing properties," *Journal of Materials Chemistry A,* vol. 3, no. 24, pp. 12796-12803, 2015.
[104] J. H. Kwak, L. Kovarik, and J. n. Szanyi, "Heterogeneous catalysis on atomically dispersed supported metals: CO2 reduction on multifunctional Pd catalysts," *ACS Catalysis,* vol. 3, no. 9, pp. 2094-2100, 2013.
[105] D. K. Bediako, B. Lassalle-Kaiser, Y. Surendranath, J. Yano, V. K. Yachandra, and D. G. Nocera, "Structure–activity correlations in a nickel–borate oxygen evolution catalyst," *Journal of the American Chemical Society,* vol. 134, no. 15, pp. 6801-6809, 2012.

[106] L. Trotochaud, J. K. Ranney, K. N. Williams, and S. W. Boettcher, "Solution-cast metal oxide thin film electrocatalysts for oxygen evolution," *Journal of the American Chemical Society,* vol. 134, no. 41, pp. 17253-17261, 2012.
[107] M. C. Biesinger, L. W. Lau, A. R. Gerson, and R. S. C. Smart, "The role of the Auger parameter in XPS studies of nickel metal, halides and oxides," *Physical Chemistry Chemical Physics,* vol. 14, no. 7, pp. 2434-2442, 2012.
[108] S. Berg, L. Andersson, H. Norström, and E. Grusell, "2.2 Substrate surface damages by rf-sputtering," *Vacuum,* vol. 27, no. 3, pp. 189-191, 1977.
[109] F. H. Mullins and A. Brunnschweiler, "The effects of sputtering damage on the characteristics of molybdenum-silicon Schottky barrier diodes," *Solid-State Electronics,* vol. 19, no. 1, pp. 47-50, 1976.

Appendix A

Appendix A contains additional electrochemical measurements supporting the main results discussed in Chapter 3.1.

Step-by-step procedure for gas quantification data collection

Three-Electrode Setup	
Cathode (WE)	Cu_2O-SnO_2 supported by Toray 060 Carbon Paper
Reference (RE)	$Ag/AgCl_{sat\ KCl}$
Anode (CE)	Pt wire

1. Run chronoamperometric measurement (e.g. -1.62V vs $Ag/AgCl_{sat}$ or -1.0V vs RHE) on AUTOLAB workstation
2. Wait 500 seconds for gas product to saturate and then inject first sample (record time and current).
3. Obtain results after 8.4 mins from GC.
4. Run next injection and repeat until 4 data points are obtained for one potential.
5. Switch to next potential -- tests are conducted from higher (-1.82V vs $Ag/AgCl_{sat}$) to lower potential (-1.02V vs $Ag/AgCl_{sat}$).

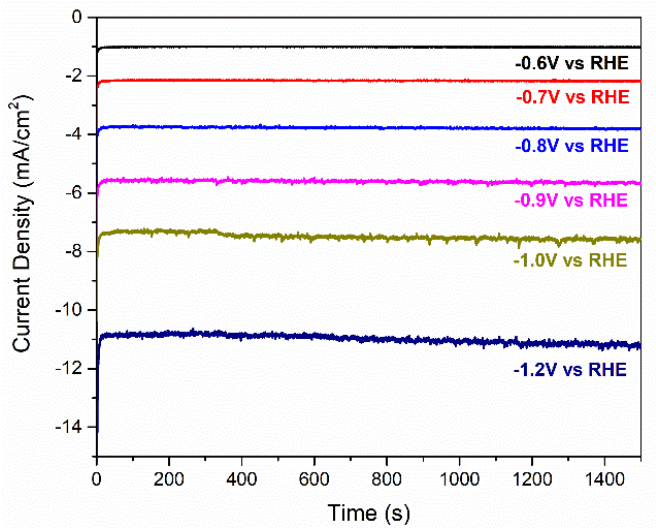

Figure A1. Chronoamperometric data for calculating gas product faradaic efficiency at each applied potential.

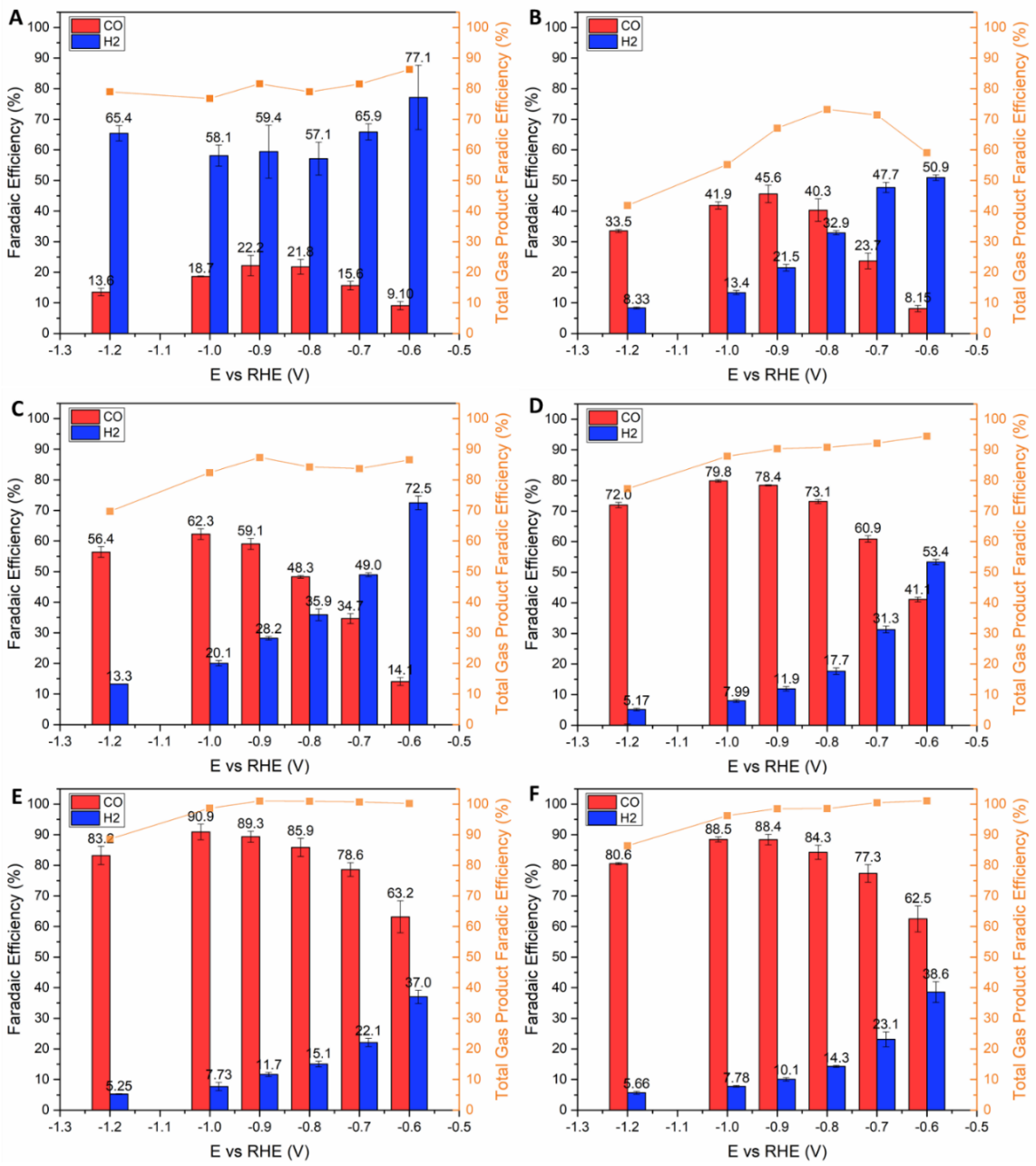

Figure A2. Gas product faradaic efficiencies for (A) Cu_2O, (B) CuSn10, (C) CuSn20, (D) CuSn30, (E) CuSn40, and (F) CuSn50. Electrolyte used is 0.1M $KHCO_3$.

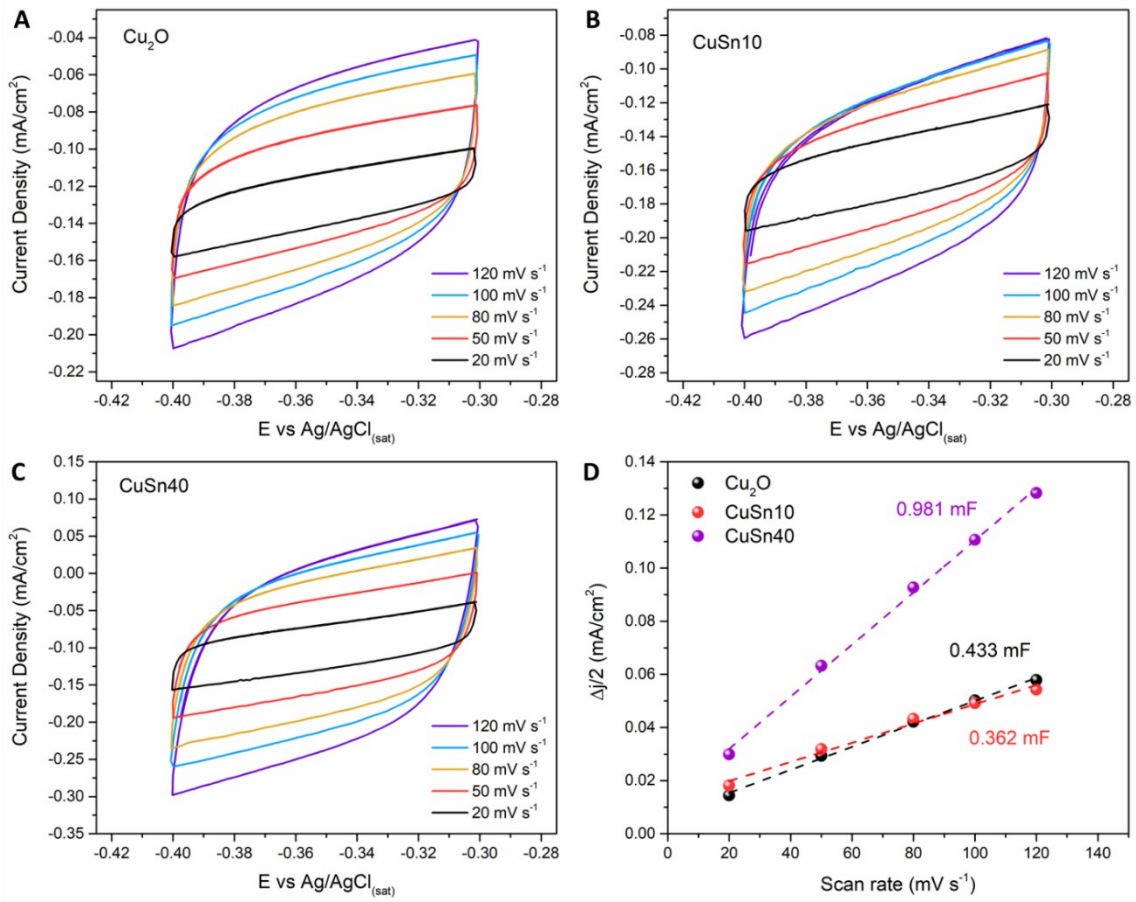

Figure A3. Determination of double-layer capacitance (C_{dl}) of Cu_2O and Cu2O-SnO2 catalyst in CO_2 saturated 0.1M $KHCO_3$ solution.

Cyclic voltammetry (CV) measurements were carried out over scan rates in a potential window where only double-layer charging and discharging is relevant. The C_{dl} was estimated by plotting the $\Delta j/2$ versus scan rates, where the slope was C_{dl} (in the unit of mF). The Δj is the difference between anodic (j_a) and cathodic (j_c) current density at the midpoint of applied potential window.

CuSn40 exhibit a higher C_{dl} comparing to Cu_2O and CuSn10, which indicate that more surface area was available for electrochemical reaction to occur. On the other hand, CuSn10 exhibit a slightly lower C_{dl} when compared to Cu_2O, which agrees with CuSn10 lower activity measured from LSVs (Figure 3-10A).

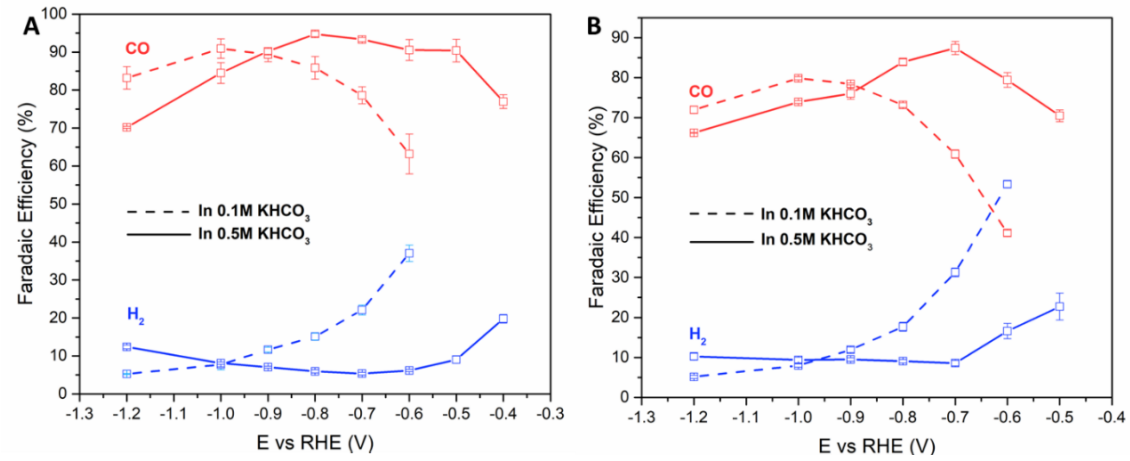

Figure A4. Catalyst performance in 0.1 M (dashed line) vs. 0.5 M $KHCO_3$ (solid line) for (A) CuSn40 and (B) CuSn30.

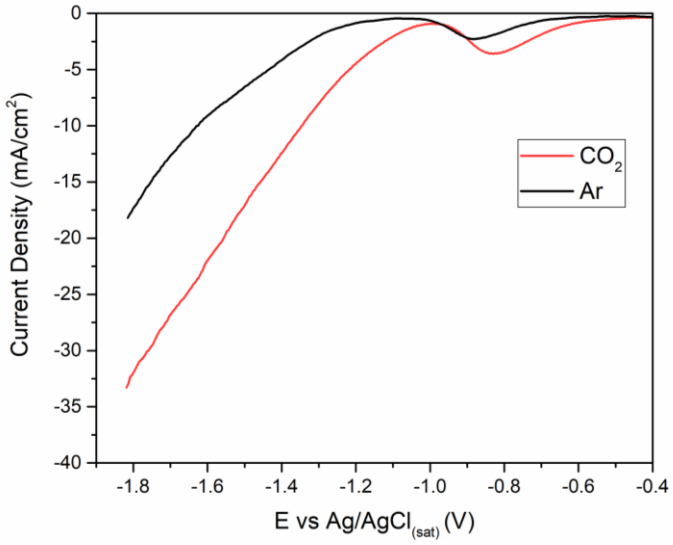

Figure A5. LSV of CuSn40 catalyst measured in 0.5 M $KHCO_3$ saturated with CO_2 (red line) and Ar (black line). The sweep rate used for LSV is 20 mV s^{-1}. The slower current density increase in Ar-saturated solution indicated that CuSn40 is catalytically favorable towards CO_2RR than HER.

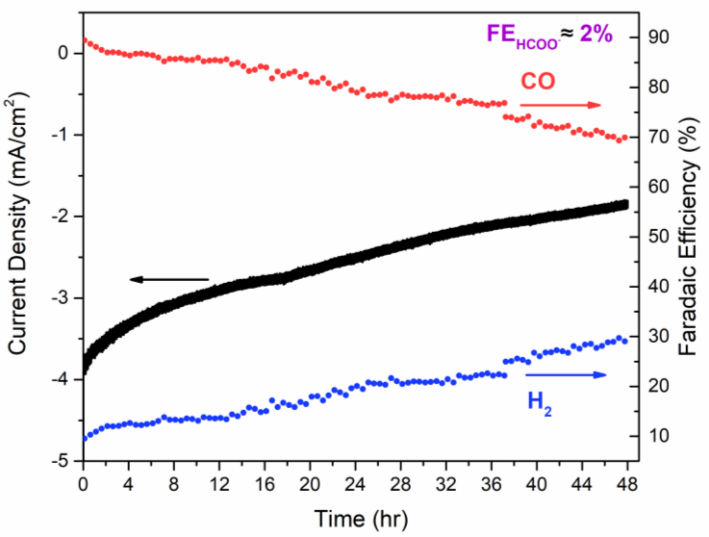

Figure A6. Extended two-day stability test of CuSn40 catalyst at -0.6 V vs. RHE in 0.5 M $KHCO_3$.

Appendix B

Appendix B contains calibration information of key equipment, including gas chromatography for gas product quantifications, and nuclear magnetic resonance spectroscopy for liquid product quantification.

GC Calibration

A standard gas (acquired from Praxair) containing 0.5% H_2, 0.5% CO, 0.5% CH_4, 0.5% C_2H_4, and 0.5% C_2H_6 was used to calibrate the gas chromatography (GC, Agilent 6890N) for gas product quantifications of CO_2RR experiments. Figure below shows a screenshot of the obtained chromatograph for the standard gas. The top portion shows signals from flame ionization detector (FID) and the bottom portion shows signals from thermal conductivity detector (TCD). The total run time for one injection is 8.4 minutes.

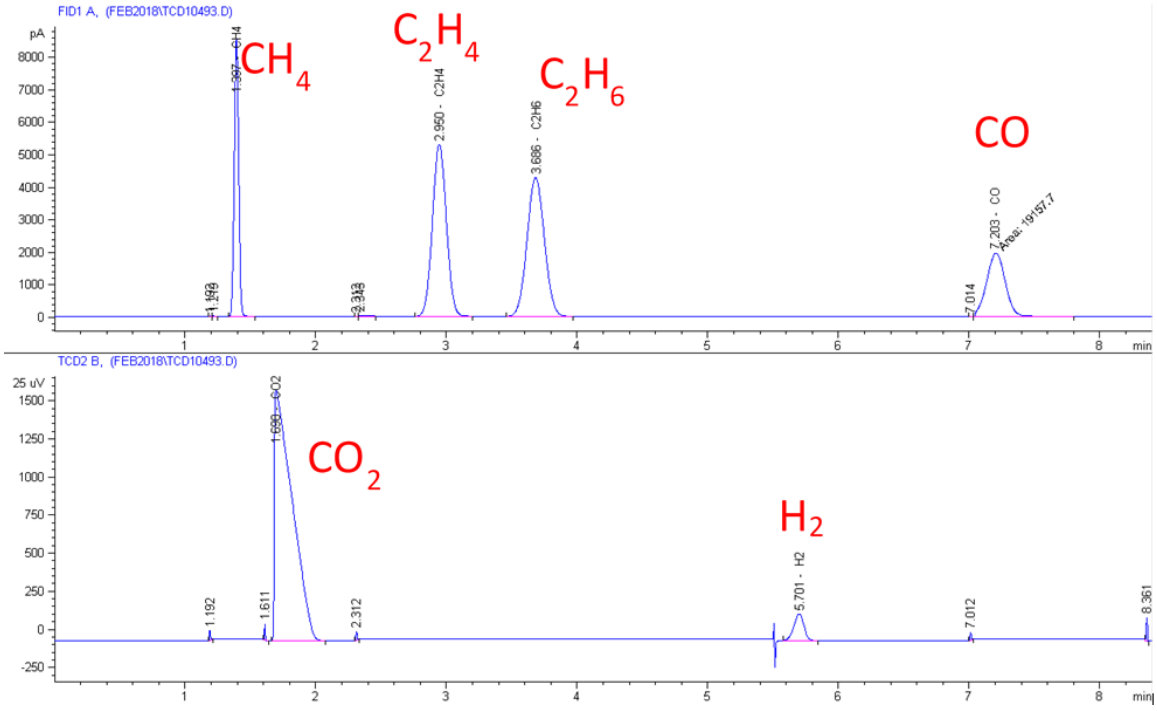

Figure B1. Chromatograph of the standard gas used for GC calibration.

The figure below shows the plumbing diagram of Agilent 6890N gas chromatography set up for the CO_2RR experiments.

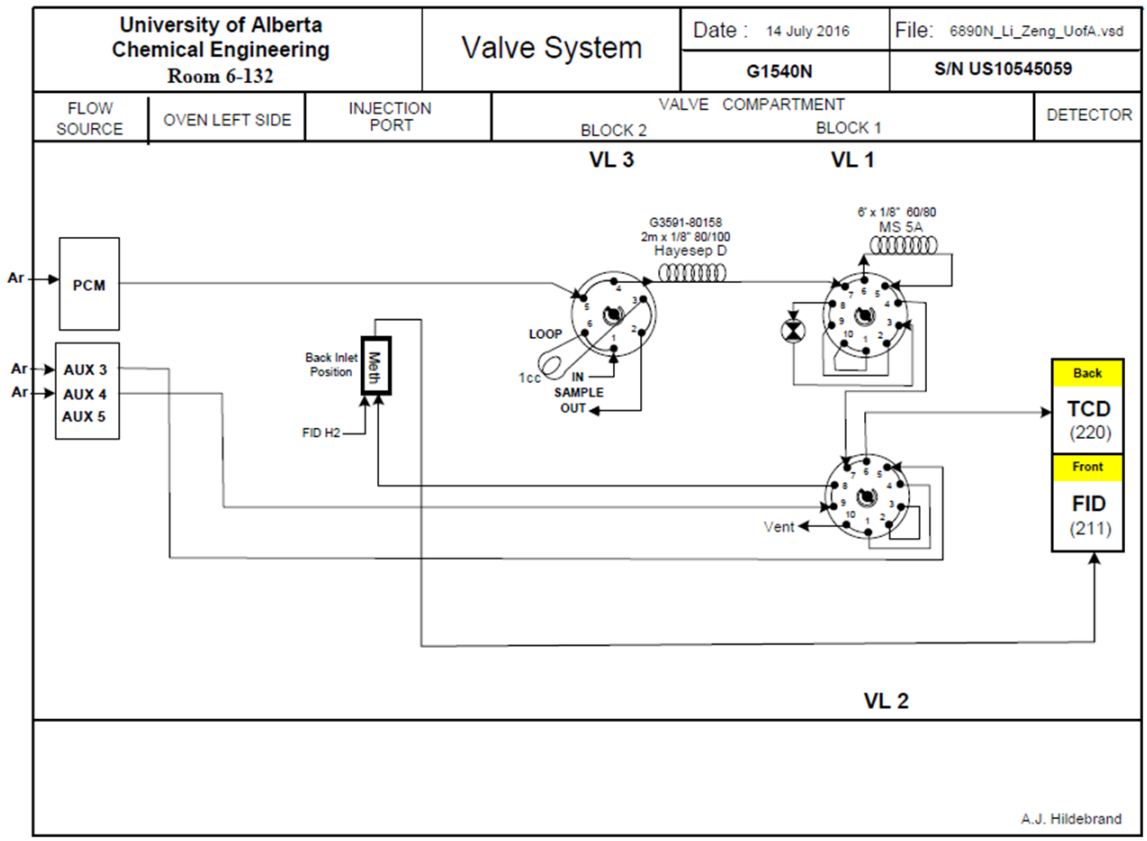

Figure B2. Plumbing diagram of the Agilent 6890N gas chromatography.

NMR Calibration

The NMR signals of known concentration of formate ($HCOO^-$) and DMSO in six standard solutions were first determined to obtain the calibration curve. The NMR peak relative area (RA) between formate and DMSO was calculated by:

$$RA = \frac{Peak\ area\ of\ formate\ at\ 8.30\ ppm}{Peak\ area\ of\ DMSO\ at\ 2.57\ ppm}$$

Then, RA was plotted as a function of formate concentration, as shown in B3 below.

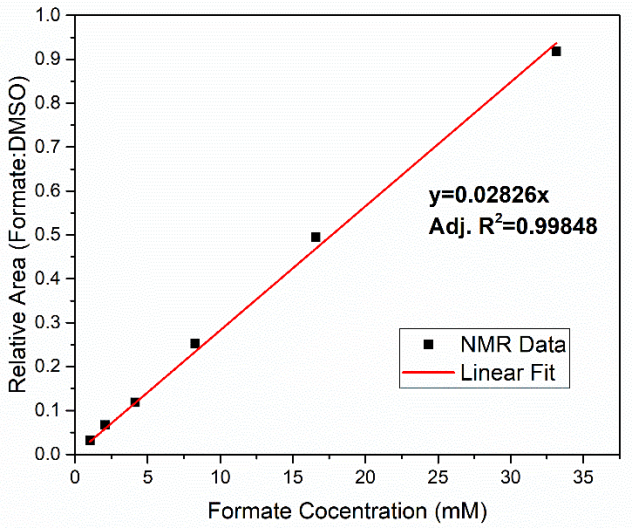

Figure B3. NMR calibration curve of Formate using DMSO as internal standard.

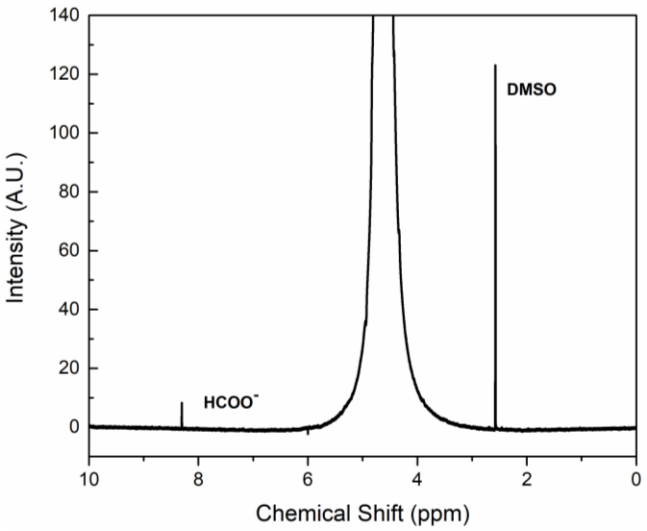

Figure B4. NMR chromatograph of a sample electrolyte extracted for test after a stability run. Two peaks showing HCOO- and DMSO at chemical shifts of 8.33 ppm and 2.6 ppm, respectively.

Nuclear magnetic resonance (NMR, 600 MHz, model VNMRS 600 Spectrometer) spectroscopy was used to identify the reduced liquid product from CO_2RR experiments. To identify reduced product from NMR chromatographs, the following table is used.[1] The only liquid product identified during experiments is formate ($HCOO^-$) listed at the 5th row of this table, with the corresponding chemical shift of 8.33 ppm.

Table B1. Peak information of possible liquid product derived from CO_2RR. Reproduced with permission.[1] Copyright 2012, Royal Society of Chemistry.

CO_2 Reduction Products							Assignment		Known Standards			
Chemical Shift	^{1}H splitting	J coupling	COSY cross peaks	^{13}C (HSQC)	^{13}C (1D)	^{13}C splitting	Probed Nucleus	Product Name	^{1}H splitting	Chemical Shift	J coupling	^{13}C (1D)
9.57	s						$CH_3CH_2C\underline{H}=O$	Propionaldehyde	s	9.57		209.6
9.55	q	2.93	2.12				$CH_3C\underline{H}=O$	Acetaldehyde	q	9.55	2.93	206.9
8.33	s			172.2	171.76	s	$\underline{H}COO^-$	Formate	s	8.33		171.77
					161.16		Bicarbonate	Electrolyte				162.97
					130.74		Phenol	Internal Standard	t	7.2	7.61	130.7
					121.24		Phenol	Internal Standard	t	6.86	7.61	121.07
					115.92		Phenol	Internal Standard	d	6.8	8.78	116.31
5.89	m		5.16, 5.06, 3.99	137.4	137.79	dd	$CH_2C\underline{H}CH_2OH$	Allyl Alcohol	m	5.9		136.86
5.16	d	17.57	5.89, 3.99		116.36	d	$C\underline{H}_2CHCH_2OH$	Allyl Alcohol	d	5.17	17.33	115.74
5.13	q	4.68	1.21		88.67	d	$CH_3C\underline{H}(OH)_2$	Acetaldehyde	q	5.13	5.37	88.57
5.06	d	10.54	5.89, 3.99		116.36	d	$C\underline{H}_2CHCH_2OH$	Allyl Alcohol	d	5.07	10.5	115.74
4.94	t	5.27	3.4		90.6	d	$(OH)_2C\underline{H}CH_2OH$	Glycolaldehyde	t	4.94	5.13	90.63
4.843	t	5.27					$CH_3CH_2C\underline{H}(OH)_2$	Propionaldehyde	t	4.85	5.87	92.77
					91.4	s	$(OH)_2C\underline{H}C(OH)_2$	Glyoxal				91.39
							WATER					
4.25	s						$CH_3C(=O)C\underline{H}_2OH$	Hydroxyacetone	s	4.25		68.36
3.99	d	4.68	5.9, 5.15, 5.05	63.5	63.44	d	$CH_2C\underline{H}CH_2OH$	Allyl Alcohol	dt	3.99	5.13, 1.46	62.96
3.545	s			63.65	63.41	s	$HOC\underline{H}_2CH_2OH$	Ethylene Glycol	s	3.54		63.41
3.54	q	7.03	1.06	58.3	58.3	d	$CH_3C\underline{H}_2OH$	Ethanol	q	3.53	7.32	58.3
3.44	t	7.03	1.42	64.35	64.42	d	$CH_3CH_2C\underline{H}_2OH$	n-Propanol	t	3.44	6.49	64.43
3.4	d	4.68	4.94	65.6	65.38	d	$(OH)_2C\underline{H}CH_2OH$	Glycolaldehyde	d	3.4	5.13	65.42
3.23	s			49.85	49.76	s	CH_3OH	Methanol	s	3.23		49.75
							DMSO	Internal Standard	s	2.6		39.6
2.44	q	7.03		37.25			$CH_3C\underline{H}_2CH=O$	Propionaldehyde	q	2.44	7.32	37.34
2.12	d	2.93	9.55	30.94	30.8	d	$CH_3CH=O$	Acetaldehyde	d	2.12	2.93	30.89
2.1	s			30.9			$CH_3C=OC\underline{H}_3$	Acetone	s	2.1		30.44
2.02	s			25.3			$CH_3C(=O)CH_2OH$	Hydroxyacetone	s	2.02		25.63
1.79	s			24	24.19	d	$CH_3C(=O)O^-$	Acetate	s	1.87		23.74
1.48	dt	5.85		30.95			$CH_3C\underline{H}_2CH(OH)_2$	Propionaldehyde	dt	1.47	7.57, 12.94	30.45
1.42	sextet	6.44	3.44, 0.77	25.28	25.37	t	$CH_3C\underline{H}_2CH_2OH$	n-Propanol	sextet	1.42	7.32	25.41
1.21	d	5.27	5.13	24	23.82	d	$CH_3CH(OH)_2$	Acetaldehyde	d	1.2	5.37	23.5
1.06	t	7.03	3.54	17.4	17.62	d	CH_3CH_2OH	Ethanol	t	1.06	7.08	17.63
0.92	t	7.61		5.74			$CH_3CH_2CH=O$	Propionaldehyde	t	0.92	7.32	5.54
0.78	t	7.61					$CH_3CH_2CH(OH)_2$	Propionaldehyde	t	0.78	7.32	8.47
0.77	t	7.61	1.42	10.2	10.34	d	$CH_3CH_2CH_2OH$	n-Propanol	t	0.77	7.57	10.36

Reference

[1] K. P. Kuhl, E. R. Cave, D. N. Abram, and T. F. Jaramillo, "New insights into the electrochemical reduction of carbon dioxide on metallic copper surfaces," *Energy & Environmental Science,* vol. 5, no. 5, pp. 7050-7059, 2012.